Astronomy Reports, Vol. 46, No. 11, 2002, pp. 867–870. Translated from Astronomicheskiĭ Zhurnal, Vol. 79, No. 11, 2002, pp. 963–967.

The Nature of Active Radio Galaxies in the Cluster A569

A. A. Lipovka and N. M. Lipovka

St. Petersburg Branch of the Special Astrophysical Observatory, St. Petersburg, Russia

Received June 15, 2000; in final form, May 23, 2002

Abstract—We investigate the nature of bright radio sources with known radio spectra in the direction of the nearby cluster of galaxies A569 ($z = 0.0193$). The optical identifications of the sources show that 45% of these radio sources are associated with compact galaxies. A substantial fraction of these galaxies have active nuclei, with the radio emission concentrated toward the galactic center. Some of the cluster galaxies have radio halos, with appreciably weaker radio powers and spectral indices $\alpha = 0.95 \pm 0.2$. We compute the magnetic fields in the nuclei and halos of the galaxies for the adopted distance to A569. As expected, the magnetic fields in the galactic halos make a smooth transition to the intergalactic field, while the magnetic fields in the central regions of the galaxies rise sharply toward the nucleus.

1. INTRODUCTION

It has been established [1] that galaxies in the region of the cluster A569 ($z = 0.0193$) are most likely gravitationally bound with three high-velocity subclusters and make up a "final" relaxed system. Velocities were computed for 41 members of this system by Beers *et al.* [1].

In 1994, we investigated a region more than 40 square degrees in size in the vicinity of A569 and obtained a catalog of 212 galaxies concentrated toward the cluster A569 and the three nearest subclusters [2]. It turned out that 9% of these have weak radio emission, emitted predominantly by their nuclei.

A multi-faceted study of the character of the radio emission of sources in the vicinity of A569 revealed a group of powerful radio sources with nonthermal spectra. These objects are not associated with the galaxies in our catalog [2], making a study of their nature of considerable interest. We discovered more than 100 such powerful radio sources near A569 and the three nearest subclusters, for which we have determined radio spectra and obtained optical identifications with relatively weak, predominantly optically compact galaxies.

In this paper, we investigate this population of objects. In Section 2, we present the results of optical identifications and of our estimates of spectral indices and magnetic-field strengths. The distance to the radio sources was taken to be 60 Mpc during the calculation of the magnetic fields. Section 3 discusses the characteristics of these objects and analyzes the distribution of their radio brightness in the optical galaxies.

2. RADIO PROPERTIES OF THE OBJECTS AND THEIR OPTICAL IDENTIFICATIONS

We identified a group of bright radio sources in the studied region ($\mathrm{RA}(1950.0) = 06^{\mathrm{h}}57^{\mathrm{m}} - 07^{\mathrm{h}}40^{\mathrm{m}}$, $\mathrm{Dec}(1950.0) = +45^\circ$ ... $+51^\circ$), for which we constructed spectra in the frequency interval 151–4850 MHz using the data of the three catalogs [3–5]. The range of spectral indices for these objects is fairly broad: from $\alpha = 0.18$ to $\alpha = 1.3$. The objects fell into two populations, depending on their spectral indices and the size of the radio-emitting region relative to the optical galaxy. We propose that these two populations reflect different evolutionary stages, as is suggested by the differences in their properties. The histogram of radio spectral indices (figure) contains two groups of objects, which, as we will show below, also have

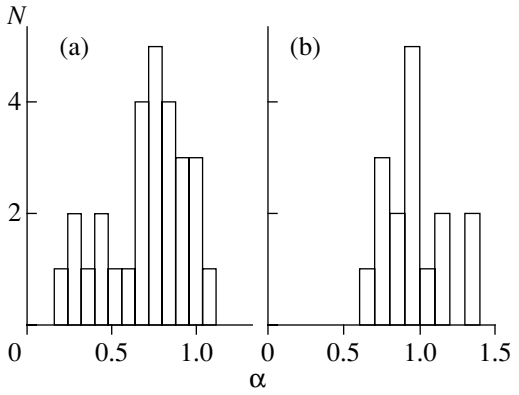

Distribution of spectral indices for galaxies with (a) radio nuclei and (b) radio halos.

1063-7729/02/4611-0867$22.00

Table 1

No.	RA (1950)	DEC (1950)	P, mJy	θ_1	θ_2	T	ε, %	H, μOe	α	R	θ	$1-b/a$
1	$6^h56^m35\overset{s}{.}3$	$+48°4'42\overset{''}{.}8$	81.3	$2\overset{''}{.}74$	$1\overset{''}{.}55$	p		8.1	0.82	$21\overset{m}{.}21$	$3\overset{''}{.}1$	0.18
2	6 57 36.4	+49 25 12.8	22.4	3.33	2.49	h	64	2.8	1.05	18.12	7.1	0.10
3	6 58 4.9	+50 35 3.6	22.3	9.53	7.90	h	56	0.7	1.3	19.87	3.5	0.21
4	6 58 3.6	+50 35 59.9	8.7	7.61	3.39	p	84	2.8	0.69	15.02	10.8	0.06
5	6 58 11.0	+50 50 19.3	495.5	1.46	0.82	n		30.	0.74	18.16	6.7	0.11
6	6 58 57.0	+50 6 36.4	197.3	17.68	6.94	h	100	2.7	0.76	19.59	4.4	0.29
7	7 0 10.6	+48 28 23.8	81.3	6.22	2.16	h	50	3.7	0.87	18.80	5.3	0.18
8	7 0 26.6	+47 5 25.3	823.0	1.04	0.65	n		25.	0.43	19.85	4.7	0.55
9	7 0 29.6	+50 34 55.2	681.0	2.32	1.36	n		50.	0.49	14.46	11.8	0.04
10	7 0 30.4	+50 34 38.6	2.5	9.10	3.32	p		1.5	0.76	17.82	6.6	0.05
11	7 0 56.7	+46 34 45.2	84.1	1.09	0.94	n		10.	0.91	14.06	11.9	0.04
12	7 2 22.2	+47 31 58.9	109.9	5.26	2.33	n		5.8	0.78	15.66	14.9	0.52
13	7 2 38.6	+46 7 40.0	18.5	6.28	3.11	p		4.1	0.67	19.13	4.5	0.07
14	7 3 5.9	+46 52 36.6	1589.9	0.86	0.58	n		70.	0.70	14.00	11.8	0.03
15	7 3 45.8	+50 5 54.6	598.7	1.91	0.52	n		20.	0.82	17.77	6.8	0.15
16	7 5 5.9	+47 25 55.8	175.4	2.02	0.00	n		20.	0.62	21.26	2.6	0.04
17	7 5 21.5	+48 41 46.0	220.0	4.74	3.1	n	40	30.	0.28	8.75	46.8	0.07
18	7 5 44.2	+46 18 35.2	42.1	4.37	3.08	p	40	2.4	1.1	19.52	4.3	0.20
19	7 5 46.0	+46 18 25.9	18.2	4.34	3.06	n		1.9	1.1	16.96	7.7	0.11
20	7 6 2.7	+48 1 39.9	136.7	2.67	1.58	n		7.4	0.92	19.06	4.8	0.14
21	7 6 13.3	+50 8 2.1	2.1	6.66	4.51	h	96	0.8	1.1	16.46	8.6	0.04
22	7 6 15.3	+50 8 1.5	10.9	2.93	1.42	h	81	2.3	1.1	16.12	10.3	0.04
23	7 7 7.0	+49 29 1.5	289.5	1.11	0.59	n		150.	0.27	19.19	4.5	0.10
24	7 8 46.7	+48 11 16.1	186.9	4.36	1.17	h	56	5.6	0.91	16.93	7.8	0.03
25	7 9 13.8	+49 46 57.1	14.0	4.20	0.68	h	66	2.5	0.98	19.45	4.1	0.16
26	7 9 20.6	+50 58 50.6	153.5	6.44	1.09	n		5.3	0.79	13.95	16.0	0.02
27	7 9 40.9	+48 54 41.8	224.6	9.45	5.33	h	49	2.9	0.95	15.96	9.0	0.04
28	7 10 48.0	+49 32 48.4	99.4	1.31	0.90	n		20.	0.81	19.54	4.6	0.27
29	7 1217.5	+48 57 56.4	286.2	1.67	0.97	n		30.	0.69	19.69	3.8	0.05
30	7 14 22.9	+46 30 55.6	18.7	7.04	3.10	h	57	2.1	0.93	17.55	11.1	0.17
31	7 14 43.3	+47 13 49.1	4.4	10.63	6.18	h	94	1.4	0.79	19.97	3.3	0.16
32	7 14 42.5	+47 13 27.3	30.1	3.57	1.87	n		6.2	0.75	19.09	5.5	0.05
33	7 15 2.5	+46 25 6.3	53.2	2.30	1.92	n		20.	0.47	17.67	10.6	0.27
34	7 15 46.6	+47 24 40.6	145.1	2.95	1.21	p		5.1	1.04	19.72	2.9	0.07
35	7 16 38.6	+47 43 20.7	234.9	2.14	1.20	n		90.	0.18	17.85	7.3	0.05
36	7 17 11.8	+46 20 16.2	131.3	3.91	2.05	h	47	3.9	1.05	20.60	6.0	0.32
37	717 14.6	+46 58 1.1	260.6	1.71	1.04	n		10.	0.91	18.87	6.4	0.21
38	7 18 .5	+45 28 28.7	59.3	2.11	1.23	n		8.7	0.84	19.87	3.2	0.11
39	7 20 53.8	+45 4 24.9	111.6	1.15	0.52	n		30.	0.66	19.27	5.5	0.23
40	7 20 59.9	+47 17 14.1	42.9	0.65	0.00	n		10.	0.96	19.63	4.0	0.11
41	7 21 11.7	+49 4 2.5	35.8	6.55	2.44	h		2.9	0.88	19.67	3.7	0.09
42	7 21 13.1	+49 4 38.1	77.8	6.34	4.92	h		1.7	1.19	19.99	2.9	0.07
43	7 23 18.3	+48 50 14.0	412.6	0.94	0.71	n		150.	0.32	19.36	4.5	0.15
44	7 23 49.8	+47 48 8.8	161.2	4.49	2.16	h	23	4.9	0.94	19.09	4.7	0.014
45	7 24 57.4	+46 46 35.8	106.3	4.04	1.52	h	69	5.5	0.88	18.38	6.4	0.147
46	7 28 38.5	+45 21 19.4	53.0	4.71	1.12	h		1.4	1.34	21.59	3.9	0.43
47	7 31 17.3	+45 14 56.5	65.0	6.85	1.87	n		4.7	0.73	17.62	8.7	0.112
48	7 36 53.8	+47 52 49.5	78.1	1.05	0.82	n		20.	0.70	17.49	8.2	0.064
49	7 37 23.9	+46 25 26.6	60.9	4.72	2.70	n		3.2	1.0	17.09	8.6	0.049
50	7 37 24.9	+46 25 50.2	95.5	13.05	6.02	h		2.	0.92	21.59	3.6	0.33
51	7 39 4.5	+49 0 18.0	45.7	9.02	6.10	h		1.9	0.97	19.49	4.6	0.169

different optical characteristics, such as their optical size and magnitude.

The optical identifications were carried out using the APM maps [6]; a high fraction of identifications was obtained (45%). However, there is a group of objects (10%) requiring additional study, since high-resolution observations [5] show a two-component structure, giving rise to difficulties in their optical identification. The unidentified radio sources are predominantly objects with nonthermal spectra ($\alpha = 0.87 \pm 0.14$) and mean fluxes P(1400 MHz) = 170 mJy. It is probable that the radio emission of these objects is associated with galactic halos and that it was not possible to obtain optical identifications for them either due to inaccuracy in their radio coordinates or because the optical brightness of the corresponding galaxy is weaker than $22^{\rm m}$.

Table 1 presents the coordinates and radio properties of those radio sources for which we obtained optical identifications with good accuracy in terms of coordinate agreement. The columns of this table contain (1) an ordinal number for each source; (2), (3) equatorial coordinates of the radio source at epoch 1950.0 from [5]; (4) the flux density in mJy at 1400 MHz [5]; (5), (6) the radio dimensions of the object in arcseconds [5]; (7) the region of the galaxy from which the radio emission is radiated: n—nucleus, p—plane, and h—halo; (8) the fraction ε of the radio emission in an outer, more extended halo [4]; (9) the calculated magnetic field in μOe; (10) the spectral index calculated using the data of [3–5]; (11) the magnitude of the object in the red [6]; (12) the optical dimensions in arcseconds [16]; and (13) the ellipticity of the galaxy $(1 - b/a)$ [6], where b/a is the ratio of the minor and major axes of the ellipse.

The radio observations of the galaxies with various resolutions and the optical data provide information about that part of the galaxy predominantly giving rise to the radio emission (the nucleus, disk, or halo), as indicated in columns (7) and (8) in Table 1.

The mean spectral index for our sample, $\alpha = 0.89 \pm 0.2$, shows that the radio emission of these objects is nonthermal and thus could be synchrotron radiation by relativistic electrons in a uniform magnetic field. We calculated the value of the magnetic field under the natural assumption that the energy density of the magnetic field cannot exceed the energy density in cosmic rays [7]. The distance to the radio galaxies was taken to be 60 Mpc, which corresponds to the recessional velocity of the cluster A569 and its three neighboring subclusters. We calculated a magnetic field for each radio source, taking into account its size (Table 1, columns 5, 6) and spectral index (column 10). The resulting magnetic-field values are presented in column 9 of Table 1. The magnetic fields in the galactic halos and intergalactic space of A569 are similar to estimates obtained for our own Galaxy [8], in the intergalactic space of the local system dominated by the Milky Way and the Magellanic Clouds.

Table 2

Region	H, μOe	$\theta_{\rm rel}$	α
Nucleus-1	81	<0.19	<0.5
Nucleus-2	22	<0.25	0.81
Plane	3.58	1.	0.85
Halo-1	2.28	3.	0.95
Halo-2	1.2	6.	0.98

3. CHARACTERISTICS OF THE OBJECTS

As we can see from the results, the fraction of optical identifications is high. The mean characteristics of the identified objects also argue in favor of the identifications obtained. The identified objects are primarily compact galaxies that are weaker than 15^m, with average sizes of $5'' \pm 2.5''$. As noted above, the corresponding radio objects can be divided into two groups:

(1) Powerful radio galaxies in which the radio emission is concentrated in the nucleus of the optical galaxy. The more compact the radio nucleus, the more powerful the radio emission and the steeper the radio spectrum. The figure presents the distribution of spectral indices for this group of galaxies.

(2) Objects with spectral indices $\alpha > 0.8$ in which the radio emission is associated with either the galactic disk or a weak halo. The objects with radio-emitting disks are much less powerful in the radio than objects in the first group. The spectra of these objects are steeper than those of objects in the first group. The objects with radio halos are somewhat weaker in the radio. The figure presents the distribution of spectral indices for the population of objects with radio-emitting disks or halos.

For convenience, we present in Table 2 the mean values of some characteristics of the objects in these two groups. The columns of the table give (1) the region of the radio emission, (2) the calculated mean magnetic field averaged over the objects in that subgroup, (3) the relative mean size of the radio-emitting region (the ratio of the radio to the optical size) θ_{rel}, and (4) the mean radio spectral index.

We subdivided galaxies with radio-emitting nuclei into two groups according to their spectral indices (nucleus-1, nucleus-2). The radio emission in galaxies with flatter spectra (nucleus-1) is more concentrated toward the center of the galaxy. Our analysis of

the radio sources with steep spectra indicated that, for some of these radio objects, high-angular-resolution observations [5] provide information about compact regions of radio emission, while observations with lower resolution [4] add to our information about the halo radio emission. We distinguished the halo-1 and halo-2 subgroups in this way.

The question of whether the halo is a restricted region with a closed field or the magnetic field makes a smooth transition into intergalactic space remains topical [7]. We can see from the calculated magnetic-field strengths and the distribution of the field in the galactic halos that the magnetic field makes a smooth transition to the intergalactic field in this cluster of galaxies and also rises sharply toward the nuclei of the galaxies (Table 2, nucleus-1 and nucleus-2). The radio flux densities in the galactic nuclei exceed those in the halos by a factor of 10^2–10^4. The concentration of the most powerful radio emission in the galactic nuclei suggests that the galaxies in our sample are active.

The mean spectral index for the unidentified radio objects is $\alpha = 0.89 \pm 0.17$, with $\theta_{mean} = 3.8'' \pm 1.75''$. Judging from the mean sizes of these objects, they appear to be in an earlier stage of development and have optical brightnesses appreciably weaker than $20^{\rm m}$, impeding their detection in the APM maps [6]. However, we also cannot exclude the possibility that some of these sources have inaccurate radio coordinates, hindering their identification with the corresponding optical objects.

High-resolution studies of galaxies with active nuclei may reveal small-scale radio structure, possibly in the form of jets. A number of the galaxies with compact radio-emitting nuclei may be candidates for active galactic nuclei.

A number of the galaxies (subgroup nucleus-1) have spectral indices $\alpha < 0.5$ and are predominantly galaxies with compact nuclei. It is reasonable to suppose that a substantial fraction of the radio emission in the nuclei of these galaxies is radiated by thermal electrons. For example, the spectrum of object no. 8 (Table 1) shows evidence for self-absorption at 1400 MHz. Based on the frequency at which self-absorption of radio synchrotron radiation in an ionized gas becomes important, we estimated the density of thermal electrons in the nucleus of this galaxy to be $N_e = 10^4$ cm^{-3}. Lower limits for the densities of free electrons in the nuclei of galaxies nos. 17, 23, 33, 35, and 43 also proved to be close to this value, 10^3–10^4 cm^{-3}.

4. CONCLUSION

We have investigated a group of bright radio sources in the direction of the galactic cluster A569. We constructed radio spectra and obtained optical identifications for more than 100 objects. Strong radio sources with nonthermal spectra are identified with compact, optically weak galaxies. The data presented in Table 1 indicate that the magnetic fields in the galactic halos make a gradual transition to the intergalactic magnetic field in the cluster A569, which is $< 10^{-6}$ Oe.

The objects whose radio emission originates in the nuclei of the optical galaxies have flatter radio spectra and more powerful radio emission than objects whose radio emission is associated with the galactic halos. Some fraction of this nuclear radio emission may be thermal emission by ionized hydrogen with a number density of 10^4 cm^{-3}.

Further high-resolution studies of the catalog of radio galaxies presented in Table 1 at millimeter wavelengths are of interest, since such observations could distinguish the thermal component of the radio emission in the galactic nuclei, as well as aid in the identification of active galactic nuclei.

5. ACKNOWLEDGMENTS

The authors are grateful to A.V. Savastena and O.V. Verkhodanov for assistance in working with various databases.

REFERENCES

1. T. C. Beers, W. Forman, J. P. Huchra, *et al.*, Astron. J. **102** (5), 1581 (1991).
2. N. M. Lipovka, A. A. Lipovka, E. Chavira, *et al.*, Preprint No. 132 (St. Petersburg, 1999).
3. O. V. Verkhodanov, S. A. Trushkin, *et al.*, in *Astronomical Data Analysis Software and Systems VI,* Ed. by G. Hunt and H. E. Payne, Astron. Soc. Pac. Conf. Ser. **125**, 322 (1997).
4. J. J. Condon, W. D. Cotton, E. W. Greisen, *et al.*, *The NRAO VLA Sky Survey,* http://www.nrao.edu/NVSS/postage.html (1996).
5. R. L. White, R. H. Becker, D. J. Helfand, and M. D. Gregg, Astrophys. J. **475**, 479 (1997).
6. M. Irwin, http://www.ast.cam.ac.uk/apmcat/ (1998).
7. S. A. Kaplan and S. B. Pikel'ner, *The Interstellar Medium* (Nauka, Moscow, 1963; Harvard Univ. Press, Cambridge, 1970).
8. N. M. Lipovka, Astron. Zh. **54**, 1211 (1977) [Sov. Astron. **21**, 688 (1977)].

Translated by D. Gabuzda

Astronomy Reports, Vol. 46, No. 11, 2002, pp. 871–873. Translated from Astronomicheskiĭ Zhurnal, Vol. 79, No. 11, 2002, pp. 968–971.

Modeling the Generation of the Magnetic Field in NGC 5775

D. D. Sokoloff

Moscow State University, Moscow, Russia

Received January 15, 2002; revised May 23, 2002

Abstract—A model for the generation of large-scale magnetic fields is constructed for the galaxy NGC 5775, in which the magnetic field has the form of a dipolar dynamo wave propagating along the galactic disk. The excitation of such a mode, which is unusual for galactic dynamos, can be explained by the strong variation of the galactic rotation with height above the plane of symmetry of the galactic disk.

1. INTRODUCTION

As a rule, the magnetic fields observed in the disks of spiral galaxies are almost completely confined to the galactic planes. According to current concepts, these fields are generated by a galactic dynamo based on the joint effect of the helicity of turbulent flows and differential rotation (see, for example, [1]). This mechanism is very stable to variations in its parameters. It excites the quadrupolar mode of the magnetic field, with the azimuthal component dominating and reaching its maximum in the galactic plane of symmetry.

The additional generation of dipolar magnetic fields is possible in the quasi-spherical gaseous halos of galaxies [2–4]. These fields can be transverse to the galactic disks, and numerical modeling of their high angles of inclination to the plane of the galactic disk becomes difficult. As a rule, the magnetic field of the disk can be clearly distinguished from the halo field. In the case of M51, the fields of the disk and halo can be distinguished even though the galaxy is viewed face-on [5].

In spite of the structural similarity of galactic dynamo models, it is probable that some spiral galaxies do not follow this behavior. Studying such galaxies can help us understand which properties are most important for standard galactic dynamo models.

Recent observations [6] of the magnetic field in the galaxy NGC 5775 appear to provide such an example. We propose here a model for the generation of the magnetic field in NGC 5775 that can explain the observations.

2. MAGNETIC FIELD AND HYDRODYNAMICS OF NGC 5775 FROM OBSERVATIONS

The galaxy NGC 5775 is observed edge-on, and radio polarization observations are not subject to Faraday depolarization at heights $|z| > 1$ kpc above the central plane of the galaxy. In this region, the magnetic-field vectors are directed at a significant angle to the disk plane, although this angle decreases with height, as usual. Tüllmann *et al.* [6] suggest the observed behavior could be associated with the effect of a strong galactic wind (in accordance with [4]). However, they prefer another explanation: the generation of a dipolar magnetic field in the thick disk.

We adopt this point of view, though we are aware of the ambiguities typical for galaxies viewed edge-on. Figure 5 from [6] appears to provide additional support for this interpretation. This figure shows a strongly filtered representation of the distribution of total intensity at 1.49 GHz together with the B vectors of NGC 5775. This distribution does not occupy the disk uniformly and resembles a wave propagating along the disk, with the distance between antinodes being about 2 kpc. This magnetic-field configuration clearly differs from that proposed by the standard galactic-dynamo model. However, we note that oscillating dipolar solutions can be found among numerical models of galactic dynamos for certain choices of parameters (see, for example, [7]). They demonstrate some morphological similarity with the regions with a single maximum of the total intensity in the figure in question.

For an extended range of galactic radii, the rotation of NGC 5775 is almost identical to that of a rigid body, and the galaxy displays a large scale height for the vertical distribution of ionized gas [8]. Tüllmann *et al.* [6] emphasized that the rotation depends considerably on the height z above the plane of the disk (see Fig. 3 from [6]).

In galactic-dynamo models, one usually assumes that the velocity Ω of the differential rotation of the disk depends only on the radius r, neglecting the dependence on the height z above the central plane

1063-7729/02/4611-0871$22.00

of the disk, at least inside the disk itself; i.e., it is assumed that $\partial\Omega/\partial r \gg \partial\Omega/\partial z$. It appears that we have the opposite case in NGC 5775, where we must take into account the vertical gradients of Ω and neglect radial gradients. Below, we shall show that, in this case, the dynamo excites a magnetic configuration similar to that observed in NGC 5775.

3. THE DYNAMO IN NGC 5775

We will use the mean-field electrodynamic equations (see, for example, [9]) for an axially symmetric magnetic field and neglect the radial gradient of Ω and the α effect responsible for the generation of toroidal magnetic field at the expense of poloidal field (the $\alpha\omega$ approximation). We will model solely those regions of the disk that are fairly distant from its center, neglecting terms containing the reciprocal radius (the local disk-dynamo problem). Let us introduce the dimensionless numbers

$$R_\alpha = \frac{\alpha_0 h}{\beta}, \quad R_\omega = \frac{\Omega' h^3}{\beta}, \tag{1}$$

where α_0 is the maximum of $\alpha(r,z)$, which is proportional to the average helicity of the turbulent motions; β is the turbulent diffusion coefficient, assumed to be constant; Ω' is the maximum gradient of the angular velocity; and h is the half-thickness of the disk in which the magnetic-field self-excitation occurs. We use the azimuthal field component B and $A = \hat{A}/R_\alpha$, where $\hat{A}$ is the azimuthal component of the vector potential, as scalar parameters describing the magnetic field. Upon standard transformations (see, for example, [10]), we obtain the following set of equations:

$$\frac{\partial A}{\partial t} = \alpha(z,r)B + \frac{\partial^2 A}{\partial z^2} + \frac{\partial^2 A}{\partial r^2}, \tag{2}$$

$$\frac{\partial B}{\partial t} = -DF(z)\frac{\partial A}{\partial r} + \frac{\partial^2 B}{\partial z^2} + \frac{\partial^2 B}{\partial r^2}. \tag{3}$$

Here, $D = R_\alpha R_\omega$ is the dynamo number, the time is measured in units of h^2/β, and $F = \partial\Omega/\partial z$ is measured in units of its maximum value and is assumed to be independent of r. Distances are measured in units of h; that is, r varies from 0 to R/h, where R is the radius of the galaxy (there is some arbitrariness in the definitions of R and h that it outside the framework of this discussion). For simplicity, we restrict our problem to self-excitation of the magnetic field (the so-called kinematic dynamo) taking the flow and helicity to be given *a priori*.

We supplement (2) and (3) with the standard vacuum boundary conditions (see, for example, [11, 12])

$$B(\pm 1) = 0, \quad \frac{\partial A}{\partial z}_{|z=\pm 1} = 0. \tag{4}$$

Instead of formulating boundary conditions in terms of r (which are likely unknown), in accordance with the treatment of Parker [13], we search for solutions periodic in r.

Equations (2) and (3) differ from the standard equations for the local galactic dynamo in that (3) contains a term with $\partial A/\partial r$ instead of $\partial A/\partial z$. On the other hand, (2) and (3) are similar to the Parker dynamo equations [13], which describe the propagation of a dynamo wave in the solar convective zone and lead to the 11-year cycle of solar activity. The differences between these sets of equations are of only minor importance.

First, the Parker equations contain derivatives of the latitude θ instead of r, while the D term is multiplied by $\cos\theta$ and becomes zero at the pole. Parker initially analyzed the behavior of a dynamo wave at a given latitude $\theta = \theta_0$ [13], with the factor $\cos\theta$ being contained in the dynamo number. The role of this factor was studied in [14] and [15]; it is important for the solar dynamo but not for our problem.

Second, as a rule, the Parker equations (in [13]) are integrated over a variable perpendicular to the layer, i.e., over z. However, this integration can be omitted (see [16] for details).

The most important difference is that α is antisymmetric in z, and the dynamo wave propagates in two parallel layers with opposite α values. It is evident that F is also antisymmetric in z. In this case, a dipolar configuration involves an antisymmetric B and symmetric A (dipole and quadrupole modes are defined in another way for the solar dynamo [17]).

Let the solution of (2) and (3) take the form

$$B(z,r) = b\exp(\gamma t + ikr)\sin\pi z, \tag{5}$$
$$A(z,r) = a\exp(\gamma t + ikr),$$

where a and b are constant amplitudes. This takes into account the boundary conditions. Substituting (5) into (2) and (3) and retaining only the first Fourier harmonics, we obtain the equations for a and b (neglecting the subsequent harmonics is similar to integrating over the convective zone in the Parker dynamo):

$$\gamma a = b - k^2 a, \tag{6}$$

$$\gamma b = -\frac{iDka}{2} - k^2 b - \pi^2 b. \tag{7}$$

The compatibility of (6) and (7) implies the dispersion relation

$$(\gamma + k^2)(\gamma + k^2 + \pi^2) = -\frac{iDk}{2}, \tag{8}$$

which differs from that for the Parker dynamo in an unimportant renormalization of D and in including

the contribution of the diffusion losses across the dynamo wave in only one of the co-factors containing $\gamma + k^2$. To simplify the calculations, we assume, in agreement with the observations, that the scale of the magnetic field is smaller in the r direction than in the z direction. Then, π^2 can be considered a small correction; that is,

$$\gamma(k) = \gamma_{P(D/2)}(k) - \frac{\pi^2}{2}, \qquad (9)$$

where $\gamma_{P(\mathcal{D})}$ is the growth rate of the Parker dynamo calculated for $D = \mathcal{D}$ without diffusion in z. The function $\gamma_{P(\mathcal{D})}(k)$ was thoroughly analyzed by Parker [13]. The maximum growth rate $\mathrm{Re}\gamma = 3|D/2|^{2/3}/(8 \times 2^{1/3}) - \pi^2/2$ is reached at $k = |D/2|^{1/3}/(2 \times 2^{2/3})$. This means that the radial size of the leading dynamo wave is $\Delta r = 2 \times 2^{2/3} h/|D/2|^{2/3}$. The self-excitation condition $\mathrm{Re}\gamma > 0$ gives the estimate $|D|_{\mathrm{cr}} = 2^{9/2}\pi^3/3^{3/2} \approx 60$ for the critical dynamo number. Standard estimates for D in spiral galaxies yield $D \approx -10$. Since D depends strongly on h, increasing the disk thickness by a factor of a few is sufficient to obtain $|D| > |D|_{\mathrm{cr}}$. For $|D| = |D|_{\mathrm{cr}}$, the dynamo wavelength is approximately one-third of its vertical size h, in good agreement with observations of NGC 5775 and the assumptions used for (9). Zero divergence provides an estimate of the inclination of the magnetic field lines to the disk plane, which gives $B_z/B_r \sim hk$; i.e., for $|D| = |D|_{\mathrm{cr}}$, $B_z/B_r \approx 3$, in full agreement with the observations.

The period of the dynamo wave is determined by the typical time for the turbulent diffusion across the disk and is equal to 10^8 yrs. Usually, α is positive and F is negative above the plane of the galactic disk, and the dynamo wave propagates to larger radii r.

The symmetry of (2) and (3) also admits quadrupolar solutions of the form $B(z, r) = b\exp(\gamma t + ikr)\cos\pi z$, but, in this case, the αB term makes no contribution to the equations for the first Fourier harmonics. Therefore, we assume that the dipolar mode is preferentially excited.

4. DISCUSSION

We have constructed a model for the generation of magnetic field that unites the magnetic-field distribution and hydrodynamics of NGC 5775 in a self-consistent way. We have used asymptotic and semi-quantitative techniques of dynamo theory, and our conclusions are semi-quantitative as well. Similar quantitative models based on numerical solutions of the mean-field electrodynamic equations remain within the framework of a standard galactic-dynamo approach but require more detailed information on the galaxy, which is limited by observational capabilities. It would be of great interest to find a galaxy similar to NGC 5775 but observed face-on.

Our analysis has shown that the most important parameters determining the magnetic field usually excited by the galactic dynamo are small vertical gradients of the angular velocity and the thin galaxy disk. Of course, these parameters are interrelated.

ACKNOWLEDGMENTS

The author is grateful to M. Urbanik for drawing his attention to the magnetic field of NGC 5775. This work was supported by the Russian Foundation for Basic Research, project no. 01-02-16158.

REFERENCES

1. R. Beck, A. Brandenburg, D. Moss, *et al.*, Ann. Rev. Astron. Astrophys. **34**, 155 (1996).
2. S. Sokolov and A. Shukurov, Nature **347**, 51 (1990).
3. A. Brandenburg, K.-J. Donner, D. Moss, *et al.*, Astron. Astrophys. **259**, 453 (1992).
4. A. Brandenburg, K.-J. Donner, D. Moss, *et al.*, Astron. Astrophys. **271**, 36 (1993).
5. E. Berkhuijsen, C. Horellou, M. Krause, *et al.*, Astron. Astrophys. **318**, 700 (1997).
6. R. Tüllmann, R.-J. Dettmar, M. Soida, *et al.*, Astron. Astrophys. **364**, L36 (2000).
7. D. Elstne, G. Rüdiger, and M. Schultz, Astron. Astrophys. **306**, 740 (1996).
8. M. D. Lehnert and T. M. Heckman, Astrophys. J. **472**, 546 (1996).
9. F. Krause and K. Radler, *Mean Field Magnetohydrodynamics and Dynamo* (Akademie-Verlag, Berlin, 1980; Mir, Moscow, 1984).
10. A. A. Ruzmaĭkin, D. D. Sokolov, and A. M. Shukurov, *Magnetic Fields of Galaxies* [in Russian] (Nauka, Moscow, 1988).
11. Ya. B. Zeldovich, A. A. Ruzmaikin, and D. D. Sokoloff, *Magnetic Fields in Astrophysics* (Gordon and Breach, New York, 1983).
12. V. Priklonsky, A. Shukurov, D. Sokoloff, and A. Soward, Geophys. Astrophys. Fluid Dyn. **93**, 97 (2000).
13. E. N. Parker, Astrophys. J. **122**, 293 (1955).
14. K. M. Kuzanyan and D. D. Sokoloff, Geophys. Astrophys. Fluid Dyn. **81**, 113 (1995).
15. V. M. Galitski and D. D. Sokoloff, Geophys. Astrophys. Fluid Dyn. **91**, 147 (1999).
16. K. M. Kuzanyan and D. D. Sokolov, Astron. Zh. **73**, 469 (1996) [Astron. Rep. **40**, 424 (1996)].
17. V. M. Galitskiĭ and D. D. Sokolov, in *Proceedings of the Workshop "Time, Chaos, and Mathematical Problems," Moscow, 2000,* Vol. 2, p. 241.

Translated by V. Badin

Astronomy Reports, Vol. 46, No. 11, 2002, pp. 874–886. Translated from Astronomicheskiĭ Zhurnal, Vol. 79, No. 11, 2002, pp. 972–985.

Chemical Composition of Stars in the Galactic Halo

S. V. Ermakov[1], V. G. Klochkova[1], V. E. Panchuk[1], and G. Zhao[2]

[1] *Special Astrophysical Observatory, Russian Academy of Sciences, Nizhniĭ Arkhyz, Karachaevo–Cherkessiya Republic, 357147 Russia*

[2] *National Astronomical Observatories, Chinese Academy of Sciences, Beijing, 100012 China*

Received January 3, 2002; revised March 15, 2002

Abstract—The chemical compositions of the atmospheres of six metal-poor stars are analyzed. Spectra with signal-to-noise ratios of no less than 100 and a resolution of $R \approx 17\,000$ were obtained using the 6-m telescope of the Special Astrophysical Observatory of the Russian Academy of Sciences. The abundances of Li, O, α-process elements (Mg, Si, Ca, Ti), Na, K, Sc, iron-peak elements (Cr, Mn, Fe, Ni, Cu, Zn), and s-process elements (Y, Ba) are derived. The star G251-54 ($[\mathrm{Fe/H}] = -1.55$, $T_{\mathrm{eff}} = 5541$ K, $\log g = 3.58$) is deficient in some elements compared to both stars with similar metallicities and the Sun. The atmosphere of G251-54 has the following elemental abundances relative to iron: $[\mathrm{O/Fe}] = +0.47$, $[\alpha/\mathrm{Fe}] \approx -0.3$, $[\mathrm{Na/Fe}] = -0.60$, $[\mathrm{Sc/Fe}] = -0.57$, $[\mathrm{Cr, Ni, Fe}] \approx 0$, $[\mathrm{Zn/Fe}] = +0.16$, $[\mathrm{Cu/Fe}] = -0.66$, $[\mathrm{Y/Fe}] = -0.70$, and $[\mathrm{Ba/Fe}] = -1.35$. The remaining five stars have metallicities in the range $-1.6 < [\mathrm{Fe/H}] < -1.3$ and normal abundances for this metallicity interval and are used as reference stars for comparison with the chemical composition of G251-54. Possible explanations for deviations of the abundances of some elements from the mean relations established for halo objects are discussed.

1. INTRODUCTION

The emphasis adopted in studies of the scatter in the chemical compositions of stars of different population types has evolved with the development of observational techniques. In the 1970s, the main source of information was determinations of large numbers of metallicities in the Strömgren photometric system, with the corresponding index calibrated primarily using curves of growth based on photographic spectra. The dispersion of metallicities in the disk population was due largely to the methods used [1]. Metallicity estimates based on photoelectric measurements were reasonable owing to the large number of measurements obtained, but a number of issues remained unresolved: the metallicity of the Hyades, the relationship between photoelectric, spectroscopic, and other determinations of globular-cluster metallicities, etc. Initially, when chemical compositions had low accuracy, a hypothesis suggesting the synthesis of all heavy elements in a single act was even put forward [2]. As techniques for numerical simulations of chemical evolution in the Milky Way were beginning to be developed, the importance of analyzing the abundances of other elements along with those of metals was pointed out [3]. In the middle and late 1980s, it was shown for a number of disk clusters and field stars [4–8] and some globular clusters [9] that the dispersion of elemental abundances within a cluster exceeded the scatter introduced by the methods used (errors in line measurements, oscillator strengths, and model approximations). The development of CCD spectroscopic chemical-composition studies left no doubt that the observed variations in the abundance curves for the atmospheres of "normal" stars are real. In the 1990s, models for the evolution of the halo began to take into account dispersions in the abundances of coeval stars (see, e.g., [10, 11]).

The abundances of most elements decrease with decreasing iron abundance and, for virtually all elements, coefficients for the corresponding abundance variations applicable within certain metallicity intervals are known [12]. However, these relations have increasingly large amounts of scatter or even disappear when there is a strong deficit of iron. This breakdown of "element–element" correlations is believed to reflect real inhomogeneity of the pre-stellar chemical composition during the early stages of the Milky Way's formation. In other words, when looking at very metal-deficient stars, we are actually seeing chemically inhomogeneous matter that was not sufficiently mixed prior to the formation of the first halo stars.

It is already evident that the chemical compositions of some halo stars do not obey the overall metallicity dependences shown by the abundances of

1063-7729/02/4611-0874$22.00

Table 1. Parameters of model atmospheres and parallaxes of stars studied

Star	$T_{\rm eff}$, K	$\log g$	[Fe/H]	ξ_t, km/s	V	π, mas	$\sigma(\pi)$, mas
G13-35	6030	4.10	−1.50	1.9	9.66	10.95	1.29
G23-14	4939	2.70	−1.46	1.7	10.76	8.11	6.21
G126-62	6067	4.14	−1.52	2.8	9.46	8.43	1.42
G147-30	6129	3.95	−1.49	2.0	9.77	8.11	1.43
G251-54	5541	3.58	−1.55	2.1	10.01	3.91	1.22
BD + 23°3912	5753	3.91	-1.36	1.4	8.89	9.38	1.24

α-process elements. For example, Fuhrmann *et al.* [13] found [Mg/Fe] = −0.28 for BD + 3°740, and McWilliam *et al.* [14, 15] found CS22968-014 and CS22952-015 to have [Mg/Fe] < 0 in the presence of a metallicity of [Fe/H] = −3.4. Carney *et al.* [16] found [α/Fe] = −0.29 and [Ba/Fe] = −1.8 for a metallicity of [Fe/H] = −1.86 for BD + 80°245. Similar results were obtained by Brown *et al.* [17] for a number of globular clusters. The underabundance of α-process elements compared to other halo stars indicates that these stars should have formed from matter that was unusually strongly enriched in the nucleosynthesis products of type-Ia supernovae. This can be explained if star formation in the parent regions of these stars continued until type-Ia supernovae began to explode, bypassing the stage of type-II supernova explosions. Since massive stars form much more rarely than low-mass stars, some clouds could have bypassed the stage of enrichment in matter processed in the interiors of massive stars. This hypothesis is supported by the fact that only low-mass stars are forming in the Taurus molecular cloud [18]. Another possible explanation is that stars and globular clusters with anomalous abundances of α-process elements have been captured from companion galaxies (e.g., the LMC).

We obtained spectra for a sample of high-proper-motion stars as part of a program to study halo stars carried out on the 6-m telescope of the Special Astrophysical Observatory [19–21]. We report here the atmospheric chemical compositions of six stars. The observational program was based on the catalog of high-proper-motion stars [22] and included stars kinematically belonging primarily to the halo with metallicities from −0.5 to −3.5 (according to the catalog data). The basic parameters of the stars studied are listed in Table 1.

2. OBSERVATIONS AND DATA REDUCTION

The spectra were obtained with the prime-focus echelle spectrometer [23] of the 6-m telescope of the Special Astrophysical Observatory of the Russian Academy of Sciences. The detector was a camera equipped with a 1040 × 1170 CCD with a pixel size of 16 × 16 μm. The spectra covered the wavelength interval 4500–8200 Å with a spectral resolution of $R = 17\,000$ and a signal-to-noise ratio of S/N > 100. The reduction of the two-dimensional echelle frames (dark-current subtraction, cosmic-ray removal, wavelength calibration, and extraction of the one-dimensional spectra) was carried out using the ESO MIDAS package. We used the program DECH20 [24] to determine the continuum level and measure the equivalent widths, which were determined by fitting Gaussians to the line profiles. Figure 1 compares our measured equivalent widths for the star BD + 23°3912 with earlier measurements

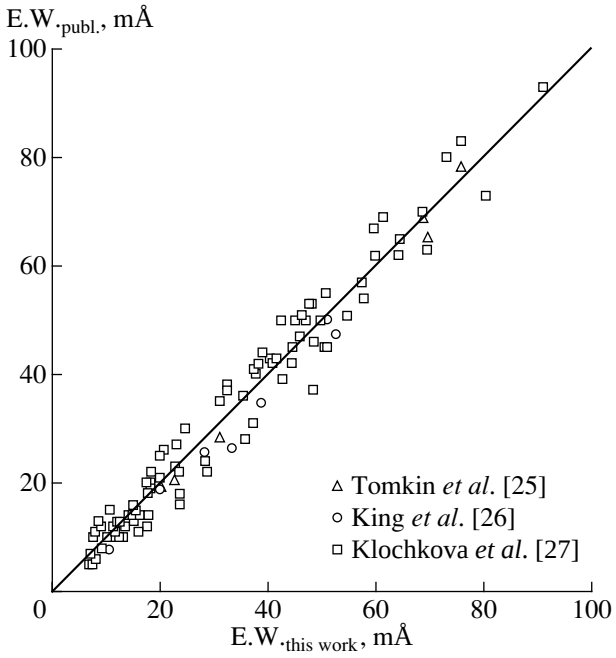

Fig. 1. Comparison of our equivalent-width measurements in the spectrum of BD + 23°3912 with published data [25–27].

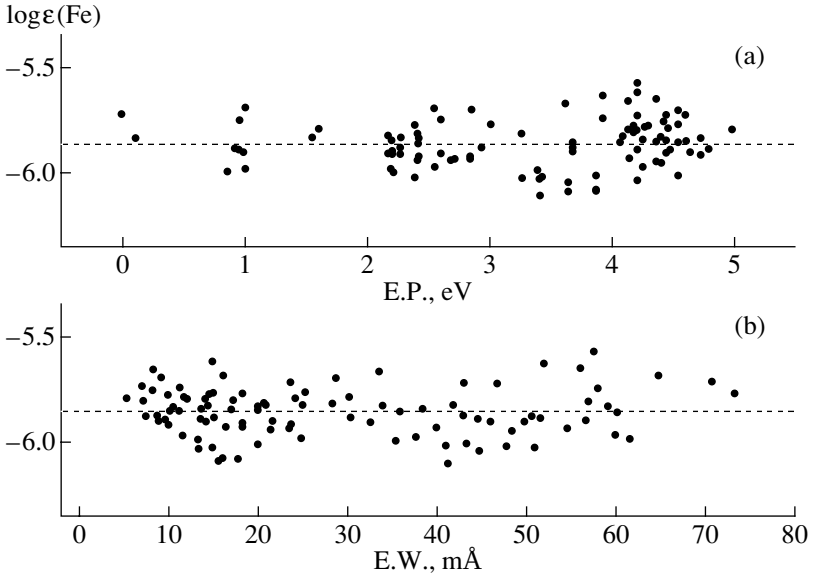

Fig. 2. FeI abundance determined from individual lines as a function of (1) excitation potential (upper panel), to illustrate the method used to determine the effective temperature, and (2) equivalent width (lower panel), to illustrate the method used to determine the microturbulence velocity.

published by Tomkin *et al.* [25] (triangles), King *et al.* [26] (circles), and Klochkova *et al.* [27] (squares).

3. PARAMETERS OF THE MODEL ATMOSPHERES

We determined the parameters of the model atmospheres as follows. We derived the effective temperature $T_{\rm eff}$ from the Strömgren photometric indices $(b-y,\, c_1)$ and the metallicities [Fe/H] from calibrations based on the infrared flux method [28]. The metallicities required for the first iteration of the $T_{\rm eff}$ computation were initially taken from the literature, but spectroscopic metallicities derived from the iron abundance were used in subsequent iterations. Our model allowed for about one hundred FeI lines for each star. The error in the resulting $T_{\rm eff}$ values is about 100 K. In addition, we used two more methods to verify the effective temperatures we obtained: (a) a method based on a spectral analysis of the FeI lines (the abundance should be independent of the excitation potential) and (b) a synthetic-spectrum analysis of the wings of the H_α line (the wings of the H_α lines are virtually unaffected by either the surface gravity $\log g$ or metallicity [Fe/H] in the effective temperature interval considered [29]). These three methods yield effective temperatures in good agreement with each other. Table 1 gives the $T_{\rm eff}$ values and other parameters used when deriving the model atmospheres. Figure 2 uses the star BD + 23°3912 as an example to show that the iron abundance derived from the FeI lines is independent of the excitation potential (for $T_{\rm eff} = 5753$ K, $\log g = 3.91$, [Fe/H] $= -1.36$). We computed the synthetic spectra using the STARSP program [30].

In most studies, the surface gravity is determined from the condition of ionization balance: FeI and FeII lines should yield the same iron abundances. However, this method can be subject to a number of errors, due to errors in the adopted system of oscillator strengths, non-LTE effects for the FeI and FeII lines, and uncertainties in the structure of the model atmospheres. We therefore used the following relations to determine the surface gravity:

$$g\frac{g}{g_\odot} = \log\frac{\mathcal{M}}{\mathcal{M}_\odot} + 4\log\frac{T_{\rm eff}}{T_{\rm eff_\odot}} + 0.4(M_{\rm bol} - M_{\rm bol,\odot})$$

and

$$M_{\rm bol} = V + BC + 5\log\pi + 5,$$

where $\mathcal{M}$ is the mass of the star, $M_{\rm bol}$ is its bolometric absolute magnitude, BC is the bolometric correction, and π is the parallax.

We used HIPPARCOS parallaxes [31], and determined the stars' masses using the grid of evolutionary tracks of van den Berg *et al.* [32], which are given in metallicity steps of ~ 0.1 dex. The bolometric corrections were computed from the calibrating formula of Balona [33]. For three stars in our sample, the $\log g$ values determined in this way agree very closely with the spectroscopic gravity estimates, and the FeI and FeII abundances computed with these $\log g$ values agree to within the abundance errors. We therefore adopted the spectroscopic $\log g$ values for the three remaining stars with low-accuracy parallaxes.

Table 2. Computed abundance errors for BD + 23°3912 ($T_{\rm eff} = 5753$ K, $\log(g) = 3.91$, [Fe/H] $= -1.36$ dex, $\xi_t = 1.4$ km/s). The last column gives the combined error assuming individual errors are uncorrelated

Estimated parameter	$\frac{\sigma_{EW}}{\sqrt{N}}$	$\Delta T_{\rm eff} = +100$ K	$\Delta \log g = +0.2$	$\Delta\xi_t = +0.3$ km/s	$\sigma_{\rm tot}$
Δ[FeI/H]	0.012	0.068	−0.004	−0.029	0.075
Δ[FeII/H]	0.037	−0.004	0.069	−0.022	0.081
Δ[Li/H]	0.051	0.079	0.001	−0.010	0.095
Δ[O/Fe]	0.019	−0.070	0.046	−0.010	0.087
Δ[Na/Fe]	0.020	0.075	−0.055	−0.030	0.100
Δ[Mg/Fe]	0.098	0.047	−0.005	−0.013	0.110
Δ[Si/Fe]	0.021	0.031	0.006	−0.005	0.038
Δ[K/Fe]	0.078	0.085	−0.040	−0.100	0.158
Δ[Ca/Fe]	0.017	0.058	−0.020	−0.037	0.074
Δ[Sc/Fe]	0.047	0.032	0.072	−0.023	0.095
Δ[TiI/Fe]	0.019	0.094	−0.004	−0.032	0.101
Δ[TiII/Fe]	0.042	0.032	0.070	−0.032	0.093
Δ[CrI/Fe]	0.033	0.094	0.000	−0.020	0.102
Δ[CrII/Fe]	0.060	−0.004	0.073	−0.010	0.095
Δ[Mn/Fe]	0.018	0.060	0.000	−0.004	0.063
Δ[Ni/Fe]	0.031	0.060	0.007	−0.014	0.069
Δ[Cu/Fe]	0.150	0.089	0.006	−0.010	0.175
Δ[Zn/Fe]	0.035	0.040	0.030	−0.035	0.071
Δ[Y/Fe]	0.015	0.040	0.070	−0.015	0.084
Δ[Ba/Fe]	0.055	0.063	0.053	−0.117	0.153

We computed the microturbulence velocities $\xi_{\rm t}$ based on the condition that the iron abundances inferred from individual iron lines should be independent of equivalent width (Fig. 2b). We used the WIDTH9 code [34, 35] and Kurucz's grid of model atmospheres [34, 35] for the abundance computations.

4. OSCILLATOR STRENGTHS

We compiled a list of unblended lines used to determine the metallicities and elemental abundances based on the list of lines in the solar spectrum of Prieto and López [36]. We selected lines whose equivalent widths were less than 100 mÅ for stars in the metallicity interval considered ($-1.6 <$ [Fe/H] < -1.3), since stronger lines are too sensitive to the choice of microturbulence velocity. We measured the initially selected lines in the spectrum of BD + 23°3912, which we used as a standard and whose chemical composition has been determined multiple times in the past (see, e.g., [25–27]). Lines that yielded systematic deviations in the abundances were not used in the subsequent analysis.

We used several lists to choose the system of oscillator strengths for the FeI and FeII lines that we employed to determine the microturbulence velocities and metallicities and to verify the correctness of the derived effective temperatures. We determined the equivalent widths of FeI and FeII lines in spectra obtained with the prime-focus echelle spectrometer [23] for three stars with well-known parameters (the Sun, Procyon, and BD + 23°3912). We then used the known model-atmosphere parameters to compute the iron abundances for each of the three stars using all the lines. In the end, we adopted the system [27], which yielded the lowest scatter of the abundances for individual lines and was most consistent with the adopted model-atmosphere parameters for all three stars. We adopted the oscillator strengths for other elements from the following sources: LiI—[38], OI—[39], NaI—[40], MgI— [41], SiI—[42], KI—[43], CaI—[44, 45], ScII—[46] and the NBS data [38, 47, 48], TiI—[49], TiII—[50, 51], CrI—[52], CrII—the NBS data [38, 47, 48] and [53], MnI—[49], NiI—[52], [54], and the NBS data [38, 47, 48], CuI—[38, 55], ZnI—[49], YII—[38, 55], BaII—[56]. The oscillator strengths for most of the elements were taken from the VALD database [57–59].

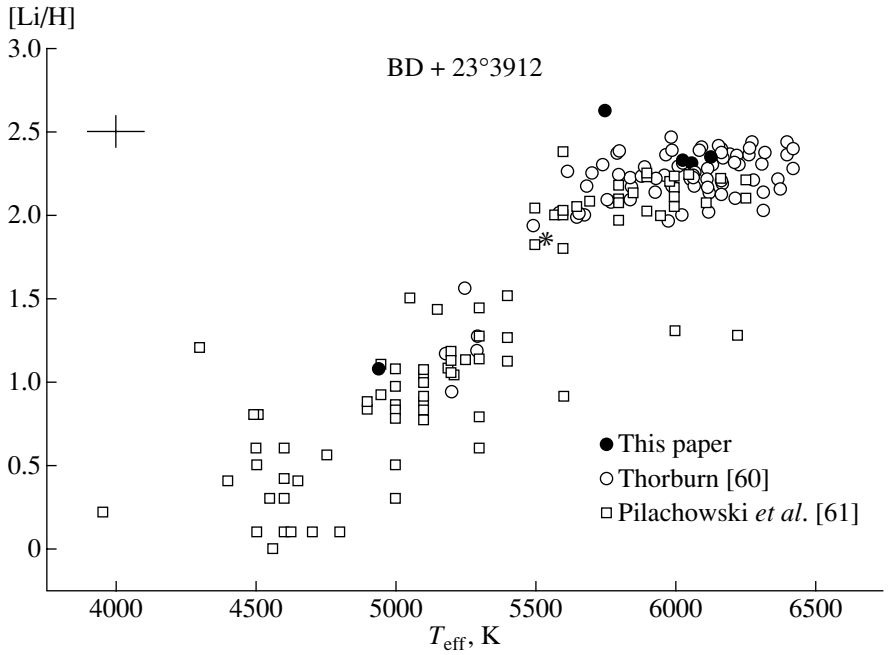

Fig. 3. Lithium abundance in the atmospheres of stars studied as a function of effective temperature (filled circles). Published data [60, 61] are shown for comparison (open symbols). The asterisk shows the position of G251-54. Also shown is BD + 23°3912, which is overabundant in Li.

5. ERRORS OF THE ABUNDANCES

The accuracy of the elemental abundances depends on several factors, which can be (arbitrarily) subdivided into the following two groups. The first errors are those affecting individual lines, such as errors in the measured equivalent widths, the adopted oscillator strengths, and the damping constants. The second group of errors are associated with factors affecting the abundance determinations based on line groups and, first and foremost, uncertainties in the parameters of the models used to compute the chemical compositions.

A comparison of our measurements with previously published data (Fig. 1) shows that the mean deviation of the single-line equivalent widths is 3–4 mÅ, which translates into in an abundance error of about 0.06 dex for a line with an equivalent width of 50 mÅ. The error decreases by a factor of $\sqrt{\rm N}$ if the abundance is determined from N lines. It is thus possible to estimate the errors due to equivalent-width measurements for elements represented by one or several lines. For elements with many spectral lines (e.g., FeI, for which about one hundred lines were measured), the scatter of the abundances based on individual lines is about 0.1 dex, which corresponds to an error of about 0.01 dex. Errors due to uncertainties in the atomic data are more difficult to estimate; however, errors due to uncertainties in the oscillator-strength scale largely cancel each other out in the case of differential determinations of the chemical composition.

The errors due to uncertainties in the model-atmosphere parameters can be estimated by computing the abundances of individual elements using atmospheric parameters that differ from the corresponding values. Table 2 lists the results of such computations for BD + 23°3912. We adopted the deviations from optimal model parameters $\Delta T_{\rm eff} =$ 100 K, $\Delta \log g = 0.2$, and $\Delta \xi_t = 0.3$ km/s. The resulting rms error in the abundances does not usually exceed 0.1 dex for most elements.

6. DERIVED ELEMENTAL ABUNDANCES

Lithium

We used the 6707 Å line to measure the lithium abundance. The abundance error was estimated by assuming that the mean error of the equivalent-width measurements was 5 mÅ. Figure 3 compares our results with those of Thorburn [60] and Pilachowski *et al.* [61]. The stars G251-54 and G23-14, which have low effective temperatures (5541 and 4939 K, respectively), are underabundant in lithium. The remaining stars, which fall in the so-called Spite plateau, exhibit normal lithium abundances for their temperatures and metallicities. BD + 23°3912 is overabundant in Li by about 0.15 dex compared to the other stars, in agreement with previous analyses for this star (see, e.g., [26, 61]).

Table 3. Atmospheric abundances for the stars studied

Element	G13-35	G23-14	G126-62	G147-30	G251-54	BD + 23°3912
logε(FeI/H)	−6.00	−5.96	−6.02	−5.99	−6.05	−5.86
logε(FeII/H)	−5.97	−5.95	−5.94	−5.98	−6.01	−5.79
[Li/H]	2.33	1.07	2.31	2.35	1.85	2.63
[O/Fe]	−	0.84	0.78	−	0.47	0.81
[Na/Fe]	0.05	0.05	0.09	0.05	−0.60	0.04
[Mg/Fe]	0.25	0.27	0.24	0.25	−0.30	0.25
[Si/Fe]	0.34	0.38	0.35	0.31	−0.33	0.40
[K/Fe]	0.36	−	0.30	0.32	−	−
[Ca/Fe]	0.37	0.37	0.38	0.39	−0.31	0.36
[Sc/Fe]	−0.04	−0.03	0.11	−0.04	−0.57	0.02
[Ti/Fe]	0.28	−0.03	0.30	0.26	−0.29	0.24
[Cr/Fe]	0.06	−0.01	0.06	0.02	0.03	0.01
[Mn/Fe]	−0.30	−0.35	−0.26	−0.32	−0.52	−0.32
[Ni/Fe]	0.02	0.01	−0.06	−0.06	−0.04	−0.04
[Cu/Fe]	−0.20	−0.84	−0.28	−0.27	−0.66	−0.20
[Zn/Fe]	0.14	0.15	−	0.18	0.16	−
[Y/Fe]	0.11	−0.07	0.11	0.06	−0.70	0.05
[Ba/Fe]	0.09	−0.11	0.14	0.07	−1.35	0.17

Oxygen

To determine the oxygen abundance, we used the infrared triplet near 7770 Å. The IR triplet is known to overestimate the oxygen abundance compared to the values derived from the [OI] 6300, 6363 Å forbidden lines or from OH rotational bands [25, 62]. We detected the IR triplet in only four of the stars, the corresponding spectral region being beyond the echelle frame in the remaining cases. The results are listed in Table 3 and shown in Fig. 4a. Our analysis yielded very similar results for three stars, whose mean abundance is [O/Fe] = +0.81 with the maximum deviation for individual stars not exceeding 0.03 dex.

Stars in the metallicity interval occupied by our six stars exhibit overabundances of oxygen, corresponding to the oxygen abundances in metal-poor halo stars. The constancy of the oxygen overabundance for metallicities from −3 to −1 is usually attributed to the fact that the synthesis of oxygen occurs in massive stars that end their evolution as type II, Ib, and Ic supernovae. Stars of this type exploded primarily during the early stages of the evolution of the Milky Way. We found G251-54 to have a relative abundance of [O/Fe] = +0.47, which cannot be explained by the errors in the equivalent widths and/or the model-atmosphere parameters. This result is in good agreement with the value [O/Fe] = +0.37 published by Carney *et al.* [16].

α-Process Elements

The variations of the abundances of α-process elements (Mg, Si, Ca, Ti) as a function of metallicity are expected to mainly follow the oxygen abundance variations. However, in contrast to oxygen and magnesium, which are synthesized only in the final stages of the evolution of massive stars, elements such as Si, Ca, and Ti can also be partly synthesized in type-Ia supernovae (see, e.g., [63]).

We determined the abundance of Ti by averaging the abundances obtained from lines of neutral and ionized titanium. For all stars except G251-54, our abundances are in good agreement with each other and are characteristic of the metallicity interval considered (see Figs. 4c, 4d, 4f, 4g). The mean abundances of individual elements are [Mg/Fe] = +0.25, [Si/Fe] = +0.37, [Ca/Fe] = +0.37, and [Ti/Fe] =

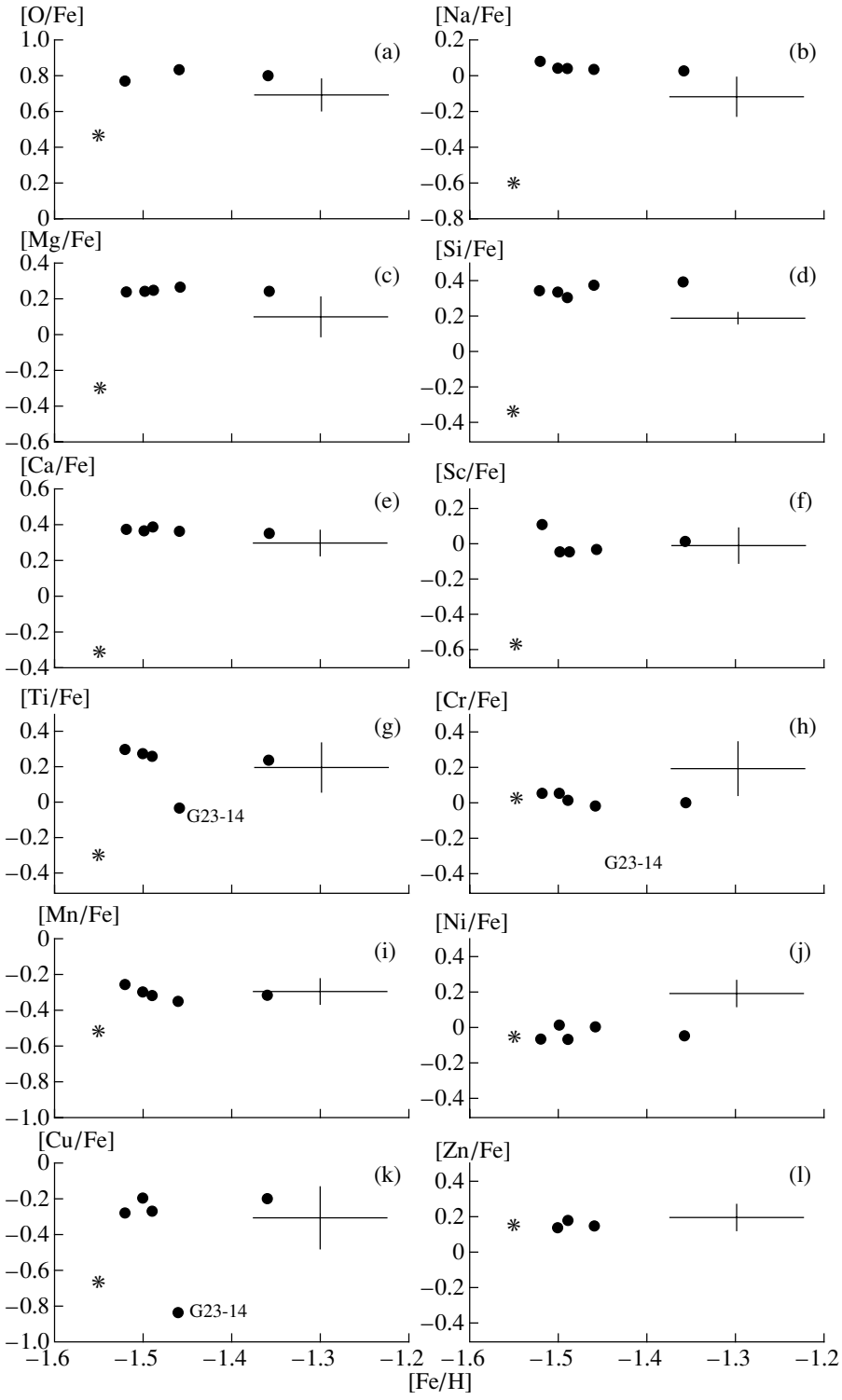

Fig. 4. Abundances of various elements in the atmospheres of the six stars as a function of metallicity [Fe/H]. The asterisk denotes G251-54.

+0.27. These values agree quite well with abundances obtained by other authors for other metal-poor stars (see, e.g., [14, 64]). G251-54 is deficient in α-process elements relative to both halo stars and the Sun.

The differences between the abundance for G251-54 and the mean abundance for the remaining

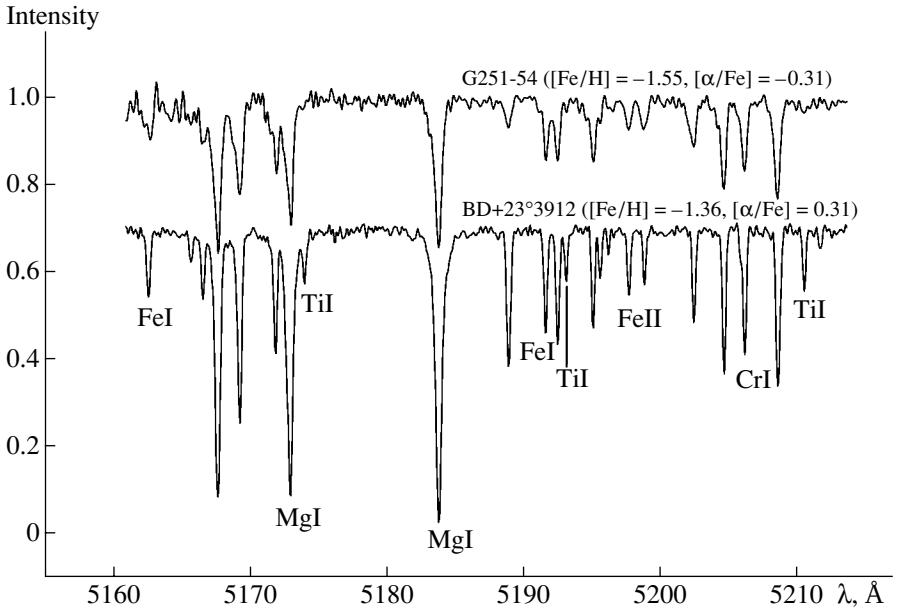

Fig. 5. Comparison of the spectrum of G251-54, which is underabundant in α-process elements, and that of a "normal" star (BD + 23°3912) near the magnesium triplet.

stars are δ[O/Fe] = 0.34, δ[Mg/Fe] = 0.55, δ[Si/Fe] = 0.70, δ[Ca/Fe] = 0.68, and δ[Ti/Fe] = 0.56. In the case of G23-14, our abundances for all α-process elements except Ti agree well with those of the other stars; we found a small deficit of Ti compared to the other stars, [Ti/Fe] = −0.03. Figure 5 shows examples of the spectra from 5180–5210 Å of G251-54 and BD + 23°3912, which have similar metallicities but very different α-process element abundances.

Sodium

Sodium, an element with an odd number of protons, is generally believed to be synthesized in massive stars during the stage of neon and carbon burning [65]. In this case, the quantity of synthesized Na depends on the neutron flux, which, in turn, depends on the metallicity and, first and foremost, the oxygen abundance.

The mean sodium abundance for our six stars is close to the solar value and is equal to [Na/Fe] = +0.06 with a maximum scatter of 0.03 dex (Fig. 4b). G251-54, whose atmosphere is strongly deficient in α-process elements, is also very deficient in Na: the relative abundance is [Na/Fe] = −0.6 and differs from the relative abundances of "normal" stars with similar metallicities by δ[Na/Fe] = 0.66.

Potassium

In the available spectral interval, the potassium abundance can be measured only from the 7699-Å resonance line. According to Chen *et al.* [44] and Gratton and Sneden [66], who analyzed the chemical compositions of disk stars, potassium is overabundant relative to the Sun and the variation of the potassium abundance as a function of metallicity is similar to that of α-process elements—the [K/Fe] ratio decreases with increasing [Fe/H] for metallicities from −1.2 to 0. Samland [67] was able to reproduce the observed dependence well with a theoretical model assuming that potassium is synthesized in massive stars during the oxygen-burning stage. The computations of Timmes *et al.* [68] predict that [K/Fe] < 0 at [Fe/H] < −0.6, which is clearly inconsistent with the observations. However, the computations of Takeda *et al.* [69] showed that non-LTE corrections for the 7699-Å line for the Sun and Procyon are −0.4 dex and −0.7 dex. Although no non-LTE corrections were computed for metal-poor stars, the large corrections obtained for the Sun and Procyon suggest that the corresponding non-LTE corrections should also substantially affect the relations obtained for metal-poor stars.

We were able to measure the 7699-Å line for only three of our six stars (in the other spectra, this line was either strongly blended with telluric lines or fell outside the recorded wavelength interval). The mean relative potassium abundance compared to the solar value was [K/Fe] = +0.33, with only a small scatter about the mean. Unfortunately, the 7699-Å line in the spectrum of G251-54 lies beyond the wavelength interval considered.

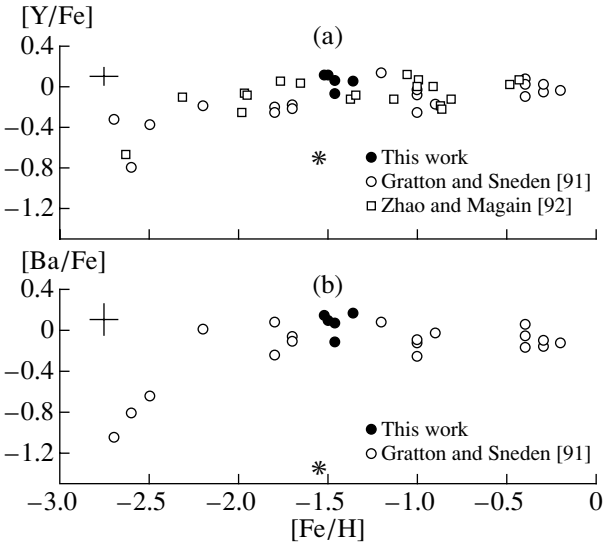

Fig. 6. Abundances of (a) yttrium and (b) barium in the atmospheres of the stars studied (filled circles) as a function of metallicity [Fe/H]. The data of [91, 92] are shown for comparison. The asterisk marks G251-54.

Chromium and Nickel

The abundances of these elements, which belong to the iron group and have even numbers of protons in their nuclei, closely follow that of iron. The chromium lines in the spectra of stars with the metallicities considered are weak. Therefore, the scatter of the chromium abundances obtained for stars with similar metallicities is not interpreted as reflecting real differences in chemical composition but instead as being due to errors in the measured equivalent widths.

We determined the chromium abundance using both lines of neutral and ionized chromium, reducing the abundance errors. We obtained the abundance ratios $[\mathrm{Cr/Fe}] = +0.03$ and $[\mathrm{Ni/Fe}] = -0.03$. It is interesting that the abundances of these elements for G251-54 in no way stand out among those for stars of similar metallicity (Figs. 4h, 4j).

Scandium and Manganese

Scandium, which is intermediate between the α-process and iron-group elements, is of greatest interest from the viewpoint of nucleosynthesis in the Milky Way. However, until recently only a few analyses of scandium abundances had been published, especially for metal-poor stars. According to the results of Peterson [70], Luck and Bond [71], and Gilroy *et al.* [72], who neglected the hyperfine structure of the Sc lines, the abundance of this element is approximately solar for the entire range of observed metallicities, albeit with a fairly large scatter from star to star. The analysis of Gratton and Sneden [73], who took into account hyperfine structure, yielded approximately the same result. In their analysis of 90 disk stars taking into account hyperfine structure, Chen *et al.* [44] found the metallicity dependence of the Sc abundance to be similar to that for α-process elements: the [Sc/Fe] ratio increases to +0.2 dex as the metallicity decreases to −1.0. The scatter of the Sc abundances increases with decreasing metallicity and is equal to 0.5 dex for the most metal-poor stars.

In our analysis of the Sc abundance, we neglected the effects of hyperfine structure. The mean Sc abundance for five stars of our sample was equal to the solar value—$[\mathrm{Sc/Fe}] = 0.00$ (Fig. 4f)—with a small scatter about the mean. However, when derived taking into account the hyperfine-structure corrections of Chen *et al.* [44], which range from +0.1 to +0.3 dex depending on the equivalent width of the line considered, our mean Sc abundance increases to about +0.2 dex. The Sc abundance of G251-54 is $[\mathrm{Sc/Fe}] = -0.57$ dex; i.e., like α-process elements, Sc is strongly underabundant relative to the other stars.

Like scandium, manganese contains an odd number of protons. Although the mechanisms for the synthesis of this element are not entirely clear, there is general agreement that Mn should be primarily produced in type-Ia and, possibly, to a lesser degree, in type-II supernovae (see, e.g., [67, 68]). Furthermore, it seems evident that the synthesis of manganese should depend very strongly on metallicity, and its abundance should decrease toward metal-poorer stars. Analyses of the abundance of this element are difficult in metal-poor stars due to the weakness of the few Mn lines that can be measured in the accessible wavelength interval. In his analysis of the Mn abundances in 25 stars with metallicities of $-2.4 < [\mathrm{Fe/H}] < -0.1$ allowing for the hyperfine structure of the MnI lines, Gratton [74] concluded that the Mn abundance is constant and equal to −0.34 dex when $[\mathrm{Fe/H}] < -1$, and increases to the solar value at higher metallicities. McWilliam *et al.* [14] and Ryan *et al.* [75] report Mn deficits of −0.8 to −1.2 dex in extremely metal-poor stars. However, the results of a number of studies [44, 73] suggest the presence of constant Mn abundances in intermediate-metallicity halo stars.

Table 4. Relative contribution of the *s* and *r* processes to the synthesis of Y and Ba in the solar system

Element	*s* main	*s* weak	*r*
Y	0.81	0.15	0.04
Ba	0.89	0.01	0.10

The Mn abundance for five of our six stars varies from −0.26 to −0.35 dex, with an average value of [Mn/Fe] = −0.31; G251-54 has a stronger Mn deficit of [Mn/Fe] = −0.52 (Fig. 4i).

Copper and Zinc

The analyses of the Cu and Zn abundances as functions of metallicity in the atmospheres of metal-poor stars performed by Sneden and Crocker [76] and Sneden *et al.* [77] showed that the [Cu/Fe] ratio decreases linearly with decreasing [Fe/H], whereas [Zn/Fe] remains constant at a value of +0.04 throughout the matallicity interval studied, down to [Fe/H] = −3 (individual values range from −0.15 to +0.3 dex). Sneden *et al.* [77] suppose that copper is synthesized primarily via the weak *s* process in the cores of massive stars, with a small contribution from explosive burning during type II supernovae. However, Matteucci *et al.* [78] suggested that type-Ia supernovae are the main source of Zn and Cu in the Milky Way and that this, in turn, may imply that type-Ia supernovae took place at metallicities [Fe/H] < −1.

The mean Cu abundance for four of our stars was [Cu/Fe] = −0.24, with a scatter of 0.04 dex (Fig. 4k). We obtained abundance ratios of [Cu/Fe] = −0.66 and −0.84 for G251-54 and G23-14, respectively. The Zn abundance in four stars including G251-54 was higher than the solar value (Fig. 4l). Our mean zinc abundance was [Zn/Fe] = +0.16, with a small scatter about the mean.

Yttrium and Barium

Heavy (c $Z > 37$), neutron-rich elements are synthesized in processes involving successive neutron captures by target nuclei. Two types of such process are distinguished, depending on the associated neutron flux: the *s* process (if the neutron flux is low and there is enough time for a beta decay to occur between successive neutron captures) and the *r* process (if the neutron density is high enough for the beta-decay rate to be much lower than the neutron-capture rate). The latter process is not as well understood as the former. Although there is general agreement that the *r* process takes place mainly in supernova explosions of massive stars (see, e.g., [79]), at least ten possible mechanisms have been suggested to explain the production of *r*-process elements [79, 80]. A considerable fraction (up to ≈20%) of the lighter elements in this group (including yttrium) that are classified as *s*-process elements are produced via the so-called weak component of the *s* process. This is believed to be activated in the cores of massive stars in the helium-burning stage [81–83]. Heavier *s*-process elements, including barium, are synthesized primarily via the main component of the *s* process, which is now believed to act during thermal pulsations of intermediate- and low-mass stars on the asymptotic giant branch [84–87]. Cameron [88] and Kappeler *et al.* [87, 89, 90] computed the relative contributions of the *s* and *r* processes to the abundance of heavy elements in the solar system. Table 4 gives the corresponding results for yttrium and barium adopted from Gratton and Sneden [91]. Table 3 lists the abundances of these elements that we obtained for the stars in our sample, and Figs. 6a and 6b compare these data to the results of Gratton and Sneden [91] and Zhao and Magain [92] for Y and of Gratton and Sneden [91] for Ba.

The mean abundances for five of the stars are [Y/Fe] = +0.05 dex and [Ba/Fe] = +0.07 and, as is evident from the figure, agree well with earlier published data. As was the case with other elements, we found G251-54 to be significantly deficient in Y and Ba—[Y/Fe] = −0.7 and [Ba/Fe] = −1.35. Carney *et al.* [16] report a relative abundance of [Ba/Fe] = −1.84 for G251-54, which is 0.5 dex lower than our result. This discrepancy is probably due to the fact that Carney *et al.* [16] determined the Ba abundance from the BaII resonance line at 4554 Å, which can underestimate the abundance by up to −0.5 dex compared to those derived from other Ba lines (see [16] for a discussion of this effect).

7. RESULTS AND DISCUSSION

In this paper, we have reported the chemical compositions of six metal-poor stars including G251-54, which has anomalous chemical composition compared to stars of similar metallicity. The remaining five stars, which have metallicities of $-1.6 < [Fe/H] < -1.3$, have relative elemental abundances typical of this metallicity interval (Table 3, Figs. 3, 4, 6), and we used these abundances as reference values when considering the results for G251-54.

The atmospheric chemical composition of G251-54 was first investigated by Carney *et al.* [16], who reported the star's abundances of oxygen, α-process elements (Mg, Ca, Ti), and Ba and Li. We have presented here results for these and a number of other elements, including Na and Si, iron-group elements (Sc, Cr, Mn, Ni, Cu, Zn), and Y. Consideration of a larger number of elements should aid in the interpretation of the measured abundances. Our results confirm those of Carney *et al.* [16]—most elements are significantly underabundant relative both to stars of similar metallicity and to the Sun. In particular, the oxygen underabundance relative to other metal-poor stars is δ[O/Fe] = −0.34. This deficit is even

more pronounced for α-process elements: $\delta[\alpha/\mathrm{Fe}] = -0.62$. About the same deficits are found for Na and Sc—so-called intermediate elements with odd numbers of protons in their nuclei. An even larger deficit is observed for s-process elements, especially Ba, whose abundance is 1.42 dex lower than in other metal-poor stars; the deficit for Y is −0.75 dex.

Interestingly, different α-process elements appear to have different deficits; the underabundance of Mg and Ti is −0.56 dex but is even greater for Si and Ca: −0.69 dex. This may indicate that these elements are synthesized via different mechanisms from different sources and, in particular, with different contributions from type-Ia supernovae.

Another result of at least equal importance is that we found no deficits for a number of iron-peak elements (Cr, Ni, Zn), whose abundances are in full agreement with those found for the other stars studied. At the same time, deficits are observed for Mn and Cu, which are also classified as iron-peak elements, but have odd numbers of protons in their nuclei. We derived the abundances of these two elements using fairly weak lines, so that the accuracy of these results is lower than for the other elements. However, since measuring very weak lines in noisy spectra can only overestimate the equivalent widths, we should effectively obtain upper limits for the abundances of these two elements; i.e., the conclusion that there are deficits for Mn and Cu stands. Interestingly, like G251-54, the star G23-14 exhibited some deficit of these two elements compared to the other stars. Finally, the lithium abundance for G251-54 is in full agreement with the typical value for stars with similar parameters.

The nucleosynthesis history during the formation of a star with a chemical composition similar to that of G251-54 should differ from the usual scenario for the vast majority of stars studied earlier. The nucleosynthesis history of G251-54 may have common features with those of the young globular clusters Palomar 12 and Ruprecht 106 [16]. Brown *et al.* [17, 93] found $[\mathrm{O/Fe}] = +0.05$ and $[\alpha/\mathrm{Fe}] = -0.2$ for Ruprecht 106 and $[\alpha/\mathrm{Fe}] = -0.6$ for Palomar 12, which are significantly different from the abundances of α-process elements in "normal" metal-poor stars. On the other hand, the abundance of Ba in these globular clusters is normal [17]. Carney *et al.* [16] investigated the question of whether the chemical compositions of these globular clusters and G251-54 were related to their Galactocentric distances (and thus to the region of their formation). The Galactocentric distances of Palomar 12 and Ruprecht 106 are 14 and 17 kpc, respectively. A maximum Galactocentric distance of 22 kpc was derived for G251-54 based on its space velocity. Thus, in all three cases, we find anomalous chemical compositions combined with large apogalactic distances.

In this regard, it is interesting to compare the abundances for G251-54 with those for stars that formed in the outer regions of the Galactic halo but then ended up in the solar neighborhood. Carney *et al.* [22] identified about one hundred such stars with apogalactic distances exceeding 15 kpc. However, an analysis of the published results for ten of these stars revealed no anomalies: only one (BD—6°855) is deficient in silicon [94]. It follows that the anomalous chemical composition observed in G251-54 is uncharacteristic even for stars brought into the solar neighborhood from the outer halo.

The origin of stars with anomalous chemical compositions similar to that observed for G251-54 and the two globular clusters noted above could possibly be explained if there was a strong enrichment of their parent gaseous clouds in products of Galactic nucleosythesis, but this enrichment took place after the formation of the halo, when the abundances of α-process elements reached their solar values. This process could have resulted in an underabundance of metals (due to mixing with the initial unenriched matter) but should have no effect on the relative abundances of various elements with respect to iron. If such a scenario were possible, we could observe metal-poor stars with solar abundances of α-process elements. This explanation may be relevant for Palomar 12, but it is not appropriate for G251-54 or Ruprecht 106, since these objects show substantially stronger deficits of α-process elements. Furthermore, this interpretation cannot explain the observed very strong underabundance of s-process and other elements.

In our opinion, a more likely scenario is the capture by the Milky Way of small satellite galaxies in which, owing to the low mass of the initial gaseous clouds, star formation followed a significantly different pattern. In particular, the star-formation process in such low-mass clouds could have bypassed the stage of enrichment with the products of type-II supernova explosions and continued until the onset of the phase of type-Ia supernovae. In this case, the atmospheres of stars formed in such clouds should be extremely underabundant in elements synthesized during the evolution of single, massive stars. These elements include oxygen, α-process elements, sodium, r-process elements and, partly, s-process elements. Because precisely these elements are underabundant in G251-24 relative to other metal-poor stars, a scenario in which the star formed in an isolated, low-mass cloud seems plausible. The underabundance of elements with odd numbers of protons (Na, Sc, Mn, Cu), whose synthesis depends strongly on the metallicity of the region in which the nuclear reactions

take place, and the normal abundances of such iron-peak elements as Cr, Ni, and Zn also fit into this scenario. We can also take into account the fact that Ba is synthesized primarily in low-mass stars on the asymptotic giant branch and that such stars reach this stage after the onset of the phase of type-Ia supernovae. In this case, the overderabundance of Ba in the atmosphere of G251-54 can also be explained in this scheme.

Stars like G251-54 are of special interest from the viewpoint of the chemical evolution of the Milky Way, since they reveal a chemical-enrichment history different from that shown by other metal-poor stars. In addition, large apogalactic distances and unusual atmospheric chemical compositions may be indicative of an extragalactic origin for these stars and their subsequent capture by the Milky Way. Combining kinematic and chemical analyses of such stars enables us to analyse, not only the history of the chemical evolution of the Milky Way and its nearest neighborhood, but also the processes of mergers with small satellites.

8. ACKNOWLEDGMENTS

This work was supported by the Russian Foundation for Basic Research (project nos. 01-02-16093 and 00-02-17689) and the National Natural Science Foundation of China (grant nos. 10173014 and NKBRSF 1999075406).

REFERENCES

1. V. G. Klochkova and V. E. Panchuk, Pis'ma Astron. Zh. **15**, 236 (1989) [Sov. Astron. Lett. **15**, 102 (1989)].
2. A. O. J. Unsöld, Science **163**, 1015 (1969).
3. B. M. Tinsley, Astrophys. J. **229**, 1046 (1979).
4. V. G. Klochkova and V. E. Panchuk, Izv. SAO **20**, 16 (1985).
5. A. M. Boesgaard, Astrophys. J. **336**, 798 (1989).
6. A. M. Boesgaard and E. D. Friel, Astrophys. J. **351**, 467 (1990).
7. V. G. Klochkova, V. E. Panchuk, and V. V. Tsymbal, Izv. SAO **33**, 41 (1991).
8. V. G. Klochkova, Izv. SAO **34**, 31 (1991).
9. G. H. Smith, in *The Abundance Spread within Globular Clusters: Spectroscopy of Individual Stars,* Ed. by G. Cayrel de Strobel, M. Spite, and T. Lloyd Evans (Obs. de Paris, Paris, 1989), p. 63.
10. S. Basu and N. C. Rana, Astrophys. Space Sci. **196**, 1 (1992).
11. T. K. Suzuki and Y. Yoshii, Astrophys. J. **549**, 303 (2001).
12. M. Spite, in *The Stellar Populations of Galaxies (IAU Symposium 149),* Ed. by B. Barbuy and A. Renzini (Kluwer, Dordrecht, 1992), p. 123.
13. K. Fuhrmann, M. Axer, and T. Gehren, Astron. Astrophys. **301**, 492 (1995).
14. A. McWilliam, G. W. Preston, C. Sneden, and L. Searle, Astron. J. **109**, 2757 (1995).
15. A. McWilliam, G. W. Preston, C. Sneden, and S. Shectman, Astron. J. **109**, 2736 (1995).
16. B. W. Carney, J. S. Wright, C. Sneden, *et al.*, Astron. J. **114**, 363 (1997).
17. J. A. Brown, G. Wallerstein, and D. Zucker, Astron. Soc. Pac. Conf. Ser. **92**, 355 (1996).
18. A. McWilliam, Ann. Rev. Astron. Astrophys. **35**, 503 (1997).
19. V. G. Klochkova and V. E. Panchuk, Astron. Zh. **73**, 912 (1996) [Astron. Rep. **40**, 829 (1996)].
20. S. V. Ermakov and V. G. Klochkova, Bull. Spec. Astrophys. Obs. **46**, 110 (1998).
21. V. G. Klochkova, S. V. Ermakov, and V. E. Panchuk, Astrophys. Space Sci. **265**, 185 (1999).
22. B. W. Carney, D. W. Latham, J. B. Laird, and L. A. Aguilar, Astron. J. **107**, 2240 (1994).
23. V. E. Panchuk, I. D. Najdenov, V. G. Klochkova, *et al.*, Bull. Spec. Astrophys. Obs. **44**, 127 (1998).
24. G. A. Galazutdinov, Preprint SAO No. 92 (1992).
25. J. Tomkin, M. Lemke, D. L. Lambert, and C. Sneden, Astron. J. **104**, 1568 (1992).
26. J. R. King, C. P. Deliyannis, and A. M. Boesgaard, Astron. J. **112**, 2839 (1996).
27. V. G. Klochkova, G. A. Mal'kova, and V. E. Panchuk, Bull. Spec. Astrophys. Obs. **39**, 5 (1996).
28. A. Alonso, S. Arribas, and C. Martinez-Roger, Astron. Astrophys. **313**, 873 (1996).
29. R. G. Gratton, E. Carretta, and F. Castelli, Astron. Astrophys. **314**, 191 (1996).
30. V. V. Tsymbal, Astron. Soc. Pac. Conf. Ser. **108**, 198 (1996).
31. The Hipparcos and Tycho Catalogues, ESA SP-1200 (ESA, 1997).
32. D. A. van den Berg, F. J. Swenson, F. J. Rogers, *et al.*, Astrophys. J. **532**, 430 (2000).
33. L. A. Balona, Mon. Not. R. Astron. Soc. **268**, 119 (1994).
34. R. L. Kurucz, in *The Stellar Population of Galaxies (IAU Symposium 149),* Ed. by B. Barbuy and A. Renzini (Kluwer, Dordrecht, 1992), p. 225.
35. R. L. Kurucz, CD-ROM 18 (SAO, Cambridge, 1993).
36. C. A. Prieto and R. J. G. López, Astron. Astrophys., Suppl. Ser. **131**, 431 (1998).
37. R. E. Luck and H. E. Bond, Astrophys. J. **244**, 919 (1981).
38. R. L. Kurucz, CD-ROM 18 (SAO, Cambridge, 1993).
39. W. L. Wiese, M. W. Smith, and B. M. Glennon, *Atomic Transition Probabilities*, Vol. 1, NSRDS-NBS 4.
40. P. E. Nissen and W. J. Shuster, Astron. Astrophys. **326**, 751 (1997).
41. T. N. Chang, Phys. Rev. A **41**, 4922 (1990).
42. T. Garz, Astron. Astrophys. **26**, 471 (1973).
43. D. L. Lambert and B. Warner, Mon. Not. R. Astron. Soc. **138**, 181 (1968).
44. Y. Q. Chen, P. E. Nissen, G. Zhao, *et al.*, Astron. Astrophys., Suppl. Ser. **141**, 491 (2000).
45. G. Smith and D. St. J. Raggett, J. Phys. B **14**, 4015 (1981).

46. J. E. Lawler and J. T. Dakin, J. Opt. Soc. Am. B **6**, 1457 (1989).
47. G. A. Martin, J. R. Fuhr, and W. L. Wiese, J. Phys. Chem. Ref. Data **17**, Suppl. 3 (1988).
48. J. R. Fuhr, G. A. Martin, and W. L. Wiese, J. Phys. Chem. Ref. Data **17**, Suppl. 4 (1988).
49. E. A. Gurtovenko and R. I. Kostyk, in *Fraunhofer Spectra and a System of Solar Oscillator Strengths,* Ed. by M. Ya. Orlov [in Russian] (Naukova Dumka, Kiev, 1989).
50. T. A. Ryabchikova, G. M. Hill, J. D. Landstreet, *et al.*, Mon. Not. R. Astron. Soc. **267**, 697 (1994).
51. A. Bizzarri, M. C. E. Huber, A. Noels, *et al.*, Astron. Astrophys. **273**, 707 (1993).
52. P. S. Barklem, N. Piskunov, and B. J. O'Mara, Astron. Astrophys., Suppl. Ser. **142**, 467 (2000).
53. R. L. Kurucz, CD-ROM 20-22 (SAO, Cambridge, 1994).
54. M. E. Wickliffe and J. E. Lawler, Astrophys. J., Suppl. Ser. **110**, 163 (1997).
55. J. Reader and C. J. Sansonetti, Phys. Rev. A **33**, 1440 (1986).
56. W. L. Wiese and G. A. Martin, *Wavelengths and Transition Probabilities for Atoms and Atomic Ions* (National Bureau of Standards, Washington, DC, 1980), NSRDS-NBS, no. 68.
57. F. Kupka, N. E. Piskunov, T. A. Ryabchikova, *et al.*, Astron. Astrophys., Suppl. Ser. **138**, 119 (1999).
58. T. A. Ryabchikova, N. E. Piskunov, H. C. Stempels, *et al.*, in *Atomic Spectra and Oscillator Strengths,* Phys. Scr. **83**, 162 (1999).
59. N. E. Piskunov, F. Kupka, T. A. Ryabchikova, *et al.*, Astron. Astrophys., Suppl. Ser. **112**, 525 (1995).
60. J. A. Thorburn, Astrophys. J. **421**, 318 (1994).
61. C. A. Pilachowski, C. Sneden, and J. Booth, Astrophys. J. **407**, 699 (1993).
62. T. V. Mishenina, S. A. Korotin, V. G. Klochkova, and V. E. Panchuk, Astron. Astrophys. **353**, 978 (2000).
63. T. Tsujimoto, K. Nomoto, Y. Yoshii, *et al.*, Mon. Not. R. Astron. Soc. **277**, 945 (1995).
64. R. G. Gratton and C. Sneden, Astron. Astrophys. **204**, 193 (1988).
65. K. Nomoto, Y. Tsujimoto, and H. Yamaoka, in *Elements and the Cosmos,* Ed. by M. G. Emunds and R. Terlevich (Cambridge Univ. Press, Cambridge, 1992), p. 55.
66. R. G. Gratton and C. Sneden, Astron. Astrophys. **178**, 179 (1987).
67. M. Samland, Astrophys. J. **496**, 155 (1998).
68. F. X. Timmes, S. E. Woosley, and T. A. Weaver, Astrophys. J., Suppl. Ser. **98**, 617 (1995).
69. Y. Takeda, K.-I. Kato, Y. Watanabe, and K. Sadakane, Publ. Astron. Soc. Jpn. **48**, 511 (1996).
70. R. C. Peterson, Astrophys. J. **244**, 989 (1981).
71. R. E. Luck and H. E. Bond, Astrophys. J. **271**, L75 (1983).
72. K. K. Gilroy, C. Sneden, C. A. Pilachowski, and J. J. Cowan, Astrophys. J. **327**, 298 (1988).
73. R. G. Gratton and C. Sneden, Astron. Astrophys. **241**, 501 (1991).
74. R. G. Gratton, Astron. Astrophys. **208**, 171 (1989).
75. S. G. Ryan, J. E. Norris, and T. C. Beers, Astrophys. J. **471**, 254 (1996).
76. C. Sneden and D. A. Crocker, Astrophys. J. **335**, 406 (1988).
77. C. Sneden, R. G. Gratton, and D. A. Crocker, Astron. Astrophys. **246**, 354 (1991).
78. F. Matteucci, C. M. Raiteri, M. Busso, *et al.*, Astron. Astrophys. **272**, 421 (1993).
79. G. J. Mathews, G. Bazan, and J. J. Cowan, Astrophys. J. **391**, 719 (1992).
80. G. J. Mathews and J. J. Cowan, Nature **345**, 491 (1990).
81. S. Lamb, W. M. Howard, J. W. Truran, and I. Iben, Jr., Astrophys. J. **217**, 213 (1977).
82. R. A. Malaney and A. I. Boothroyd, Astrophys. J. **320**, 866 (1987).
83. C. M. Raiteri, M. Busso, R. Gallino, *et al.*, Astrophys. J. **371**, 665 (1991).
84. I. Jr. Iben and A. Renzini, Astrophys. J. **259**, L79 (1982).
85. D. E. Hollowell and I. Iben, Jr., Astrophys. J. **340**, 966 (1989).
86. R. Gallino, M. Busso, G. Picchio, *et al.*, Astrophys. J. **334**, L45 (1988).
87. F. Kappeler, R. Gallino, M. Busso, *et al.*, Astrophys. J. **354**, 630 (1990).
88. A. G. W. Cameron, Astrophys. Space Sci. **82**, 123 (1982).
89. F. Kappeler, H. Beer, and K. Wisshak, Rep. Prog. Phys. **52**, 945 (1989).
90. F. Kappeler, W. R. Zhao, H. Beer, and U. Ratzel, Astrophys. J. **355**, 348 (1990).
91. R. G. Gratton and C. Sneden, Astron. Astrophys. **287**, 927 (1994).
92. G. Zhao and P. Magain, Astron. Astrophys. **244**, 425 (1991).
93. J. A. Brown, G. Wallerstein, and D. Zucker, Bull. Am. Astron. Soc. **27**, 1404 (1995).
94. B. W. Carney and D. W. Latham, Astrophys. J. **298**, 803 (1985).

Translated by A. Dambis

Astronomy Reports, Vol. 46, No. 11, 2002, pp. 887–899. Translated from Astronomicheskiĭ Zhurnal, Vol. 79, No. 11, 2002, pp. 986–998.

Stellar Fluxes in Numerical Dynamical Models of Open Clusters

V. M. Danilov

Astronomical Observatory, Ural State University, pr. Lenina 51, Yekaterinburg, 620083 Russia

Received January 25, 2002; in final form, May 23, 2002

Abstract—Fluxes of stars in models of open clusters that are nonstationary in the regular field of the cluster are analyzed. An equilibrium distribution function describes the state of these models from the beginning of their dynamical evolution. Violent relaxation in the open-cluster models proceeds under equilibrium conditions in phase space and does not result in virial equilibrium. The cluster relaxation times in the one-dimensional spaces of a number of stellar-motion parameters are estimated. The stellar fluxes are anisotropic in some two-dimensional parameter spaces. Such open-cluster models exhibit a number of manifestations of self-organization (an energy flux toward the center of the cluster and a transfer of energy from large-scale to small-scale motions, periodic decreases in the entropies of the cluster models with a period equal to that of oscillations of the regular field of the cluster, etc.). It is concluded that violent relaxation represents one form of self-organization in such systems. © *2002 MAIK "Nauka/Interperiodica".*

1. INTRODUCTION

The dynamical evolution of open-cluster models that are nonstationary in the regular field of the cluster [1, 2] by the end of the first violent-relaxation time τ_{vr} [3] are characterized by an equilibrium distribution of stars over the three parameters of stellar motion ε, l, and ε_ζ (the energy, angular momentum, and energy of the star perpendicular to the Galactic plane, all per unit mass of the star). These open-cluster models [1, 2] attain neither virial nor thermodynamical equilibrium as t increases, and the virial coefficient for the cluster models at $t > \tau_{vr}$ continues to oscillate with nearly constant amplitude and the period P_r. The equilibrium of open-cluster models pointed out in [1, 2] is not complete, since the distribution of stars in the coordinate and velocity spaces and the potential of the regular forces of the cluster model vary with the period P_r, and the phase-space density function (PSDF) remains well conserved on time scales on the order of P_r.

Variations in the number density of stars in any region of the phase space are due to differences in the incoming and outgoing fluxes of stars. Therefore, to understand the dynamics of the processes that lead to the state of incomplete equilibrium in the open-cluster models of [1, 2], it is of interest to analyze the properties of stellar fluxes in the phase space, in spaces of the variables ε, l, and ε_ζ, and in a number of other spaces describing the cluster models.

The dispersions of the increments of ε, l, and ε_ζ derived from the distributions of the stellar fluxes in ε, l, and ε_ζ provide insight into the relaxation times of the open-cluster models in these spaces. According to El-Zant [4], for a number of reasons, the relaxation time of a system of N gravitating bodies can differ substantially from the time scale for the development of instabilities in the trajectories of these bodies in phase space. Danilov [1, 5] estimated the local violent-relaxation times t_r from data on the instability of the PSDFs of open-cluster models against small initial perturbations of the phase-space coordinates of the stars (the instability of the PSDF is due to instability of the stellar trajectories in the cluster models). Estimates of the relaxation rates of open-cluster mosels based on the properties of stellar fluxes in spaces of ε, l, and ε_ζ have not previously been made, but they are of considerable interest for studies of the diffusion of stars in the cluster-model phase space.

Studies of stellar fluxes in open-cluster models indicate a number of manifestations of self-organization. Consideration of the entropy of the open-cluster models in connection with self-organization effects is of interest.

In the current paper, we analyze the behavior of fluxes of stars in open-cluster models, investigate the characteristic features of violent relaxation and the incomplete equilibrium in these systems, and develop a method for the computation and analysis of the properties of the stellar fluxes.

2. DESCRIPTION OF MODELS

Following [1, 2], let us consider a cluster containing $N = 500$ stars moving in the Galactic plane in a circular orbit of radius 8200 pc around the Galactic center. At the initial time $t = 0$, the cluster is modeled

1063-7729/02/4611-0887$22.00

Parameters of OC models

No.	R_1/R_2	N_1/N_2	N_1	Use of formula (1)	R_2/R_t	$\langle R\rangle/R_t$	$t_{r,h}$	τ_ε	τ_l	τ_{ε_ζ}	σ_v/σ_r
1	0.24	0.25	100	+	0.9	0.57	1.5	5.2	2.2	1.2	2.8
2	0.24	0.25	100	+	0.7	0.45	1.2	4.4	3.2	0.9	2.3
3	0.634	4.00	400	+	0.8	0.42	1.9	2.7	3.2	1.1	1.3
4	0.24	0.25	100	−	0.7	0.45		3.9	2.9	0.7	2.4
5	0.4	4.00	400	+	0.9	0.35		2.7	2.5	0.6	1.7

as a system of two gravitating spheres with coincident centers of mass, imitating the halo and core. We analyzed five such open-cluster models, whose parameters are summarized in the Table. The first column gives a sequence of numbers identifying the models. The initial parameters R_1/R_2 and N_1/N_2 (columns 2, 3) of the first four models satisfy the relation $R_1/R_2 \simeq 0.39 \times (N_1/N_2)^{0.35}$, based on observational data [6]. Here, R_1 and R_2 are the radii of the cluster core and halo, respectively, and N_1 and N_2 the numbers of stars in the core and halo, respectively (the initial N_1 is given in column 4). The fifth model does not obey this relation between R_1/R_2 and N_1/N_2. The masses of the stars in the models are equal to $1M_\odot$.

We used the equations of stellar motion (5.517)–(5.519) from [7] and analyzed the motions of the cluster stars in a rotating coordinate system (ξ, η, ζ) fixed to the cluster center of mass. The ξ, η, and ζ axes are directed from the cluster center of mass toward the Galactic center, along the motion of the cluster in the Galactic plane, and perpendicular to the Galactic plane, respectively. We adopted the Galactic potential in the form suggested in [8]. We specified the initial positions and velocities of the stars in the models using a random-number generator, in accordance with the technique described in [1] for cluster model 2 (model 1 of the current paper coincides with model 2 of [1] at $t = 0$). At $t = 0$, the cluster model does not rotate relative to external galaxies, and the initial stellar number densities at various points of the halo and core subsystems are approximately constant in (ξ, η, ζ).

At $t = 0$, cluster models 1–3 and 5 obey the conditions of virial equilibrium for isolated clusters, and the absolute values of the velocities of the stars of subsystem i can be computed using the formula

$$v_i = \sqrt{C_i U(r)}, \quad i = 1, 2, \tag{1}$$

where $r = |\mathbf{r}|$, $\mathbf{r} = (\xi, \eta, \zeta)$ is the radius vector of the star in the cluster, $U(r)$ is the gravitational potential of the cluster, and the subscripts $i = 1, 2$ correspond to the cluster core and halo, respectively. The constants C_i are chosen so that the cluster and its subsystems obey the conditions of virial equilibrium at $t = 0$, neglecting the effect of the gravitational field of the Galaxy [9]. The use of (1) when setting the initial phase-space density functions in models 1–3 and 5 is indicated by a plus sign in column 5 of the table. In model 4, the absolute values of all the stellar velocities are assumed to be the same at $t = 0$ and to correspond to virial equilibrium for an isolated cluster. Therefore, models 1–5 do not obey the condition of virial equilibrium in the gravitational field of the Galaxy at $t = 0$.

We smoothed the force functions on the right-hand sides of the stellar equations of motions (see [10] for a description of the smoothing technique and smoothing parameter used).

The stellar equations of motion were integrated using eighth- and ninth-order Runge–Kutta methods and grid functions adopted from [11], with a precision of 15–16 decimal digits. The maximum relative errors in the computed "energy" E [see (5.522) in [7]] did not exceed 2.8×10^{-13}, 9.0×10^{-14}, 1.1×10^{-13}, 8.0×10^{-14}, and 1.3×10^{-12} in cluster models 1, 2, 3, 4, and 5, respectively. The statistical criterion for the accuracy of the computations of the phase-space density functions [12] remained satisfied for evolutionary time intervals of $t_0/\tau_{vr} = 2.7$, 3.1, 3.6, 2.45, and 1.8 for models 1, 2, 3, 4, and 5, respectively (here, as in [1, 2], we take the initial violent-relaxation times for the cluster models to be $\tau_{vr} = 2.6\overline{t}_{\rm cr}$, where $\overline{t}_{\rm cr}$ is the mean initial crossing time for a star in the cluster).

Let R_t be the tidal stability radius of the cluster in the Galactic field computed in accordance with [13], $\langle R\rangle$ the mean distance of the star from the cluster center, and $\langle\rho\rangle_i$ the cluster-averaged mean initial density for model i $(i = 1, \ldots, 5)$. The initial values of R_2/R_t and $\langle R\rangle/R_t$ for our models are listed in columns 6 and 7 of the table. We can see that cluster models 1 and 5 have the lowest and highest initial densities $\langle\rho\rangle_1$, with $\frac{\langle\rho\rangle_5}{\langle\rho\rangle_1} \simeq 4.34$.

The degree of nonstationarity of the models in the regular field is determined by the amplitude of oscillations of the virial coefficient $\delta\alpha$, where $\alpha = 2E_c/W$, $E_c = T + W$, and T and W are the kinetic and potential energies of the cluster, including the effect of the gravitational field of the Galaxy (as in [1, 2, 5]). The mean ratios $\delta\alpha$ of the amplitudes of the oscillations of the virial coefficient α to the value $\alpha = \alpha_v$ averaged over the period P_r of oscillations of the regular field are 0.53 ± 0.09, 0.14 ± 0.02, 0.06 ± 0.03, 0.09 ± 0.05, and 0.08 ± 0.02 for models 1, 2, 3, 4, and 5, respectively. Such degrees of nonstationarity are also typical of real open clusters [6].

3. MAIN FORMULAS AND NOTATION

Let us consider fluxes of stars in the space of the energy ε. We will number the ε values for the cluster stars in order of increasing ε (in this case, the ordinal numbers p of the stars whose phase-space coordinates are used when computing ε do not coincide with the ordinal numbers for the ε values). Following [1], we subdivide all the cluster stars (500 objects) into groups of 50 stars in order of increasing ε at some time t. Then, the stars with energies $\varepsilon' \in (\varepsilon_{50\times(i-1)+1}, \varepsilon_{50\times i}] \equiv E_i(t)$ specify the interval $\Delta\varepsilon_i = \varepsilon_{50\times i} - \varepsilon_{50\times(i-1)+1}$ in ε space, where $i = 2, \ldots, 10$. When $i = 1$, we must consider the interval $\varepsilon' \in [\varepsilon_{50\times(i-1)+1}, \varepsilon_{50\times i}] \equiv E_1(t)$ such that the star with the minimum energy ε_1 is also included. Let the number of stars in the ith ε interval at time t be $n_i^{(\varepsilon)}(t)$. Let $n^{(\varepsilon)}(i,j)$ denote the number of stars passing from the ith to the jth interval in the ε space during the time Δt. This number can be obtained from the stellar phase-space coordinates for the cluster model at times t and $t + \Delta t$:

$$n^{(\varepsilon)}(i,j) = \sum_{p=1}^{500} \delta_p, \quad \text{where} \tag{2}$$

$$\delta_p = \begin{cases} 1, & \text{if } \varepsilon_p(t) \in E_i(t),\ \ \varepsilon_p(t+\Delta t) \in E_j(t+\Delta t) \\ 0, & \text{in all other cases.} \end{cases}$$

Note that, generally speaking, the $\Delta\varepsilon_i$ values at times t and $t + \Delta t$ are not equal for any $i = 1, \ldots, 10$. The quantity $n^{(\varepsilon)}(i,j)/\Delta t$ is equal to the flux of stars emerging from the interval $E_i(t)$ into the interval $E_j(t + \Delta t)$ in ε space. In the framework of the method adopted to specify the $\Delta\varepsilon_j$ values, we have for the total number of stellar transitions into the interval $\Delta\varepsilon_j$ during the time Δt

$$\sum_{i=1}^{10} n^{(\varepsilon)}(i,j) = 50, \quad j = 1, \ldots, 10. \tag{3}$$

After equilibrium is established in the ε space for the open-cluster models, the stellar-transition matrix $n^{(\varepsilon)}(i,j)$ should become symmetric (or close to symmetric).

The average number of stellar transitions by j intervals in ε during the time Δt is

$$\nu^{(\varepsilon)}(j) \tag{4}$$
$$= \begin{cases} \frac{1}{10+j} \sum\limits_{i=1-j}^{10} n^{(\varepsilon)}(i, i+j), & j = -9, \ldots, -1 \\ \frac{1}{10-j} \sum\limits_{i=1}^{10-j} n^{(\varepsilon)}(i, i+j), & j = 0, 1, \ldots, 9. \end{cases}$$

In (4), we have averaged the numbers of all possible stellar transitions by j intervals in ε. The values $j > 0$ (< 0) correspond to an increase (decrease) of the star's energy ε as a result of such a transition. The function $\nu^{(\varepsilon)} = \nu^{(\varepsilon)}(j)$ is the j distribution of the mean numbers of stellar transitions in ε during the time Δt. If this distribution is symmetric about $j = 0$, there is a balance of stellar transitions in ε space.

The degree of asymmetry of the matrix $n^{(\varepsilon)}(i,j)$ can be expressed by the single quantity

$$\psi^{(\varepsilon)} = \frac{\sum\limits_{j=1}^{10}\sum\limits_{i=1}^{10} |n^{(\varepsilon)}(i,j) - n^{(\varepsilon)}(j,i)|}{\frac{1}{2}\sum\limits_{j=1}^{10}\sum\limits_{i=1}^{10} (n^{(\varepsilon)}(i,j) + n^{(\varepsilon)}(j,i))}. \tag{5}$$

It is convenient to use $\psi^{(\varepsilon)}$ to analyze the time dependence of disruptions of the balance of the corresponding stellar transitions between intervals in ε.

Let us now consider stellar transitions in the two-dimensional (r, v) space of the cluster models (here, v is the absolute value of the star's velocity in the cluster). We subdivide the region in (r, v) occupied by the cluster-model stars as we did for the ε space. However, we now assume that the number of stars $n_{ij}^{(r,v)}(t)$ located in the cell $(\Delta r_i, \Delta v_j)$ at time t is equal to five, $i, j = 1, \ldots, 10$. For brevity, we have used the term "cell $(\Delta r_i, \Delta v_j)$" to denote the region of (r, v) space with the coordinates $r' \in [r_{50\times(i-1)+1}, r_{50\times(i-1)+1} + \Delta r_i] \equiv L_i(t)$, $v' \in [v_{50\times(j-1)+1}, v_{50\times(j-1)+1} + \Delta v_j] \equiv V_j(t)$ at $i, j = 2, \ldots, 10$. In the case $i, j = 1$, $r' \in L_1(t) \equiv [r_1, r_1 + \Delta r_1]$, $v' \in V_1(t) \equiv [v_1, v_1 + \Delta v_1]$. Here, r and v are numbered in increasing order (the numbers p for the stars whose phase-space coordinates are used to compute r and v do not coincide with the numbers for r and v). With this partition of (r, v) space into cells, the number of stars in the interval $r' \in L_i(t)$ is equal to 50 (for any $i = 1, \ldots, 10$). In the notation used, we have

$r_{50\times i} = r_{50\times(i-1)+1} + \Delta r_i$. A similar relation can be written for the quantities v.

Let $n^{(r,v)}(i,j,k,m)$ be the number of stars in (r,v) space that move from the cell $(\Delta r_i, \Delta v_j)$ defined at time t to the cell $(\Delta r_k, \Delta v_m)$ defined at time $t+\Delta t$. We obtain from the stellar phase-space coordinates for the cluster model at times t and $t+\Delta t$

$$n^{(r,v)}(i,j,k,m) = \sum_{p=1}^{500} \delta_p, \quad \text{where} \quad \delta_p \qquad (6)$$

$$= \begin{cases} 1, & \text{if } r_p(t) \in L_i(t), r_p(t+\Delta t) \in L_k(t+\Delta t), \\ & v_p(t) \in V_j(t), v_p(t+\Delta t) \in V_m(t+\Delta t) \\ 0, & \text{in all other cases.} \end{cases}$$

The total number of stellar transitions to the cell $(\Delta r_k, \Delta v_m)$ during the time Δt is

$$\sum_{i=1}^{10}\sum_{j=1}^{10} n^{(r,v)}(i,j,k,m) = 5, \ \ k,m = 1,\ldots,10. \quad (7)$$

Relations (3) and (7) can be used to monitor the accuracy of the computation of $n^{(\varepsilon)}(i,j)$ and $n^{(r,v)}(i,j,k,m)$.

Let us specify the $i = i_0$ and $k = k_0$ values in the matrix $n^{(r,v)}(i,j,k,m)$. The mean number of stellar transitions $\nu^{(r,v)}_{i_0,k_0}(J)$ by $J = m - j$ intervals in v accompanied by transitions of these stars in r from the interval $L_{i_0}(t)$ to the interval $L_{k_0}(t+\Delta t)$ can be computed using formulas like (4), with $n^{(\varepsilon)}(i,j)$ replaced by the matrix $n^{(r,v)}(i_0,j,k_0,j+J)$ and the summation performed over j. We can similarly compute the mean number of stellar transitions by $I = k - i$ intervals in r for specified values $j = j_0$ and $m = m_0$ in the case of stellar transitions in v from the interval $V_{j_0}(t)$ to the interval $V_{m_0}(t+\Delta t)$. Generalizing (4) to the case of stellar transitions in a two-dimensional space yields expressions of the form

$$\nu^{(r,v)}(I,J) = \begin{cases} \frac{1}{(10+I)(10+J)} \sum\limits_{j=1-J}^{10}\sum\limits_{i=1-I}^{10} n^{(r,v)}(i,j,i+I,j+J), & I,J = -9,\ldots,-1 \\ \frac{1}{(10-I)(10+J)} \sum\limits_{j=1-J}^{10}\sum\limits_{i=1}^{10-I} n^{(r,v)}(i,j,i+I,j+J), & I = 0,1,\ldots,9; J = -9,\ldots,-1 \\ \frac{1}{(10+I)(10-J)} \sum\limits_{j=1}^{10-J}\sum\limits_{i=1-I}^{10} n^{(r,v)}(i,j,i+I,j+J), & I = -9,\ldots,-1; J = 0,1,\ldots,9 \\ \frac{1}{(10-I)(10-J)} \sum\limits_{j=1}^{10-J}\sum\limits_{i=1}^{10-I} n^{(r,v)}(i,j,i+I,j+J), & I,J = 0,1,\ldots,9. \end{cases} \quad (8)$$

In our case, the numbers of stars $n^{(r,v)}_{i,j}(t)$ are small (equal to five). Therefore, the quantities $\nu^{(r,v)}(I,J)$ should also be small and exhibit random fluctuations. In this situation, it is useful to analyze not only the distribution $\nu^{(r,v)} = \nu^{(r,v)}(I,J)$, but also the total ("synthetic") distribution $\nu^{(r,v)}(I,J)$ over all times in the time interval t_0 for the given open-cluster model.

The degree of symmetry of the matrix $n^{(r,v)}(i,j,k,m)$ can be expressed by the single quantity

$$\psi^{(r,v)} = \frac{\sum\limits_{k=1}^{10}\sum\limits_{i=1}^{10}\sum\limits_{m=1}^{10}\sum\limits_{j=1}^{10} |n^{(r,v)}(i,j,k,m) - n^{(r,v)}(k,m,i,j)|}{\frac{1}{2}\sum\limits_{k=1}^{10}\sum\limits_{i=1}^{10}\sum\limits_{m=1}^{10}\sum\limits_{j=1}^{10} (n^{(r,v)}(i,j,k,m) + n^{(r,v)}(k,m,i,j))}. \quad (9)$$

The fluxes of stars between intervals and cells in one-and two-dimensional spaces of the stellar-motion parameters in the open-cluster models can be analyzed using (2)–(9), without using data on the time variations of the sizes of the intervals and cells in the spaces considered. The number of stars located in

each such interval or cell is fixed at any time t, so that these time dependences also contain important information about the dynamics of the stellar system and the time evolution of the stellar density distribution in these spaces.

Let $s_v^2 = s_{\dot\zeta}^2/(s_{\dot\xi}^2 + s_{\dot\eta}^2 + s_{\dot\zeta}^2)$ and $\dot\zeta = \frac{d\zeta}{dt}$ and the quantities $\dot\eta$ and $\dot\xi$ be defined in a similar way. Here, $s_{\dot\xi}^2$, $s_{\dot\eta}^2$, and $s_{\dot\zeta}^2$ are the dispersions of the deviations of the $\dot\xi, \dot\eta$, and $\dot\zeta$ coordinates of the stars from their mean values, computed for stars with clustercentric distances $r \le R_t^-$, where R_t^- is the tidal radius of the cluster for stars with "retrograde" orbits [1] (see [10] for the technique used to compute R_t^-). In the evolution of cluster models 1–5, the relations $s_v^2 \simeq 0.3$–0.4 and $s_{\dot\zeta}/s_{\dot\xi} \simeq s_{\dot\zeta}/s_{\dot\eta} \simeq 1.1$–$1.3$ are, on average, satisfied on long time intervals t_0, indicating that the stellar distributions in these models are nearly spherically symmetric. Let $s_r^2 = s_\zeta^2/(s_\xi^2 + s_\eta^2 + s_\zeta^2)$, where s_ξ^2, s_η^2, and s_ζ^2 are determined from the ξ, η, ζ coordinates of the stars in the same way as we determined $s_{\dot\xi}^2$, $s_{\dot\eta}^2$, and $s_{\dot\zeta}^2$ from the coordinates $\dot\xi$, $\dot\eta$, and $\dot\zeta$ when computing s_v^2. In the evolution of models 1–5, the relations $s_r^2 \simeq 0.3$–0.4 and $s_\zeta/s_\xi \simeq s_\zeta/s_\eta \simeq 0.9$–$1.0$ are, on average, satisfied on long time intervals t_0, showing that the distribution of 70–90% of the stars in models 1–5 in (ξ, η, ζ) space can be considered close to spherically symmetric.

Let us now estimate the phase-space volume Q_{ij} occupied by the stars of the cell $(\Delta r_i, \Delta v_j)$ at time t. We will assume that the distributions of stars in the coordinate and velocity spaces for the models are spherically symmetric. We obtain in this case

$$Q_{ij} = \left(\frac{4}{3}\pi\right)^2 (r_{50\times i}^3 - r_{50\times(i-1)+1}^3) \qquad (10)$$
$$\times\, (v_{50\times j}^3 - v_{50\times(j-1)+1}^3), \quad i,j = 1,\ldots,10.$$

In the framework of the method used to specify Δr_i and Δv_j, the phase-space density of the stars in the cell $(\Delta r_i, \Delta v_j)$ of (r, v) space at time t is $f_{ij} = n_{ij}^{(r,v)}(t)/Q_{ij}$, $i,j = 1,\ldots,10$. Using the adopted notation and formula (10.23) of [14], the entropy of the system for the six-dimensional phase space can be written in the form $S = -\sum_{i=1}^{10}\sum_{j=1}^{10}(f_{ij}\ln f_{ij})Q_{ij}$. We then substitute the values $n_{ij}^{(r,v)}(t) = 5$ and $f_{ij} = 5/Q_{ij}$ into the expression for S to obtain after simple manipulation $S = -500\ln 5 + 5\sum_{i=1}^{10}\sum_{j=1}^{10}\ln Q_{ij}$. The dependences $Q_{ij} = Q_{ij}(t)$ $(i,j = 1,\ldots,10)$ fully determine the time variations of S. We therefore define the entropy S of the cluster model to within a constant term and a constant factor as follows:

$$S = \sum_{i=1}^{10}\sum_{j=1}^{10}\ln Q_{ij}. \qquad (11)$$

4. COMPUTATION RESULTS AND DISCUSSION

By time $t \simeq (0.30$–$0.43)\tau_{vr}$, the open-cluster models cease to contract (mainly perpendicular to the Galactic plane), and, at $t > (0.3$–$0.6)\tau_{vr}$, oscillations in the regular field are established, with periods of $P_r \simeq 0.6\tau_{vr}$ for models 1 and 5 and $P_r \simeq 0.74\tau_{vr}$ for model 2. The period of the oscillations in ζ is $P_\zeta \simeq 0.6\tau_{vr}$, while the periods of the oscillations in ξ and η are $P_{\xi,\eta} \simeq P_\xi \simeq P_\eta \simeq 1.2\tau_{vr}$ in models 3 and 4 (in these models, the phases of the cluster oscillations are approximately the same in ξ and η, and the period of the cluster oscillations in the (ξ, η) plane is twice the period in ζ: this period doubling is especially conspicuous in model 3). If we adopt as the beginning of the period $P_{\xi,\eta}$ the time of the strongest contraction of the cluster along the ξ, η, and ζ coordinates, the middle of the period $P_{\xi,\eta}$ corresponds to the time when the cluster undergoes the strongest contraction in ζ and the strongest expansion in ξ and η, whereas, at the end of $P_{\xi,\eta}$, the cluster synchronously experiences its strongest contraction in ξ, η, ζ, etc. Figure 1 shows the time dependences of the virial coefficient $\alpha(t)$ for the stars with clustercentric distances $r \le R_t$ for models 1 and 3. All the open-cluster models exhibit a weak decrease of the amplitude of oscillations of α with time. The small, irregular perturbations in the $\alpha(t)$ curves at large t/τ_{vr} are probably due to errors accumulated during the computation of the stellar trajectories.

We determined the Jeans wavelength λ_J for models 1–5 using formula (15.42) from [14] and the technique described in [2]. The resulting λ_J estimates range from $\lambda_J = 2D$ (for model 1) to $\lambda_J = 2.6D$ (for model 5). Here, $D = 2R_t^-$ is the diameter of the cluster. According to [15], in this situation, small, random density fluctuations (due to stellar encounters) can easily excite large-scale density oscillations, since the systems considered are close to gravitational instability. This enhancement of small density oscillations should be more active in model 1 (this model is closer to gravitational instability than the other models, and has the lowest λ_J/D).

We will analyze fluxes of stars in spaces of the quantities $\varepsilon, l, \varepsilon_\zeta, \Gamma(\varepsilon), r, v, (r,v)$, and (r,ε) in cluster models 1–5. Formulas for ε, l, and ε_ζ can be found in [1]. Here, $\Gamma(\varepsilon)$ is the phase-space volume occupied by cluster stars with energies $\varepsilon' \le \varepsilon$. A description

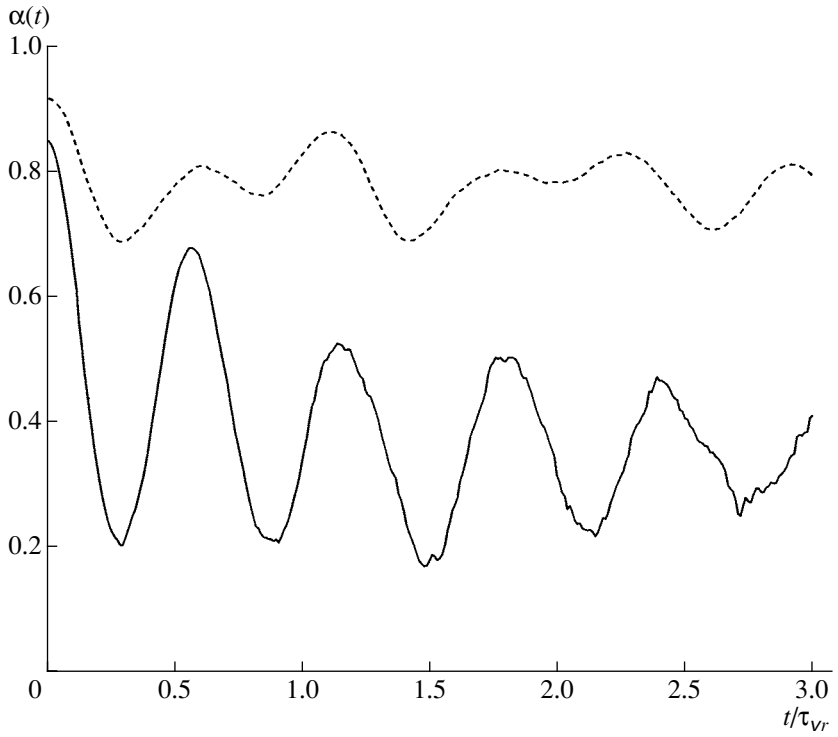

Fig. 1. Time dependences of $\alpha(t)$ in cluster models 1 (solid line) and 3 (dashed line).

of the technique used to compute $\Gamma(\varepsilon)$ can be found in [2]. We used formulas (3) and (7) to monitor the accuracy of the computations of the rates of stellar transitions in the various spaces.

In all the open-cluster models, for time intervals of the stellar transitions $\Delta t = 0.1\tau_{vr}$, the matrices describing the numbers of stellar transitions in spaces of ε, l, ε_ζ, $\Gamma(\varepsilon)$, and r are banded for all the t values considered (i.e., $n^{(x_k)}(i,j) = 0$ for $|i-j| > \Delta_k, i, j = 1, \ldots, 10$, where $k = 1, \ldots, 5$, $\mathbf{x} = (\varepsilon, l, \varepsilon_\zeta, \Gamma(\varepsilon), r)$). $\Delta_k = 1$ for $k = 1, 4$, $\Delta_2 = 2$, $\Delta_3 = 3$–5, and $\Delta_5 = 3$. The diagonal elements of the matrices $n^{(x_k)}(i,j)$ substantially exceed the other elements. The number of stellar transitions between well-separated intervals increases on long time intervals $\Delta t = (0.3$–$0.6)\tau_{vr}$. In all the open-cluster models, the rates of stellar transitions between intervals in the quantities x_k, $(k = 1, \ldots, 5)$ are balanced from the very beginning of the evolution until the end of the computations (the distributions $\nu^{(x_k)}(j)$ are quite symmetric about $j = 0$ at all times considered).

Figure 2 shows the distributions $\nu^{(y_m)}(j)$, and $m = 1, \ldots, 6$ for model 1 for $\mathbf{y} = (x_1, \ldots, x_5, v)$ and $\Delta t = 0.1\tau_{vr}$ (the corresponding distributions for other models are similar to these). The equilibrium distributions of the stars in $\varepsilon, l, \varepsilon_\zeta, \Gamma(\varepsilon)$, and r exist from the very beginning of their evolution. According to [2], the equilibrium distribution of stars in ε corresponds to the equilibrium PSDF $F_0(\mathbf{r}, \mathbf{v})$. This form of the equilibrium in the phase space is due to the balance of stellar fluxes in $\Gamma(\varepsilon)$, which is a result of the balance of fluxes in ε. Figure 2 shows that the stellar transitions are not balanced in v. The distributions of stars in r and v are related via the equilibrium PSDF. The equilibrium distribution of stars in r over the period P_r evolves such that the numbers of stars in the intervals $L_i(t)$ are approximately conserved, in spite of the periodic variations of the sizes of Δr_i. There is no such equilibrium in v space. The transitions of stars in (r, v) space are not balanced, since the cluster is not in virial equilibrium.

The origins of the equilibrium distribution $F_0(\mathbf{r}, \mathbf{v})$ in the open-cluster models at small t have nothing to do with the magnitude of the initial deviations of the cluster models from virial equilibrium, since these models have very different degrees of nonstationarity in the regular field, and there is a balance of stellar transitions in $\Gamma(\varepsilon)$ throughout their evolution (including at small t). The phase-space equilibrium corresponding to $F_0(\mathbf{r}, \mathbf{v})$ is likewise not due to our use of the initial relation $R_1/R_2 \sim (N_1/N_2)^{0.35}$ in the cluster models (since model 5 does not satisfy this relation at $t = 0$), or our use of the initial relation (1) (since model 4 does not obey this relation at $t = 0$). Note that ε, l, and ε_ζ, with the properties indicated in [1], appear as arguments of the equilibrium distribution function $f(\varepsilon, l, \varepsilon_\zeta)$ in [1] due to the condition

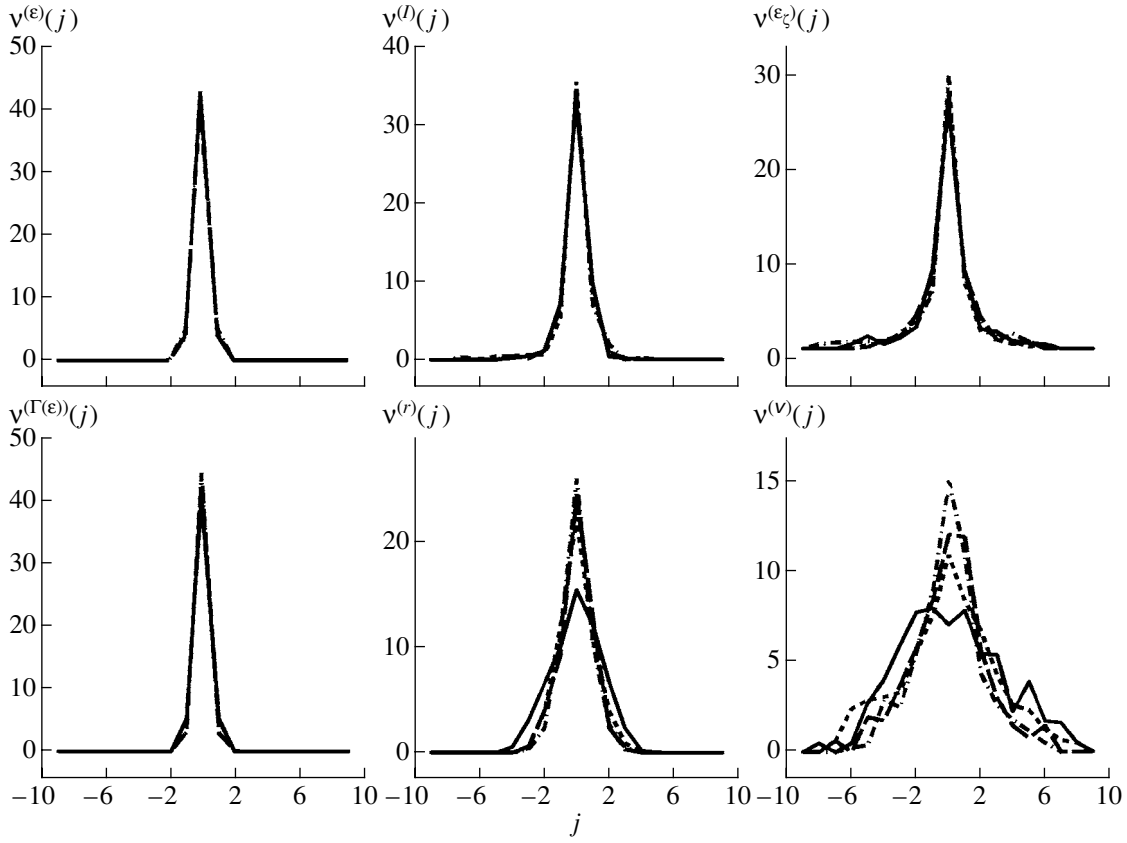

Fig. 2. Distributions of the number of stellar transitions in ε, l, ε_ζ, $\Gamma(\varepsilon)$, r, and v for cluster model 1 during the time $t_2 - t_1 = 0.1\tau_{vr}$ at various times ($t_1/\tau_{vr} = 0$, 1.0, 1.5, 2.1).

of maximum entropy of the system, as a consequence of the conservation of the integrals of the "energy" E from [7], angular momentum of the cluster A_ζ[7, (5.530)], and the energy E_ζ of the motion of the cluster stars in the ζ direction in the Galaxy. The conservation of A_ζ and E_ζ in the open-cluster models is due to the existence of various symmetries in the distributions of the stars in ξ, η, ζ. These symmetries, in turn, are due to the axial symmetry of the potential adopted for the regular forces in the Galaxy and the motion of the open-cluster models in circular orbits in the Galactic plane. The phase-space equilibrium corresponding to $F_0(\mathbf{r}, \mathbf{v})$ at small t is probably also a result of these same factors.

The quantities $\psi^{(z_i)}$ and the dispersions σ_{z_i} of j for stellar transitions in the spaces z_i, $i = 1, 2, 3$, $\mathbf{z} = (\varepsilon, l, \varepsilon_\zeta)$ remain small (and vary little) from $t = 0$ until the end of the computations (for model 1, see Fig. 3). This also indicates that the equilibrium distributions of stars $f(\varepsilon, l, \varepsilon_\zeta)$ and $F_0(\mathbf{r}, \mathbf{v})$ exist in all the open-cluster models from the very beginning of their evolution. Thus, in these cluster models, violent relaxation proceeds under the conditions of the equilibrium distribution $F_0(\mathbf{r}, \mathbf{v})$. Therefore, t_r is not the time for the relaxation of the open-cluster models to the phase-space equilibrium described by the function $F_0(\mathbf{r}, \mathbf{v})$. This relaxation leads to the spontaneous establishment of a single frequency of synchronous oscillations in models 1, 2, and 5, and the development of oscillations with two characteristic frequencies and the corresponding amplitudes of the large-scale oscillations in models 3 and 4. The parameters of the established ("equilibrium") oscillation process in models 1–5 vary little with time (see Fig. 1 for models 1 and 3). Thus, it would be more correct to refer to t_r in models 1–5 as the time for the establishment of an "equilibrium" oscillatory process that is close to an autowave process [16, 2].

According to Fig. 2, the number of intervals $\Delta\varepsilon$ that a star passes through in model 1 in the direction of increasing (decreasing) ε is, on average, $v_\varepsilon = 0.5\sigma_\varepsilon/\Delta t$. The greater v_ε, the faster the motion of the stars and the relaxation of the system in ε space. Because the size of the cluster in ε space is equal to ten intervals $\Delta\varepsilon$ [see discussion of (2)], the relaxation time of the cluster in ε space is $\tau_\varepsilon = 10/v_\varepsilon = 2\tau_{vr}/\sigma_\varepsilon$ (here, we use the fact that $\Delta t = 0.1\tau_{vr}$). Thus, τ_ε is the mean time it takes a star to change its energy ε by an amount on the order of the size of the cluster in ε

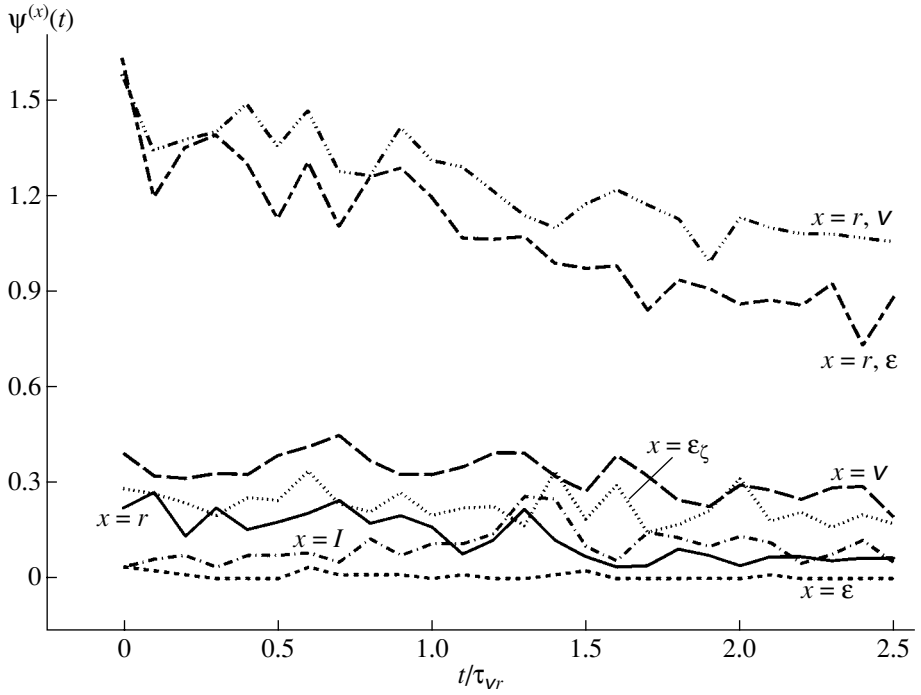

Fig. 3. Time dependences of $\psi^{(x)}(t)$ for cluster model 1.

space under the action of all forces and mechanisms operating in the cluster. We can similarly determine the cluster relaxation times τ_l and τ_{ε_ζ} in the spaces of l and ε_ζ.

Columns 9–12 of the table give estimates of τ_ε, τ_l, τ_{ε_ζ} (all in fractions of τ_{vr}), and σ_v/σ_r in models 1–5 taking into account the mean σ_ε, σ_l, $\sigma_{\varepsilon_\zeta}$, σ_v, and σ_r values over the evolution time intervals considered for these models. The errors in τ_ε, τ_l, and τ_{ε_ζ} due to the dispersions of the corresponding mean quantities $\nu(j)$ from (4) in models 1–5 are 1.5–4% of τ_ε, τ_l, and τ_{ε_ζ} (the dispersions of $\nu(j)$ in (4) are usually three to four orders of magnitude smaller than those of j obtained taking into account the distributions $\nu(j)$). Column 8 of the table gives estimates of the local violent-relaxation time $t_{r,h}$ in the phase space for the cluster halo (in fractions of τ_{vr}) obtained in [1, 2] for cluster model 1 and in [11] for models 2 and 3). We can see that $\tau_\varepsilon > t_{r,h} > \tau_{\varepsilon_\zeta}$ in models 1–3. In all the models except for model 3, $\tau_\varepsilon > \tau_l > \tau_{\varepsilon_\zeta}$. In model 3, $\tau_l > \tau_\varepsilon > \tau_{\varepsilon_\zeta}$. Note that clusters with parameters for their core–halo structure close to the initial parameters of model 3 are rarely found among observed open clusters (see the (ξ, μ) diagram for 103 open clusters in [6]). Therefore, the inequalities $\tau_\varepsilon > \tau_l > \tau_{\varepsilon_\zeta}$ obtained for models 1, 2, and 4 are more characteristic of observed open clusters. Thus, the fastest violent relaxation in these cluster models is found in the space of ε_ζ. The rate of violent relaxation in the phase space, $\sim 1/t_{r,h}$, is somewhat lower in models 1–3 than $1/\tau_{\varepsilon_\zeta}$. The small values of τ_{ε_ζ} in models 1–5 are probably due to the fact that they contract mainly along the ζ axis, and their subsequent oscillations along this axis also have higher amplitudes (in models 1, 2, and 5) and frequencies (in models 3 and 4) than the oscillations along the ξ and η axes. Lower values of τ_ε are achieved in denser cluster models with a lower degree of nonstationarity in the regular field. The quantities τ_{ε_ζ} exhibit the same, albeit less prominent, dependence. The largest τ_l values are typical of cluster models with intermediate mean densities. The table shows that the difference between the largest (τ_ε or τ_l) and smallest (τ_{ε_ζ}) relaxation times decreases with decreasing nonstationarity of the open-cluster models.

The open-cluster models considered here may develop phase-space barriers [4; 17, p. 155], through which the diffusion of stars is slow, which has various effects on the rates of change of ε, l, and ε_ζ for these stars. The number of stochastic stellar trajectories and their influence probably grow in denser cluster models with lower degrees of nonstationarity in the regular field, decreasing the role of phase barriers and leading to their disappearance in such systems [17]. In this case, the differences between the relaxation times for open-cluster models in the spaces of ε, l, and ε_ζ, which increase with increasing nonstationarity of the cluster models, can also be considered to reflect self-organization of such systems.

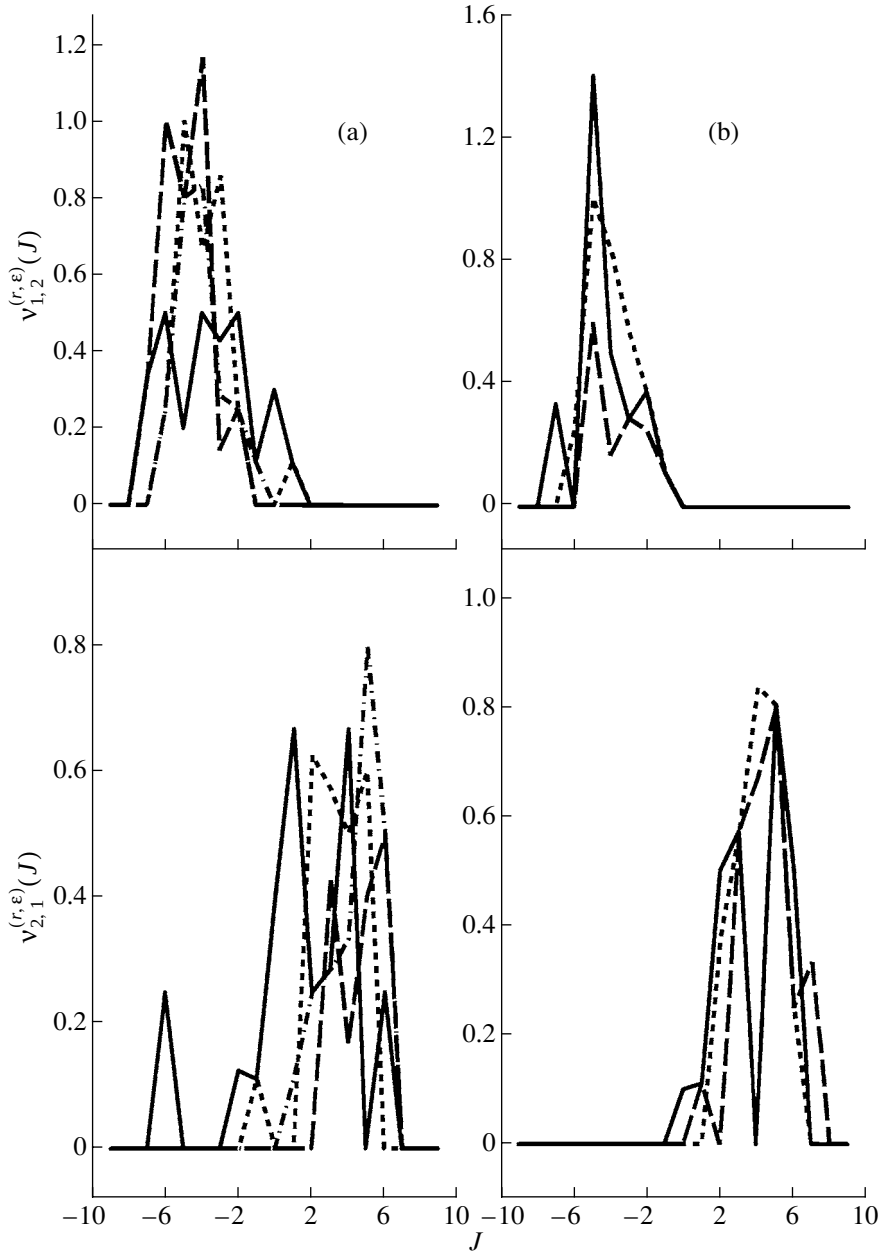

Fig. 4. Distribution of the number of stellar transitions in (r, ε) space in cluster model 1 during time interval $t_2 - t_1 = 0.1\tau_{vr}$ for (a) various times ($t_1/\tau_{vr} = 0.1$, 0.7, 1.3, 1.9) during the stage of contraction of the cluster and (b) for various times ($t_1/\tau_{vr} = 0.3$,1.0, 1.5) during the stage of expansion.

The table shows that $\sigma_v/\sigma_r > 1$ in the cluster models considered, and the value of σ_v/σ_r averaged over models 1–5 is $\langle\sigma_v/\sigma_r\rangle \simeq 2.1$, with the maximum and minimum values being $\sigma_v/\sigma_r = 2.8$ and $\sigma_v/\sigma_r = 1.3$, respectively. Thus, in models 1–5, the rate of cluster relaxation is, on average, a factor of 2.1 higher in v space than in r space. This is due to the broader "wings" of the distributions $\nu^{(v)}(j)$ compared to those of $\nu^{(r)}(j)$.

The quantities $\psi^{(r,v)}$ and $\psi^{(r,\varepsilon)}$ exceed the quantities $\psi^{(r)}$, $\psi^{(v)}$ by a factor of a few and slowly decrease with time for all models considered (see Fig. 3 for the case of model 1). This indicates that the fluxes of stars in the spaces (r, v), (r, ε) are not balanced and that the models undergo slow evolution toward the establishment of balances of the stellar fluxes in these two spaces. The lack of balance of the fluxes of stars in (r, v) space is due to the cluster energy being transferred from kinetic to potential and back

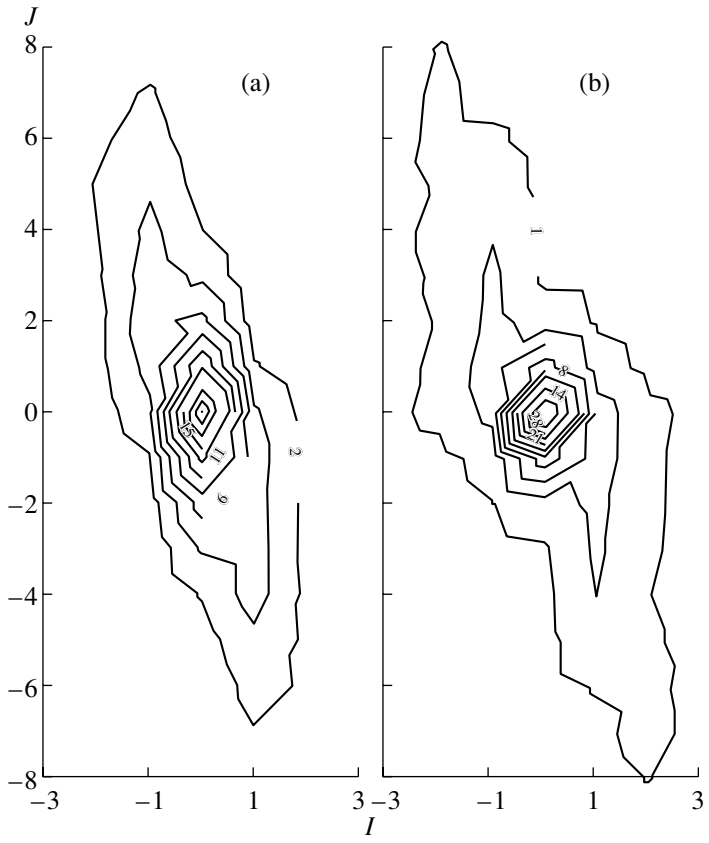

Fig. 5. (I, J) diagrams of "synthetic" distributions of the numbers of stellar transitions in the spaces (a) (r, v) and (b) (r, ε) during the time $\Delta t = 0.1\tau_{vr}$ in cluster model 1.

to kinetic energy (because the cluster models are not in virial equilibrium). Figure 4 shows the distributions $\nu_{1,2}^{(r,\varepsilon)}(J)$ and $\nu_{2,1}^{(r,\varepsilon)}(J)$ for several times in the evolution of model 1 during periods of cluster expansion and contraction. We can easily see that these distributions are antisymmetric about $J = 0$. The asymmetry of these distributions increases for stellar transitions in r by a greater number of intervals. The distributions $\nu_{1,2}^{(r,\varepsilon)}(J)$ and $\nu_{2,1}^{(r,\varepsilon)}(J)$ become symmetric about $J = 0$ only near the times of maximum contraction or expansion of the cluster, when the regular force field of the cluster does not change. These distributions are also nearly symmetric about $J = 0$, independent of t for fluxes of stars in ε space accompanied by transitions of these stars in r at the cluster periphery (between L_7 and L_{10}). Thus, as the regular field of the cluster changes over a period P_r, the stars moving along r toward the cluster center increase their energies ε, while those moving away from the center decrease their energies. This effect disappears near times of maximum contraction and expansion of the cluster. Because the distribution $\nu^{(r)}(j)$ is always symmetric about $j = 0$ in the open-cluster models, for each star moving along r toward the cluster center, there is a star moving away from the center. This leads to the development of a flux of stellar energy ε directed toward the center of the cluster. This flux is due to the "heating" of the cluster by the time-dependent regular force field of the cluster. The energies ε of stars in the cluster core are, on average, lower than the stellar energies at the periphery (the fraction of halo stars is usually small in the cluster core). The orbits of halo stars are usually larger than the orbits of stars of the cluster core. The flux of energy toward the cluster center considered here is therefore a manifestation of energy transfer from large-scale motions to small-scale motions and also a manifestation of self-organization of such systems.

Figures 5a and 5b show families of equal-density contours for the "synthetic" distributions $\nu^{(r,v)}(I, J)$ and $\nu^{(r,\varepsilon)}(I, J)$ obtained for model 1 using (8). The distributions $\nu^{(r,v)}(I, J)$ and $\nu^{(r,\varepsilon)}(I, J)$ obtained for individual pairs of times t and $t + \Delta t$ agree well with the corresponding synthetic distributions; however, the contours of the synthetic distributions are less distorted by random fluctuations of these distributions (i.e., they are smoother). The directions of the

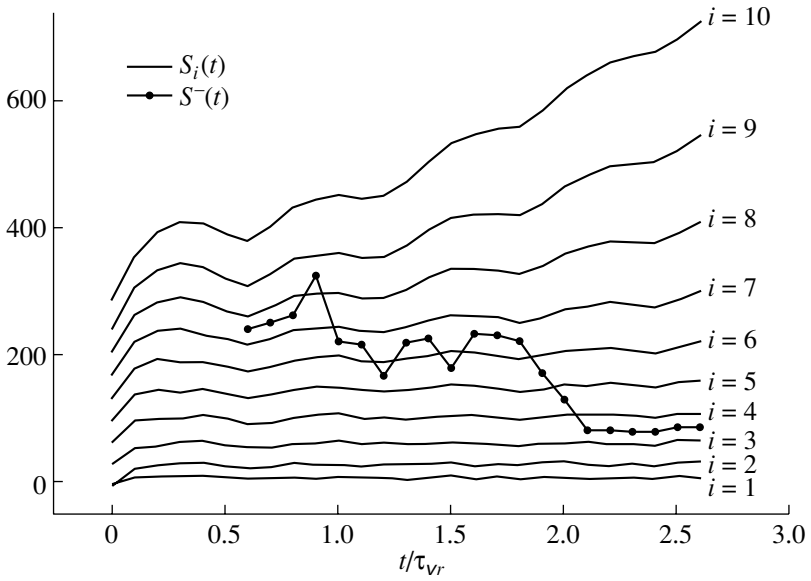

Fig. 6. Time dependences of $S_i(t)$ and $S^-(t)$ in cluster model 1.

largest extent of the distributions $\nu^{(r,v)}(I,J)$ and $\nu^{(r,\varepsilon)}(I,J)$ in the (I,J) plane do not coincide with the I and J axes. For fluxes of stars in (r,v) space, this is due to the increase of a star's velocity in the regular field when it moves toward the cluster center (and to the decrease of a star's velocity as it moves away from the cluster center). The degree of extension of the distribution $\nu^{(r,v)}(I,J)$ along the indicated direction in (I,J) space is also due to the lack of a virial equilibrium in the system (synchronous radial motions of stars dominate).

For fluxes of stars in (r,ε) space, the slope of the direction of maximum extension of the distribution $\nu^{(r,\varepsilon)}(I,J)$ with respect to the I and J axes is due to "heating" of the cluster by the periodically varying regular force field of the cluster [the energies ε of stars moving toward the cluster center ($I<0$) increase and those moving away from the cluster center ($I>0$) decrease]. Judging from the ticks indicating the numbers of stars in the fluxes on the contours showing the relation $r=r(\varepsilon)$ in Fig. 5b, a net energy flux toward the cluster center is ensured by the somewhat smaller number of stellar transitions in (r,ε) space compared to the number of transitions producing the similar dependence $r=r(v)$ in (r,v) space. The relaxation of the stellar motions is fastest in the direction of the maximum extension of the distributions $\nu^{(r,v)}(I,J)$ and $\nu^{(r,\varepsilon)}(I,J)$ in the (I,J) plane (and in the corresponding (r,v) and (r,ε) planes) and is slowest perpendicular to these directions for the (r,v) and (r,ε) planes. Although the flux of energy ε from large-scale to small-scale stellar motions is relatively small, it is sufficient to bring about self-organization of the system and to synchronize all density oscillations on various scales developing in the cluster (Fig. 1). The energy coming into the cluster phase-space element $\Delta\Gamma$ due to this flux is apparently redistributed in the cluster via the diffusion of stars in the phase space due to stellar encounters. This redistribution of the stellar energies should result in a gradual decay of the large-scale oscillations in the cluster, as we can see in the time dependences of the virial coefficient $\alpha=\alpha(t)$ for cluster models 1 and 3 in Fig. 1.

Figure 6 shows the plots of the dependences $S_k(t)=\sum_{i=1}^{k}\sum_{j=1}^{10}\ln Q_{ij}$ for model 1. The quantities $S_k(t)$ show how the entropy of the system of cluster stars with clustercentric distances $r\le r_{50\times k}$ varies with time (the r_i increase with i). The broken line with dots in Fig. 6 shows the dependence $S^-(t)$, where $S^-(t)$ is the entropy of the system of stars with clustercentric distances $r\le R_t^-$ at time t. Here, we determined $S^-(t)$ approximately using the formula $S^-(t)=\frac{1}{2}(S_{k-1}(t)+S_k(t))$ if $R_t^-\in L_k(t)$. The errors of the $S^-(t)$ values determined in this way do not exceed $\sim(0.56\text{–}0.71)\Delta S_k(t)$, where $\Delta S_k(t)=S_k(t)-S_{k-1}(t)$. The errors in R_t^- at $t\ge\tau_{vr}$ do not exceed $\sim(0.25\text{–}0.5)\Delta r_k$. The R_t^- values in model 1 could be determined only at $t\ge0.6\tau_{vr}$ (due to specific features of the technique used to estimate R_t^- [10]). The entropy $S=S_{10}(t)$ increases during the evolution of model 1 (due to the increase of the phase-space volume occupied by the cluster stars), and this dependence is superimposed by the oscillations of S with the period P_r. The maximum S values are attained approximately at the times of

maximum contraction of the cluster in the radius r (due to the increase of the size of the cluster in the v space). The production of entropy in such systems usually increases or decreases when the mean density increases or decreases. The quantities $\Delta S_i(t)$ also exhibit systematic increases and periodic oscillations, which are most important at the cluster periphery. The increase of $\Delta S_{10}(t)$ with time is due to the fact that stars with cluster-centric distances $r \in L_{10}(t)$ at $t > (0.4 - 0.5) \cdot \tau_{vr}$ satisfy the condition $r > R_t^-$. These stars gradually leave the cluster, and their velocities are increased in the Galactic force field. According to Fig. 6, $S^-(t)$ also undergoes (apparently random) variations and slight decreases at $t > 0.9\tau_{vr}$ due to the decrease in the number of stars with $r \le R_t^-$.

The periodic variations of the entropy S with time are due to the lack of virial equilibrium in the system and the fact that the fluxes of stars in (r, v) space are not balanced. The decrease in the entropy S over a time $\Delta t = \frac{1}{2}P_r$ after the maximum contractions of the clusters is a sign of self-organization of such systems and is due to the synchronization of the radial motions of the stars under the action of the regular force field during the preceding contraction of the cluster. A more detailed study of the manifestations of self-organization in open-cluster models requires analysis of the stellar trajectories in such systems.

5. CONCLUSIONS

(1) The open-cluster models considered here display a balance of the fluxes of stars in the spaces of ε, l, ε_ζ, $\Gamma(\varepsilon)$, and r from the beginning of the evolution until the end of the computations. Therefore, equilibrium distributions of the stars in these spaces are present throughout the dynamical evolution of these models. The equilibrium distribution of stars in r space during periodic oscillations of the regular field of the cluster evolves such that the numbers of stars in the intervals $L_i(t)$ are approximately conserved, despite the periodic variations of the sizes Δr_i. The equilibrium PSDF $F_0(\mathbf{r}, \mathbf{v})$ corresponding to a balance of the fluxes of stars in the spaces $\Gamma(\varepsilon)$ and ε is present from the beginning of the evolution of the open-cluster models. In these models, violent relaxation proceeds under the conditions of this equilibrium distribution $F_0(\mathbf{r}, \mathbf{v})$, and results in the development of an "equilibrium" oscillatory process over a time t_r, whose parameters vary little with time. Violent relaxation in these models is a form of self-organization, and t_r is the time for self-organization of the cluster to a level close to an auto-wave process.

(2) The presence of the equilibrium distribution $F_0(\mathbf{r}, \mathbf{v})$ in the open-cluster models from the beginning of their evolution until the end of the computations is most likely due to the axial symmetry of the adopted model for the Galactic potential, the circular orbits of the open-cluster models in the Galactic plane, and symmetries in the distributions of stars in the models.

(3) In these open-cluster models, the fluxes of stars in the spaces of v, (r, v), and (r, ε) remain unbalanced throughout their evolution. The cluster models exhibit a slow evolution toward the establishment of balances of the stellar fluxes in these spaces. The lack of an equilibrium in the v and (r, v) spaces is due to the lack of a virial equilibrium in the open-cluster models.

(4) During the variations of the regular field of the cluster over the period of its oscillations, stars moving in the r direction toward the cluster center increase their energy ε, while those moving away from the center decrease their energy. This effect is most important in the central regions of the cluster, decreases at the periphery, and is absent near the times of maximum contraction and expansion of the cluster. During the variations of the regular field of the cluster over the period of its oscillations, an energy flux develops toward the center of the cluster (due to the "heating" of the cluster by its variable regular field), and energy ε is transferred from large-scale to small-scale stellar motions. This energy flux leads to self-organization of the cluster models. The clearest manifestation of this self-organization is the spontaneous establishment of an "equilibrium" oscillatory process.

(5) We estimated the relaxation times of the open-cluster models in the spaces of ε, l, and ε_ζ. The relaxation of the cluster models is fastest in ε_ζ space. The relaxation times most often satisfy the inequalities $\tau_\varepsilon > \tau_l > \tau_{\varepsilon_\zeta}$. The difference between the maximum and minimum relaxation times in the spaces of ε, l, and ε_ζ increases with increasing nonstationarity of the open-cluster models. On average, the relaxation in v space proceeds a factor of 2.1 faster than in r space.

(6) We found anisotropy in the fluxes of stars in the (r, v) and (r, ε) spaces. The direction and degree of the extension of the distribution of stellar fluxes in (r, v) space are due to the lack of a virial equilibrium in the open-cluster models and the acceleration of stars by the force field of the cluster. The direction and degree of extension of the distribution of stellar fluxes in (r, ε) space are due to the flux of stellar energies ε directed along the radius r toward the cluster center.

(7) The entropy S of the cluster models increases systematically with time, with the periodic oscillations of the density and regular field of the cluster

superimposed on this increase. The entropy oscillations are in antiphase with the oscillations of the radial (r) sizes of the clusters. The entropy $S^-(t)$ of the system of stars in cluster model 1 with clustercentric distances $r \leq R_t^-$ decreases during the evolution at $t > 0.9\tau_{vr}$, due to the decrease in the number of such stars in the cluster.

6. ACKNOWLEDGMENTS

This work was supported by the Russian Foundation for Basic Research, project no. 00-02-16217.

REFERENCES

1. V. M. Danilov, Astron. Zh. **77**, 345 (2000) [Astron. Rep. **44**, 298 (2000)].
2. V. M. Danilov, Astron. Zh. **79**, 492 (2002) [Astron. Rep. **46**, 443 (2002)].
3. D. Lynden-Bell, Mon. Not. R. Astron. Soc. **136**, 101 (1967).
4. A. A. El-Zant, Astron. Astrophys. **326**, 113 (1997).
5. V. M. Danilov, Astron. Zh. **76**, 93 (1999) [Astron. Rep. **43**, 74 (1999)].
6. V. M. Danilov and A. F. Seleznev, Astron. Astrophys. Trans. **6**, 85 (1994).
7. S. Chandrasekar, *Principles of Stellar Dynamics* (Univ. of Chicago Press, Chicago, 1942; Inostrannaya Literatura, Moscow, 1948).
8. S. A. Kutuzov and L. P. Osipkov, Astron. Zh. **57**, 28 (1980) [Sov. Astron. **24**, 17 (1980)].
9. V. M. Danilov, Astron. Zh. **65**, 716 (1988) [Sov. Astron. **32**, 374 (1988)].
10. V. M. Danilov, Astron. Zh. **74**, 188 (1997) [Astron. Rep. **41**, 163 (1997)].
11. V. M. Danilov and L. V. Doragavtseva, Astron. Zh. **79**, 242 (2002).
12. V. M. Danilov, Pis'ma Astron. Zh. **23**, 365 (1997) [Astron. Lett. **23**, 322 (1997)].
13. I. R. King, Astrophys. J. **67**, 471 (1962).
14. W. C. Saslaw, *Gravitational Physics of Stellar and Galactic Systems* (Cambridge Univ. Press, Cambridge, 1985; Mir, Moscow, 1989).
15. M. D. Weinberg, Astrophys. J. **410**, 543 (1993).
16. V. A. Vasil'ev, Yu. N. Romanovskiĭ, and V. G. Yakhno, *Autowave Processes* [in Russian] (Nauka, Moscow, 1987).
17. R. Z. Sagdeev, D. A. Usikov, and G. M. Zaslavsky, *Nonlinear Physics: from the Pendulum to Turbulence and Chaos* (Nauka, Moscow, 1988; Harwood, Chur, 1988).

Translated by A. Dambis

Astronomy Reports, Vol. 46, No. 11, 2002, pp. 900–907. Translated from Astronomicheskiĭ Zhurnal, Vol. 79, No. 11, 2002, pp. 999–1007.

Analysis of Brightness Variations in the Massive Close Binary System UU Cassiopeia

T. S. Polushina

Astronomical Observatory, Ural State University, pr. Lenina 51, Yekaterinburg, 620083 Russia

Received April 30, 2001; in final form, May 23, 2002

Abstract—We derive the parameters of the hot, massive close binary system UU Cas from earlier and recent photoelectric $UBVR$ observations: $M_1 = 34.5M_\odot$, $M_2 = 25.7M_\odot$, $A = 69R_\odot$, and $i = 68°$; the components' limb darkening coefficients are close to 1. Our fitting of the light curves provides evidence for a high degree of over-contact: the components fill their inner critical surfaces by 132% and 100%. It is possible that the appearance of the light curve is determined not only by the distorted shapes of the components and their eclipses but, to a considerable extent, by screening by a complex envelope and the envelope's contribution to the system's total luminosity. © *2002 MAIK "Nauka/Interperiodica".*

1. INTRODUCTION

Four-color photoelectric observations of the eclipsing variable star UU Cas were carried out in 1984–1989 in the framework of studies of massive close binary systems at the Astronomical Observatory of Ural State University. Before this observing program, there was no photoelectric photometry for this star in the literature. Published photographic light curves have appeared fairly regularly and are relatively numerous; we know of ten such publications. It is striking that no two of these light curves are very similar. There are differences in the heights of the maxima, and the variations in the depths of the primary and secondary minima are extremely large. The variations in the secondary minimum are especially strong (Table 1). Differences of 0.3^m (with the maximum depth of the secondary minimum being II0.42^m) are difficult to attribute to uncertainties in the photographic photometry. Spectroscopic observations of the star are very sparse. Only one radial-velocity curve has been published, in 1934 [11], and the most recent estimates of its spectral type, B0.5III, were made in 1972 [12].

2. OBSERVATIONS

Our observations of UU Cas (BD+60°2629, $m_{\max} = 10.4^m(p)$, $m_{\min} = 10.8^m(p)$, $P = 8.51929^d$, Sp = B0.5III) were obtained with the single-channel photometer of the 45-cm telescope of Ural State University in four bands close to the standard $UBVR$ photometric bands. We acquired 190 differential measurements of the star's brightness in each of the filters, with good phase coverage of the variability period ($\sigma_U = \pm 0.028^m$, $\sigma_B = \pm 0.020^m$, $\sigma_V = \pm 0.018^m$, $\sigma_R = \pm 0.016^m$) [10]. The normal light curves of UU Cas are presented in Table 2, which contains the phases of the period and the corresponding brightness differences between the variable and comparison star together with their errors. The light curves are displayed in Fig. 1.

Antokhina and Kumsiashvili [9] present mean photoelectric UBV light curves for UU Cas obtained in 1975–1984. A comparison of the star's variability in two adjacent time intervals based on high-accuracy observing material confirms variability in the heights of the maximum and the depths of the minima, as well as a brightness excess on the ascending branches of the secondary minimum. However, the earlier of the two light curves shows distortions of the primary minimum in all bands, as well as deformations in the maximum of the order of 0.04^m (Fig. 1).

It is interesting that, in the presence of such large variations in the shape of the light curve over long time intervals, with the amplitudes of these variations being comparable to the variability amplitude ($\Delta m = 0.45^m$ in V), no significant variations in the period of the variations have been detected over the 90 years the system has been studied [10].

3. FITTING OF THE LIGHT CURVES

We used our own light curve to determine the physical and geometrical characteristics of the system. We computed the system's relative orbital elements in a Russell–Merrill model (homothetic triaxial ellipsoids) using the code of Lavrov [13] and applying a rectification procedure. Since there was no solution for this light curve, we constructed a

1063-7729/02/4611-0900$22.00

Table 1. Variations in the light curve of UU Cas

Authors	Years	N	Method	Δ Max	Min I	Min II	Comments	References
M. Beyer	1932–1935	120	pg	0.00^m	0.22^m	0.16^m	The amplitude varied during the observations	[1]
S.M. Selivanov	1934	63	vis					[2]
P.P. Parenago, B.V. Kukarkin	1896–1939	396	pg–vis	0.00	0.35	0.20		[3]
G. Tolmar	1934–1939	118	pg	0.00	0.44	0.42	Very large scatter	[4]
S. Gaposchkin		1334	pg–vis	0.02	0.40	0.26		[5]
W. Zonn	1955–1957	130	pg					[6]
J. Semeniuk, G. Romano	1942	163	pg	0.00	0.3	0.2		[7]
K. Haussler	1941–1967	499	pg	0.05	0.39	0.11		[8]
M.I. Kumsiashvili	1975–1984	850	pe U	0.01	0.45	0.32		[9]
			B	0.02	0.43	0.31		
			V	0.00	0.44	0.32		
T.S. Polushina	1984–1989	190	pe U	0.00	0.48	0.32		[10]
			B	0.01	0.43	0.33		
			V	0.03	0.45	0.35		
			R	0.02	0.45	0.35		

sort of "smoothed light curve" taking into account all available photoelectric observations with corresponding weights and introducing several assumptions following from the geometry of the model: the minima should be symmetrical, there should be no depressions in the branches of the minima, and the maxima should be smooth. Each point of the light curve constructed in this manner was assigned a weight. The results of our fitting of this light curve are displayed in Fig. 2 and presented in Table 3, where k is the ratio of the mean radii of the components, R_2 is the relative radius of the secondary, i is the orbital inclination, X is the limb-darkening coefficient, L_1 is the relative luminosity of the secondary, and ε is the eccentricity of the meridional section of the components, derived from the geometrical ellipticity factor.

We derived the absolute parameters of the system applying the method described by Svechnikov [14] and the empirical mass–luminosity relation for the main-sequence components of close binary systems [15], since only lines of the primary are visible in the spectra, and the component mass ratio cannot be determined directly from spectroscopic observations. We specified the mass of the primary using the mass-function value $f(m) = 3.693M_\odot$ derived by Sanford [11] from observations of the radial-velocity curve:

$$A(R_\odot) = 68.97 \pm 0.70, \quad q = 0.75 \pm 0.3,$$
$$R_1(R_\odot) = 38.5 \pm 3.1, \quad R_2(R_\odot) = 24.0 \pm 3.7,$$
$$M_1(M_\odot) = 34.5 \pm 1.5, \quad M_2(M_\odot) = 25.7 \pm 0.6.$$

The rms errors given here indicate the level of band-to-band deviations for the photoelectric light curves used.

The formal fitting solution for the smoothed light curves of UU Cas gave the following results.

(1) The system was found to be in an over-contact configuration, with the primary overfilling its inner critical surface (ICS) by, on average, 32%, reaching a surface containing the second Lagrangian point, and the secondary filling or nearly filling its inner critical surface. The apparent size of the secondary depends appreciably on the wavelength: while the secondary overfills its inner critical surface by 10% in the U band, its size in the V band corresponds to 84% of

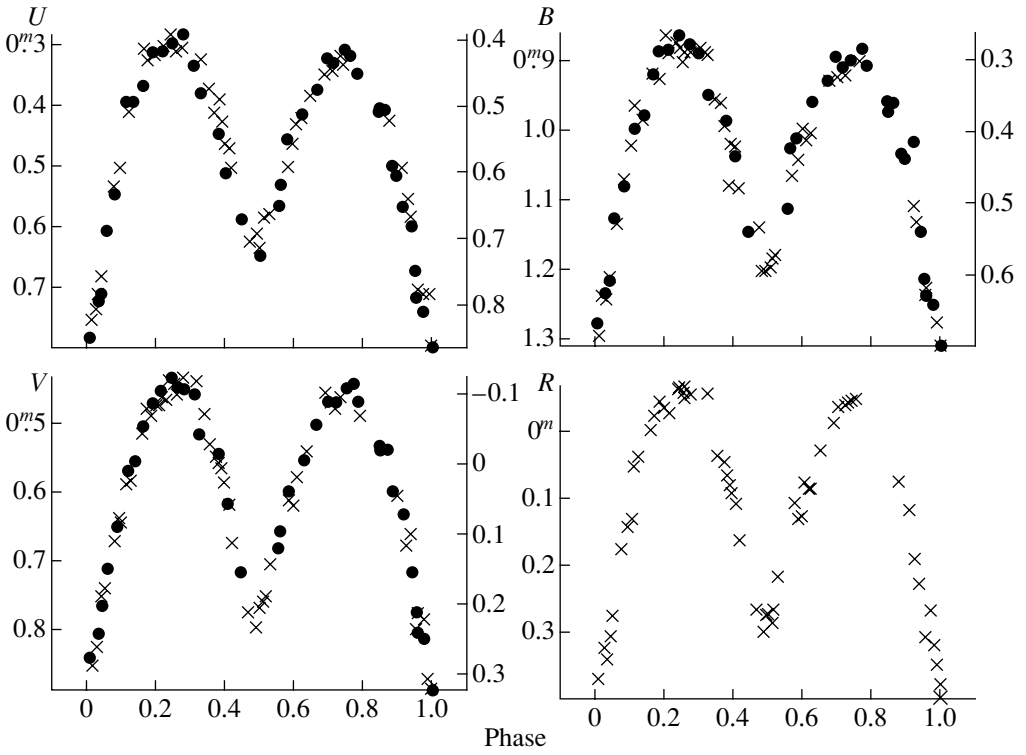

Fig. 1. Comparison of light curves of UU Cas for 1975–1984 (circles) and 1984–1989 (crosses).

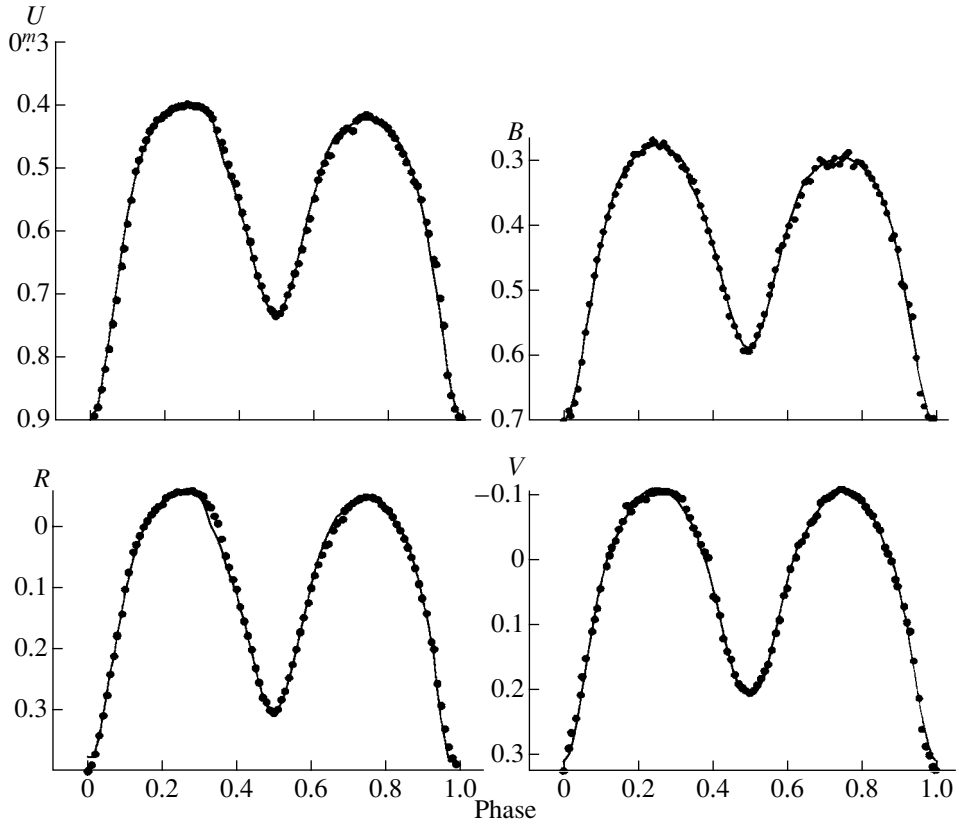

Fig. 2. Comparison of the theoretical light curves (solid curves) and observations (circles).

Table 2. Normal light curve of UU Cas

F_R	R	σ_R	F_V	V	σ_V	F_B	B	σ_B	F_U	U	σ_U
0.0140	$0^m.371$	$\pm 0^m.009$	0.0146	$0^m.852$	$\pm 0^m.009$	0.0147	$1^m.297$	$\pm 0^m.010$	0.0141	$0^m.754$	$\pm 0^m.019$
0.0253	0.325	0.009	0.0307	0.828	0.009	0.0297	1.239	0.010	0.0253	0.736	0.019
0.0337	0.341	0.009	0.0401	0.753	0.013	0.0369	1.244	0.014	0.0353	0.715	0.014
0.0413	0.307	0.013	0.0501	0.742	0.013	0.0453	1.212	0.014	0.0482	0.683	0.019
0.0511	0.274	0.013	0.0775	0.673	0.013	0.0636	1.135	0.014	0.0788	0.533	0.020
0.0788	0.177	0.013	0.0911	0.638	0.013	0.0850	1.071	0.014	0.0949	0.503	0.014
0.0911	0.142	0.013	0.0972	0.643	0.013	0 0949	1.081	0.014	0.1126	0.435	0.014
0.1034	0.132	0.009	0.1115	0.589	0.009	0.1075	1.020	0.010	0.1222	0.407	0.020
0.1148	0.051	0.013	0.1209	0.583	0.013	0.1180	0.964	0.014	0.1615	0.305	0.019
0.1222	0.041	0.013	0.1560	0.515	0.013	0.1384	0.982	0.014	0.1790	0.325	0.019
0.1573	−0.001	0.013	0.1700	0.480	0.013	0.1633	0.919	0.014	0.1984	0.317	0.013
0.1707	−0.020	0.013	0.1817	0.489	0.013	0.1755	0.919	0.014	0.2199	0.302	0.013
0.1884	−0.043	0.009	0.1929	0.472	0.013	0.1875	0.923	0.014	0.2383	0.284	0.013
0.2015	−0.037	0.009	0.2009	0.471	0.009	0.1991	0.861	0.010	0.2499	0.300	0.013
0.2126	−0.029	0.013	0.2228	0.467	0.009	0.2155	0.889	0.010	0.2602	0.306	0.014
0.2353	−0.064	0.009	0.2368	0.438	0.009	0.2358	0.874	0.010	0.2748	0.304	0.014
0.2395	−0.067	0.009	0.2398	0.439	0.013	0.2394	0.876	0.014	0.3287	0.323	0.020
0.2505	−0.057	0.009	0.2507	0.443	0.009	0.2473	0.880	0.010	0.3533	0.374	0.011
0.2573	−0.066	0.009	0.2575	0.448	0.010	0.2566	0.902	0.012	0.3706	0.410	0.011
0.2601	−0.052	0.009	0.2602	0.458	0.010	0.2568	0.887	0.012	0.3813	0.392	0.014
0.2738	−0.054	0.009	0.2730	0.447	0.010	0.2696	0.881	0.012	0.3914	0.427	0.013
0.3243	−0.055	0.009	0.2792	0.433	0.013	0.2765	0.882	0.014	0.3976	0.462	0.019
0.3531	0.037	0.007	0.3188	0.438	0.013	0.3005	0.882	0.014	0.4086	0.469	0.020
0.3693	0.044	0.008	0.3356	0.485	0.018	0.3210	0.888	0.020	0.4193	0.504	0.019
0.3786	0.064	0.009	0.3523	0.531	0.007	0.3494	0.953	0.008	0.4718	0.626	0.014
0.3864	0.080	0.009	0.3697	0.550	0.007	0.3664	0.959	0.009	0.4893	0.613	0.014
0.3955	0.093	0.007	0.3789	0.557	0.008	0.3769	0.991	0.009	0.4989	0.637	0.013
0.4086	0.105	0.013	0.3894	0.568	0.009	0.3873	1.080	0.010	0.5138	0.584	0.013
0.4184	0.161	0.009	0.3955	0.587	0.009	0.3941	1.018	0.010	0.5304	0.580	0.020
0.4715	0.266	0.009	0.4107	0.619	0.010	0.4043	1.021	0.012	0.5820	0.501	0.019
0.4890	0.299	0.009	0.4190	0.673	0.010	0.4191	1.082	0.010	0.5914	0.463	0.014
0.4949	0.273	0.009	0.4702	0.777	0.008	0.4693	1.140	0.010	0.6035	0.429	0.013
0.5030	0.272	0.009	0.4888	0.796	0.008	0.4853	1.204	0.009	0.6135	0.421	0.013
0.5127	0.267	0.009	0.4988	0.769	0.008	0.4954	1.205	0.009	0.6468	0.382	0.020
0.5164	0.287	0.013	0.5111	0.761	0.009	0.5098	1.196	0.010	0.6875	0.347	0.013
0.5295	0.216	0.013	0.5156	0.753	0.010	0.5149	1.185	0.012	0.7063	0.343	0.014
0.5765	0.108	0.018	0.5296	0.705	0.013	0.5226	1.180	0.014	0.7162	0.325	0.014
0.5859	0.129	0.009	0.5825	0.612	0.009	0.5693	1.064	0.010	0.7279	0.316	0.014
0.5935	0.124	0.013	0.5918	0.619	0.010	0.5894	1.041	0.012	0.7417	0.332	0.014
0.6019	0.075	0.009	0.6015	0.577	0.009	0.5998	0.998	0.010	0.8713	0.424	0.014
0.6093	0.086	0.009	0.6088	0.578	0.009	0.6072	1.011	0.010	0.9046	0.504	0.020
0.6171	0.085	0.013	0.6312	0.541	0.009	0.6229	1.001	0.010	0.9241	0.554	0.013
0.6468	0.028	0.013	0.6855	0.455	0.008	0.6769	0.927	0.009	0.9376	0.583	0.020
0.6855	−0.012	0.008	0.7022	0.470	0.008	0.6948	0.920	0.009	0.9554	0.706	0.011
0.6980	−0.036	0.009	0.7152	0.478	0.009	0.7108	0.902	0.010	0.9737	0.713	0.019
0.7128	−0.044	0.008	0.7278	0.461	0.008	0.7230	0.916	0.009	0.9905	0.712	0.014
0.7229	−0.042	0.009	0.7873	0.489	0.008	0.7594	0.900	0.009	0.9980	0.799	0.014
0.7303	−0.046	0.009	0.8957	0.605	0.009	0.8832	1.031	0.010			
0.7448	−0.049	0.009	0.9222	0.675	0.009	0.9172	1.105	0.010			
0.8713	0.076	0.013	0.9322	0.661	0.009	0.9266	1.132	0.010			
0.8991	0.117	0.009	0.9520	0.802	0.009	0.9489	1.237	0.010			
0.9238	0.188	0.008	0.9596	0.776	0.013	0.9568	1.228	0.014			
0.9343	0.227	0.009	0.9729	0.785	0.009	0.9702	1.242	0.010			
0.9520	0.307	0.009	0.9896	0.874	0.009	0.9853	1.277	0.010			
0.9656	0.269	0.009	0.9969	0.887	0.009	0.9964	1.309	0.009			
0.9738	0.317	0.013									
0.9858	0.347	0.013									
0.9948	0.378	0.009									
0.9988	0.398	0.009									

Table 3. Photometric elements of the UU Cas system

	k	R_2	i	X	L_1	ε^2	R_1/ICS_1, %	R_2/ICS_2, %
U	0.730	0.382	66.6°	1	0.787	0.103	131	110
	±0.104	±0.035	±0.3		±0.081			
$B(1)$	0.770	0.403	64.1	1	0.747	0.110	132	114
	.049	.015	.3		.026			
$B(2)$	0.568	0.344	67.1	1	0.857	0.173	151	99
	.202	.060	.3		.109			
V	0.519	0.291	69.9	0.9	0.835	0.104	139	84
	.018	.007	.4		.091			
R	0.559	0.327	69.3	1	0.837	0.143	129	106
	.040	.010	.2		.024			

the inner critical surface. The size of the primary is in agreement in all the bands within the errors in the fitting.

(2) The limb-darkening coefficient X is very high, corresponding to the value expected for red giants. Using lower X values resulted in poorer convergence or the absence of a solution.

(3) The B light curve gave two solutions with equally good convergence, presented in Table 3 as $B(1)$ and $B(2)$.

(4) The derived inclination of the orbit to the plane of the sky is different for different bands, with the differences greatly exceeding 3σ.

4. VARIABILITY OF UU CAS NOT COVERED BY THE MODEL

In the next stage of our analysis, we plotted deviations of the observed light curves for each time interval from the obtained model light curves for the corresponding bands, based on the 95% confidence intervals. The (O−C) curves for 1975–1984 and 1984–1989 are presented in Figs. 3 and 4. We can see the following in these figures.

(1) The deviations from the theoretical curve reach large values at some phases of the period; for example, 0.1^m in the R band at phase 0.96 during 1984–1989 or 0.08^m in the B band at phase 0.56 in 1975–1984.

(2) These deviations are significant and considerably exceed 2σ.

(3) The deviations are repeated in different bands, especially in the 1975–1984 observations, and some persist in 1984–1989. (The degree of correlation between the curves is demonstrated by Tables 4–6, which contain the sample correlation coefficients and corresponding statistical parameters, t, which enable us to test the null hypothesis for a significance level $\alpha = 0.05$; t_{crit} can be used to judge the significance level of a correlation coefficient).

(4) Many features present in all bands and even for both seasons are visible only in very narrow phase intervals, $0.02–0.05^P$.

Table 4. Sample correlation coefficients between the deviation curves for the UBV observations of 1975–1984

	B	t_{Bi}	V	t_{vi}
U	0.638	5.106	0.654	5.331
B			0.799	8.185

Note: $t_{\mathrm{crit}} = 2.028$.

5. DISCUSSION

We interpreted these results using the results of the computations of a model binary system consisting of two ellipsoidal components embedded in a semi-transparent common envelope carried out by Pustyl'nik and Einasto [16, 17]. These studies simultaneously took into account the main effects of interaction in the close binary system and of eclipses, as

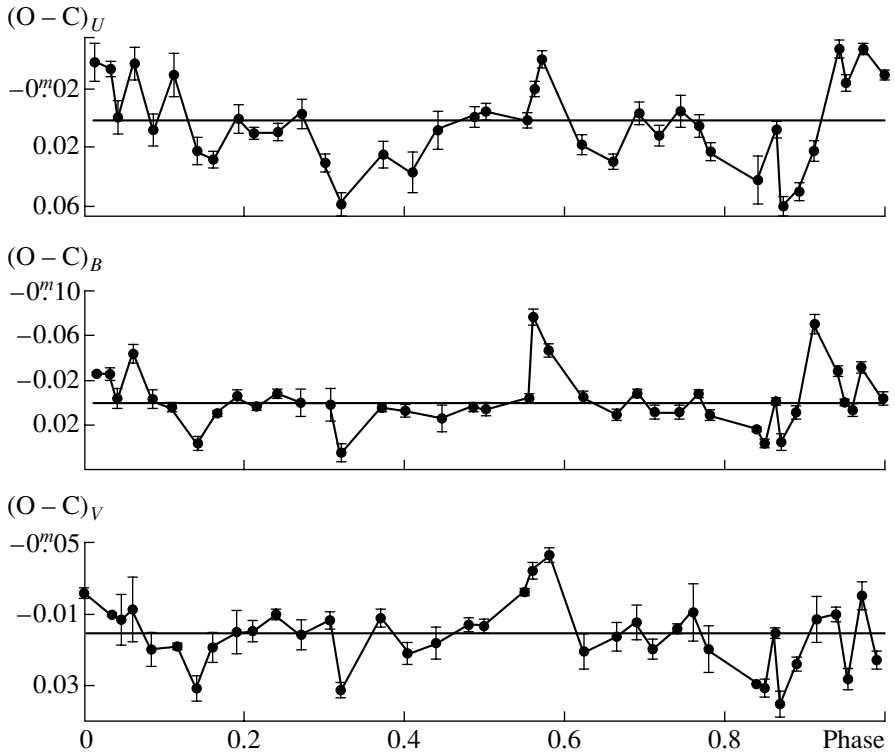

Fig. 3. Deviations of the 1975–1984 observations of UU Cas from the model light curve.

well as the periodic screening by the envelope, which influences the shape of the light curve. We also took into consideration the results of the hydrodynamical computations of the structure of matter flows in semi-detached binary systems of Bisikalo *et al.* [18, 19].

The presence of circumstellar gas can readily explain the high limb-darkening coefficients of the components [16, 17]. The common envelope should also contribute additional light, L_3 [16, 17]. However, we were not successful in estimating this contribution and taking it into account in our solution. The large deviations in the orbital inclination angles, i, for different bands could be due to this additional light, which may be different in different bands. In this case, the effect of the common envelope (which is also different in different bands) requires as a lower limit that $L_3 = 0.1$ of the combined brightness of the system in the U band. Taking into account the contribution of the envelope using values up to $L_3 = 0.1$ does not influence the derived parameters of the system, except for the orbital inclination angle i. However, the sum of squared deviations of the observed curve from the theoretical curve grows linearly. Table 3 shows that the contribution of the third light is largest in the U band.

The very large contribution of the third light, the limb-darkening coefficients $X = 1$, characteristic of cool stars, and deviations from the model curve reaching 0.1^m testify to a very large contribution of gaseous structures in the system, comparable to that of the component stars.

Table 5. Sample correlation coefficients between the deviation curves for the $UBVR$ observations of 1984–1989

	B	t_{Bi}	V	t_{vi}	R	t_{Ri}
U	0.018	0.127	0.010	0.074	0.153	1.103
B			0.238	1.750	0.306	2.298
V					0.491	4.026

Note: $t_{\rm crit} = 2.007$.

Table 6. Sample correlation coefficients between the deviation curves for corresponding bands in 1975–1984 (rows) and 1984–1989 (columns)

	U	$t_{\rm crit}$	B	$t_{\rm crit}$	V	$t_{\rm crit}$	R	$t_{\rm crit}$
U	−0.073	−0.453	0.344	2.258	0.064	0.376	0.143	0.889
B	−0.092	−0.568	0.366	2.423	0.169	1.057	−0.073	−0.450
V	−0.157	−0.983	0.441	3.031	0.259	1.904	0.101	0.628

Note: $t_{\rm crit} = 2.02$.

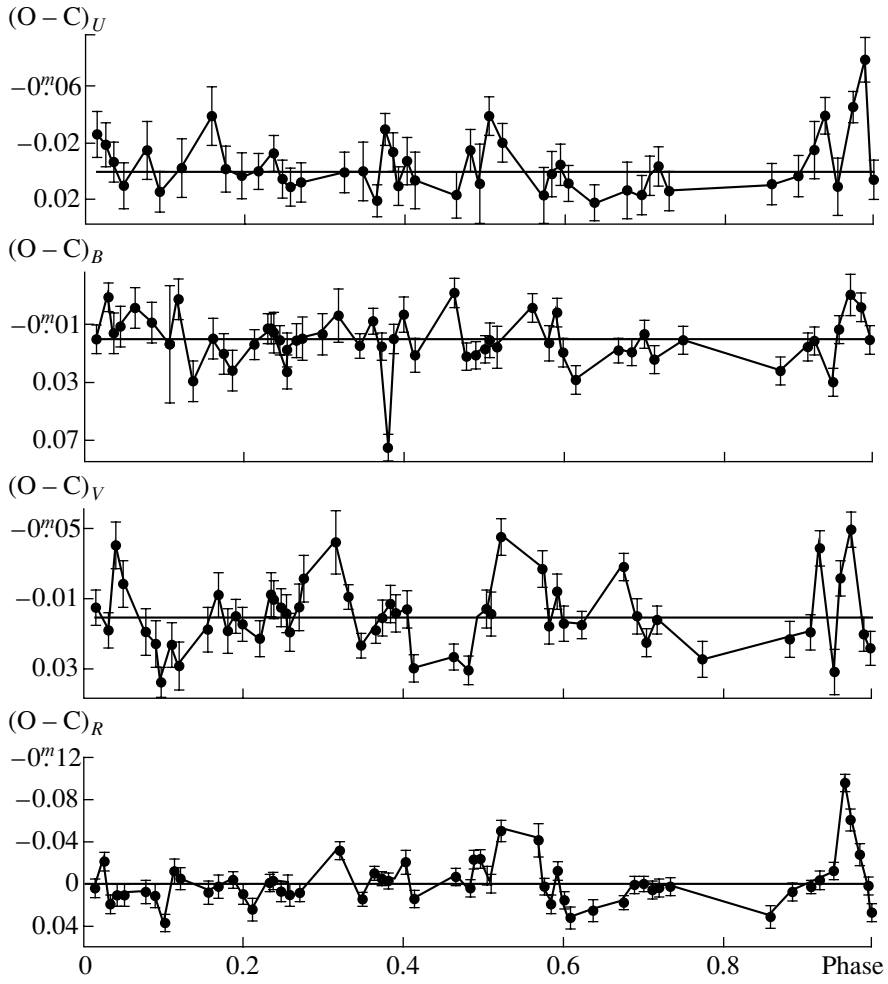

Fig. 4. Deviations of the 1984–1989 observations of UU Cas from the model light curve.

We believe the overfilling of the inner critical surface of the primary obtained for a model consisting of two triaxial ellipsoids can be explained using the model of Bisikalo *et al*. [18, 19]. It follows from [20, 21] that the flows of matter in semi-detached systems lead to the formation of a common envelope. The influence of the common envelope on the morphology of the flows was first considered in [22], where the common envelope was taken to be gas filling the space between the components of the system and not participating in the accretion process. Bisikalo *et al*. [22] showed that the presence of a common envelope in a system significantly influences the flow of matter near the Roche lobe of the component from which the flow originates. In the stationary regime, a large fraction of the surface of the donor star accretes gas from the common envelope, preventing gas from flowing along the Roche lobe to the point L_1. The illustrations in [22] show a significant increase in the gas density near the donor star, depending on the parameters considered.

This model suggests that a large amount of gas may have been accumulated near the primary of UU Cas, forming a "cocoon" whose size coincides with the second critical Roche surface. This cocoon is optically thick in all the $UBVR$ bands, so that the apparent radii of the primary derived in all these bands are in good agreement.

Cases of components overfilling their inner critical surfaces are encountered in light-curve analyses based on both direct and inverse solution methods. The following systems can be noted among massive close binary systems with early spectral types on the main sequence:

(1) SV Cen (B1V+B6III), in which the second critical Roche lobe is filled [23];

(2) UW CMa (O7f+O8f), in which the body of the primary in the UV is considerably larger than the inner critical surface [24];

(3) V599 Aql (B3.5+B3.5), in which the primary overfills its Roche lobe by 26% and the secondary by 12% [25];

(4) Y Cyg (BOIV+BOIV), in which the secondary fills its inner critical surface by 111% [26];

(5) V701 Sco (B1.5+B1.5), in which the observed sizes of the components exceed the inner critical surface by 11–13% [27].

The spectroscopic mass of the primary of UU Cas corresponds approximately to an O7 star. However, Martin [1] estimates the spectral type of UU Cas to be B0.5. It appears that the stellar radiation is reprocessed from O7 to B0.5 in the cocoon.

It is likely that the secondary does not fill its inner critical surface but, because of the flow from the primary, has an envelope that fills this surface, whose optical depth depends on the wavelength and exceeds unity in the U band. The radii of the secondary are probably overestimated because of the effect of the variable screening by the common-envelope gas [16, 17], which is the strongest in the U band, as noted above.

The differences of the heights of the maxima of the light curves in different bands could can be due to anisotropy of the common-envelope gas.

A comparison of observations from different intervals differing by more than 200 orbital periods testifies to the presence of both stable and short-lived (less than 80 periods) gaseous structures in the system.

The residual deviations between the observations acquired during the two time intervals considered and the model light curves (Figs. 3, 4) suggest a more complex distribution of gas in the binary system. The figures demonstrate the presence of strong "flickering" whose amplitude depends on the wavelength. The presence of such flickering even at phases with additional strong and prolonged absorption suggests that it originates in the outer regions of the system (two stars in a multi-component envelope).

6. CONCLUSIONS

The results of our photometry and analysis of the observations show that UU Cas has an over-contact configuration, with the primary overfilling its inner critical surface by, on average, 32% and the secondary's apparent size depending significantly on the wavelength.

We explain the primary's overfilling of its inner critical surface using the model suggested in [18, 19, 22]. Gas located near the primary probably forms an optically thick "envelope," observed in the continuum of all the optical spectral bands.

The secondary probably does not fill its inner critical surface but possesses an envelope whose optical depth depends on the wavelength and exceeds unity in the U band.

The circum-system gas in UU Cas has a multi-component structure.

REFERENCES

1. M. Beyer, Astron. Nachr. **258**, 277 (1936).
2. S. M. Selivanov, Tadjik. Obs., No. 1 (1934).
3. P. P. Parenago and B. V. Kukarkin, Peremen. Zvezdy **5**, 287 (1940).
4. Gy. Tolmar, Astron. Nachr. **271**, 21 (1940).
5. S. Gaposchkin, *Annals of the Astronomical Observatory of Harvard College* (The Observatory, Cambridge, 1952), Vol. 118, p. 26.
6. W. Zonn and J. Semeniuk, Acta Astron. **9**, 141 (1959).
7. G. Romano, Ariel. Publ., No. 17 (1959).
8. K. Haussler, Hartha Mitt., No. 3 (1970).
9. E. A. Antokhina and M. I. Kumsiashvili, Astron. Zh. **69**, 52 (1992) [Sov. Astron. **36**, 25 (1992)].
10. T. S. Polushina, Astronomic–Geodesic Studies (in press).
11. R. F. Sanford, Astrophys. J. **79**, 84 (1934).
12. N. Martin, Astron. Astrophys. **17**, 253 (1972).
13. M. I. Lavrov, Tr. Kazan. Gor. Astron. Obs. **53**, 34 (1993).
14. M. A. Svechnikov, Uch. Zap. Ural. Gos. Univ., Ser. Astron. **88** (5), 3 (1969).
15. S. Yu. Gorda and M. A. Svechnikov, Astron. Zh. **76**, 598 (1999) [Astron. Rep. **43**, 521 (1999)].
16. I. B. Pustyl'nik and L. Einasto, Byull. Akad. Nauk Gruz. SSR, Abastumanskaya Astrofiz. Obs. **58**, 121 (1985).
17. I. B. Pustyl'nik and L. Einasto, Byull. Tartussk. Astrofiz. Obs., No. 106, 3 (1990).
18. D. V. Bisikalo, A. A. Boyarchuk, O. A. Kuznetsov, and V. M. Chechetkin, Astron. Zh. **74**, 889 (1997) [Astron. Rep. **41**, 794 (1997)].
19. D. V. Bisikalo, A. A. Boyarchuk, O. A. Kuznetsov, and V. M. Chechetkin, Astron. Zh. **75**, 706 (1998) [Astron. Rep. **42**, 621 (1998)].
20. K. Sawada and T. Matsuda, Mon. Not. R. Astron. Soc. **255**, 17 (1992).
21. D. Molteni, G. Belvedere, and G. Lanzafame, Mon. Not. R. Astron. Soc. **249**, 748 (1991).
22. D. V. Bisikalo, A. A. Boyarchuk, O. A. Kuznetsov, and V. M. Chechetkin, Astron. Zh. **74**, 880 (1997) [Astron. Rep. **41**, 786 (1997)].
23. R. E. Wilson and T. C. Starr, Mon. Not. R. Astron. Soc. **176**, 625 (1976).
24. Y. L. Eaton, Astrophys. J. **220**, 582 (1978).
25. M. A. Svechnikov, *Catalog of Orbital Elements, Masses, and Luminosities of Close Binary Stars* (Irkutskiĭ Univ., Irkutsk, 1986).
26. R. A. Botsula, Peremen. Zvezdy **22**, 707 (1988).
27. R. E. Wilson and K. C. Leung, Astron. Astrophys. **61**, 137 (1977).

Translated by N. Samus'

Astronomy Reports, Vol. 46, No. 11, 2002, pp. 908–917. Translated from Astronomicheskiĭ Zhurnal, Vol. 79, No. 11, 2002, pp. 1008–1018.

Gamma-ray Bursts as a Result of the Interaction of a Shock from a Supernova and a Neutron-Star Companion

Ya. N. Istomin[1] and B. V. Komberg[2]

[1] *Lebedev Physical Institute, Leninskiĭ pr. 53, Moscow, 117924 Russia*

[2] *Astro Space Center, Lebedev Physical Institute, Profsoyuznaya ul. 84/32, Moscow, 117997 Russia*

Received October 30, 2001; in final form, May 23, 2002

Abstract—A supernova explosion in a close binary system in which one of the components is a compact magnetized object (neutron star or white dwarf) can form a narrow "tail" with length $l_t \sim 10^9$ cm, width $h_t \sim 10^8$ cm, and magnetic field $B_t \sim 10^6$, due to the resulting shock wave flowing around the magnetosphere of the compact object. The energy released by the reconnection of magnetic field lines in this tail can accelerate electrons to relativistic speeds ($\gamma \approx 10^4$), creating the conditions required for powerful synchrotron radiation at energies from hundreds of keV to several MeV, i.e., for a gamma-ray burst (GRB). The duration of this radiation will depend on the power of the shock that forms during the supernova. If the shock is not sufficiently powerful to tear off the magnetosphere tail from the compact object, the duration of the GRB will not exceed $l_t/V_A \leq 1$ s, and the conditions necessary for an "afterglow" at softer energies will not arise. If the shock is more powerful, the tail can be torn from the magnetosphere, forming a narrow ejection, which is perceived in its relativistic motion toward the observer ($\Gamma \sim 10^4$) as an afterglow whose duration grows from tens of seconds at gamma-ray energies to tens of days in the optical. This may explain why afterglows are observed only in association with long GRBs ($T_{90} > 10$ s). Very short GRBs ($T_{90} < 0.1$ s) may be local, i.e., low-power, phenomena occurring in close pairs containing compact, magnetized objects, in which there is again an interaction between the magnetosphere of the compact object and a shock wave, but the shock is initiated by a flare on the companion, which is a red-dwarf cataclysmic variable, rather than by a supernova. © *2002 MAIK "Nauka/Interperiodica"*.

1. INTRODUCTION

During the nine years of operation of the American space-borne Compton Gamma-Ray Observatory, BATSE registered more than 2000 triggered cosmic gamma-ray bursts (GRBs) [1]. However, due to the poor angular resolution attainable at γ energies (degrees), it proved difficult to accurately identify GRBs with objects in other wave bands when the burst was observed with only one spacecraft. After the launch of the Italian-Dutch Beppo SAX spacecraft in 1996, whose X-ray (2–30 keV) counters had angular resolutions $< 6'$, it became possible for X-ray telescopes working at 0.5–10 keV to determine the position of the source of the X-ray afterglow with accuracies to $\sim 1'$ some six hours after the onset of the GRB. In turn, this made it possible to identify optical transients associated with GRBs. At present, optical identifications of about two dozen GRBs with $T_{90} > 1$ s have been obtained using large ground-based telescopes and the Hubble Space Telescope [2]. It has been possible to obtain spectra for many of these, though only several days after the GRB (with the exception of GRB 990123, whose optical transient was very bright at the time of the GRB itself, reaching 9^m [3]). In other cases, the optical transients have been much weaker due to the rapid decrease in their luminosities, so that their spectra must be "dragged out" of objects much weaker than $19–20^m$.

Narrow absorption lines of various metallic ions have been observed in the spectra of some optical transients, which could be used to derive $Z_{\rm abs}$ values, which suggested that these objects were at cosmological distances. Firm conclusions about the cosmological nature of GRBs (or at least GRBs with optical transients) became possible on the basis of spectra of the weak ($24–25^m$) optical "bases" that remained after the optical transients had disappeared, which have been interpreted as the radiation of stars in the host galaxies. These spectra revealed lines characteristic of galaxies undergoing bursts of star formation. The colors of the optical "bases" were also consistent with the idea that they corresponded to galactic radiation. The coincidence of $Z_{\rm abs}$ and $Z_{\rm emis}$ in the spectra of the optical transients and X-ray/γ-ray emission of GRB 970508, GRB 980703, GRB 990712, and

1063-7729/02/4611-0908$22.00

GRB 991208 [4] provided conclusive evidence that they were at cosmological distances. Since the range of redshifts for identified GRBs extends from 0.0085 (GRB 980425) to $Z = 3.4$ (GRB 971214) and the observed γ-ray fluxes range from 10^{-8} to 10^{-5} erg/cm^2, the luminosity function of GRBs turns out to be fairly broad. (For more detail about the properties of GRBs, see the review [5].)

The question of the nature of short GRBs ($T_{90} < 0.1$ s) remains open. Based on certain properties of their angular distribution and the form of their $\log N - \log S$ dependence, a number of authors (for example, [6]–[8]) have preferred to interpret them as local (Galactic) phenomena.

In any case, the cosmological distances to some prolonged GRBs made the question of their energy source acute: if the radiation is isotropic, the energies are estimated to be 10^{53-54} erg at hundreds of keV, comparable to the total energy released by massive supernovas, 90% of which is believed to be emitted in the form of neutrinos (see, for example, [9]). This comparison between the phenomena of GRBs and supernovas seems to be supported by the temporal and spatial coincidence of the "compact" supernova SN 1998 bw ($E = 10^{48}$ erg, type SNIb/c) with GRB 980425, identified with a nearby galaxy with $Z = 0.0085$ (see, for example, [10]). In addition, "hills" are observed in the light curves of some optical transients several tens of days after the GRB, which can be interpreted as a contribution from a weak X-ray/γ-ray type-Ib/c supernova that was simultaneous with the GRB (see, for example, [5, 11, 12]).

Another piece of evidence supporting a connection between GRBs and supernovas is the XMM-Newton detection of narrow X-ray lines of ions characteristic of supernova shells (Mg, Si, S, Al, Ca, Ni) in the spectrum of the afterglow of GRB 011211. The velocity of the line-emitting material several hours after the GRB reached 0.1 s [13].

To remove the "energy crisis" that arises in attempts to relate GRBs to supernovas, it has been suggested that GRBs are associated with relativistic ejections that are strongly collimated within a small angle $\Delta\varphi$ and radiate for some time at γ-ray energies. In principle, this makes it possible to decrease the luminosity required by the observed fluxes from GRBs at cosmological distances by a factor of $(\Delta\varphi/4)^2$, which, for $\Delta\varphi \approx 10^{-2}$rad ($\sim 1^\circ$) yields a factor of $\sim 10^5$. Of course, in this case, we must increase the spatial rate of GRBs by this same factor, since only a small fraction of the total number of bursts will be observed. However, this difficulty can be easily circumvented by increasing the volume from which it is possible to observe γ-ray fluxes from GRBs at a level of 10^{-8}–10^{-5} erg/cm^2. In fact, to obtain agreement between the observed rate of GRBs and the supernova rate, it is sufficient to suppose that either GRBs accompany only a rare type of supernova or that each supernova gives rise to a GRB in a narrow relativistic ejection. According to the estimates of [14], we have

$$n_{\rm GRB} < 2 \times 10^{-8}\ {\rm yr}^{-1} \text{ per galaxy with} L \sim L_*,$$

$$n_{\rm SN} \sim 2 \times 10^{-2}\ {\rm yr}^{-1}$$
$$\text{per galaxy with } L \sim L_* \text{ (at } Z \sim 1)$$

where L_* is the luminosity of a galaxy located near the break in the galaxy luminosity function. Hence, we have $n_{\rm GRB}/n_{\rm SN} < 10^{-6}$; i.e., one GRB occurs per 10^6 supernovas, or each supernova is associated with a GRB if $\Delta\varphi \sim 1^\circ \approx 4(n_{\rm GRB}/n_{\rm SN})^{1/2} \sim 10^{-2}$ rad (see also [10, 15]).

The mechanism for generating the γ radiation in a narrow cone remains unclear, though various possibilities have been proposed. For example, Paczynski [16] once expressed the view that an object with special properties (a "hypernova") will form during the coalescence of two neutron stars. However, Blinnikov *et al.* [17] noted that the energy of a hypernova explosion could not exceed $10^{-3}\ {\rm M_{NS}\ c^2} = 10^{51}$ erg, which is insufficient to explain the energies of cosmological GRBs if their radiation is isotropic. In addition, the link between long GRBs and supernovas in starburst galaxies suggests a connection with explosions of massive stars, i.e., with type I supernovas. It is also not ruled out that the supernova precursors could be Wolf–Rayet stars [18]. This led Paczynski [19] to propose a connection between GRBs and strongly anisotropic supernova explosions of massive stars. He suggested that these ejections lose energy with time and become isotropic via their interaction with the interstellar medium. Thus, the remnant of a GRB could be observed in the radio as compact double structures (not unlike so-called "microquasars"). In [20], SN 1987a in the LMC is suggested as an example of a remnant of a GRB whose relativistic jet did not coincide with the line of sight toward the Earth.

The idea of a possible connection between GRBs and very anisotropic supernova explosions has been extensively discussed in the literature (see, for example, [21]). Initially, anisotropic supernova explosions were invoked to explain the high peculiar velocities ($\sim$400 km/s) of both single and double radio pulsars (see, for example, [22]). The much lower peculiar velocities of millisecond pulsars (< 100 km/s) [23] could be explained if they were not produced by the disruption of close pairs in which their companions exploded but were in close pairs in the central regions of globular clusters that were disrupted during interactions with background stars [24]. It is not difficult to obtain a modest amount of anisotropy during a

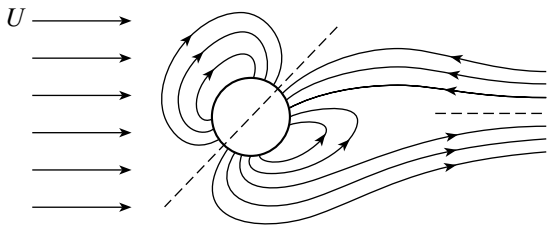

Fig. 1. Development of a magnetosphere tail during the interaction between a shock (with velocity U) from a supernova and its companion (neutron star or white dwarf) in a close pair. The energy of the shock is not enough to tear off part of the tail (the case $T_{\rm GRB} < 1$ s, without an afterglow).

supernova, especially in magnetorotational models for the explosions (see, for example, [25, 26]). However, it is not easy to obtain the high degree of anisotropy needed to reconcile the energetics of cosmological GRBs with the observed fluxes (see the review [27]).

Other possible explanations for the strong directivity of the γ radiation in GRBs and their relationship to supernovas are also encountered in the literature. For example, Milgrom and Usov [28] consider the action of a GRB on a white dwarf with which it forms a close pair, and suggest this could lead to the explosion of the white dwarf, which is observed as a supernova such as SN 1998 bw (see also [29]). Protheroe and Bednarek [30] propose that GRBs are produced in the interaction of the shock wave from a type Ib/c supernova with a companion. In this case, electrons can be accelerated to very high energies, leading to the radiation of γ rays in a narrow cone. Dar and De R'yula [31] consider a "mortar" GRB model in which a narrow ejection of individual relativistic plasma blobs develops during the formation of a thick disk around a neutron star, made up of the accreting products of a supernova. Finally, Umeda [32] suggests a scenario in which the GRB is associated with the interaction of a relativistic ejection that arises in a very asymmetrical supernova explosion with a thick envelope that was ejected by the supernova precursor.

Thus, current concepts about the nature of GRBs require a combination of two conditions: a supernova explosion (possibly of a special type) and the formation of a narrow (opening angle less than a degree) beam of relativistic particles radiating from X-ray to γ-ray energies. Since strongly anisotropic supernova explosions seem unlikely to us, we propose a model in which a massive supernova precursor is in a close binary system with a neutron star; the GRB arises during the interaction of the fast shock wave generated during the supernova with the magnetosphere of the neutron star. A narrow magnetosphere tail can form, in which stored magnetic energy is dissipated in the process of magnetic reconnection, and can accelerate charged particles to relativistic speeds ($\gamma = 10^4$). (This is essentially an analog of magnetospheric flares during the interaction of the solar wind with the magnetosphere of the Earth.) Synchrotron radiation by these particles in the magnetic "tail" ($B_t \sim 10^6$ G) concentrated in a narrow cone ($\Delta\varphi \sim 1/\gamma \sim 10^{-4}$) could be perceived by an observer as a burst of γ radiation if the line of sight to the Earth coincides with the direction of the "tail."

To our knowledge, there is no treatment of this problem in the framework of three-dimensional magnetohydrodynamics in the literature. However, the results of Morietta *et al.* [33], who present two-dimensional numerical simulations of the hydrodynamical interaction of a shock from a type Ia supernova with a subgiant, red giant, or main-sequence companion, suggest that a narrow ejection in the direction of propagation of the shock will also form if the shock compresses the magnetosphere of a neutron star. Therefore, it is of interest to obtain preliminary estimates of the characteristic parameters of this process, to qualitatively investigate its relevance to GRBs.

2. FORMATION OF THE MAGNETOSPHERE TAIL

(1) As an example, we present estimates for a not-very-close pair ($a = 10^{13}$ cm, $V_{\rm orb} = 200$ km/s, $P_{\rm orb} = 30^{\rm d}$) consisting of a blue supergiant ($M = 20M_\odot$, $R_* = 50R_\odot$) and a neutron star ($M = 1.4M_\odot$, $R_{\rm NS} = 10^6$ cm, $B_0 = 10^{12}$ G). The blue supergiant loses its extended envelope in the presupernova stage and can explode as a "compact" supernova (SN I b/c). According to the review [9], the parameters of the shock associated with the "recoil" will be

$$E^0_{\rm kin} = 10^{47}\ {\rm erg}, \quad \Delta M = 2 \times 10^{27}\ {\rm g},$$
$$\rho_{\rm sh} = 10^{-8}\ {\rm g/cm^3} = 10^{16}\ {\rm protons/cm^3},$$
$$h_{\rm sh} = 10^9\ {\rm cm}, \quad V_{\rm sh} = 4 \times 10^9\ {\rm cm/s}$$
$$\text{and } T_{\rm sh} \approx 3 \times 10^6 {\rm K}.$$

Applying simplifying assumptions, let us consider the consequences of an interaction between the shock and the magnetosphere of the neutron star or white dwarf companion (Fig. 1). The shock arising during the supernova interacts with the dipole magnetic field of the neutron star ($B = B_0(R^3/r^3)$). At a distance $r^* = R(B_0^2/4\pi\rho_{\rm sh}V_{\rm sh}^2)^{1/6}$ from the neutron star, the kinetic energy of the shock is comparable to the pressure of the magnetic field. The surface $r = r^*$ can be considered the Alfvén surface, since the velocity of the plasma flow $V_{\rm sh}$ is comparable to the Alfvén

velocity $V_A = (B^2/4\pi\rho)^{1/2}$. In the region $r > r^*$, the velocity of the shock U begins to depend on r, $U^2 = V_{\rm sh}^2[1 - (r^*)^6/r^6]$, leading to its focusing behind the "target" of radius r^*. The condition for this focusing can be written

$$V_{\rm sh}^2[1 - (r^*)^6/r^6] = (r^2 + l^2)/\tau^2,$$

where l is the distance from the neutron star to the region of focusing (the length along the magnetosphere tail) and τ is the time required for the focusing.

It follows from the form of the dependences of the left-hand and right-hand sides of this equation on the distance r that the cumulative effect of the energy of the shock propagating at different r values occurs near the point $r = r_c$. Thus, due to the cumulative effect, the energy of the shock is focused from the surface with radius

$$r_c = r^*[3(V_{\rm sh}^2\tau^2/(r^*)^2)]^{1/8}.$$

For $r > r^*$, we have $V_{\rm sh}^2\tau^2 = l^2$, so that

$$r_c = 3^{1/8} r^* (l/r^*)^{1/4}.$$

As a result, we find that a shock from the region $r = r_c$ is focused in the magnetosphere tail at a distance

$$l = 3^{-1/2} r^* (r_c/r^*)^4.$$

Due to our assumption that the magnetic field is frozen in the plasma flow carried along by the shock, a magnetosphere tail will form in the direction of propagation of the shock, as occurs during the interaction of the magnetosphere of the Earth and the solar wind.

If the width of the tail is $d(l)$ and the magnetic field in the tail is $B_t(l)$, we have by virtue of conservation of the magnetic flux

$$B_t d^2 = B_1 d_1^2,$$

where the subscript 1 corresponds to the field and width at the base of the tail. It follows from the condition that the magnetic field be frozen that [1]

$$B_t = (\rho_t/\rho_{\rm sh})(dl/dr_c)[B^*(r^{*3}/r_c^3)],$$

where B^* is the magnetic field at the Alfvén surface, $B^* = (4\pi\rho V_{\rm sh}^2)^{1/2}$, and $dl/dr_c = 4l/r_c$ is the coefficient of tensile stress of an element of the "fluid."

The density in the tail ρ_t can be estimated from the continuity equation

$$2\pi r_c dr_c V_{\rm sh}\rho_{\rm sh} = 2\pi d(l) dl V_r \rho_t,$$

where $V_r = V_{\rm sh} r_c/l$ is the radial velocity of the plasma flow in the tail. Hence, we have

$$\rho_t = \frac{1}{4}(\rho_{\rm sh}) r_c/d(l)$$

and

$$B_t = B^*(l/d(l))(r^*/r_c)^3.$$

On the other hand, $B_t = B_{t1} d_1^2/d^2(l)$ and, assuming $B_{t1} d_1^2 = B^* r^{*2}$, we can write

$$d(l) = r^*(l/r^*)^{-1/4},$$
$$B_t(l) = B^*(l/r^*)^{1/2}.$$

We can see that the cumulative effect leads to an increase in the magnetic field in the tail as $B_t^2 \sim l^{1/2}$. [2]

It would be natural if the length of the tail L were not very different from the width of the shock $h_{\rm sh}$. In fact, the kinetic energy of the shock is collected starting from the radius $r_c \approx r^*(l/r^*)^{1/4}$ and goes into amplifying the magnetic field in the tail. Therefore, we can write the magnetic energy in the form

$$\varepsilon_B = \int_{r^*}^{L} (B_t^2/8\pi)\pi d^2(l) dl$$

or

$$\varepsilon_B = (B^{*2}/12) r^{*3} (L/r^*)^{3/2}.$$

On the other hand, the kinetic energy of the shock intercepted at the radius r_c is

$$\varepsilon_k = (\rho_{\rm sh}/2) V_{\rm sh}^2 h_{\rm sh} \pi r_c^2 = (B^{*2}/8) h_{\rm sh} r^{*2} (L/r^*)^{1/2}.$$

Equating $\varepsilon_B = \varepsilon_k$, we obtain $L \approx h_{\rm sh}$. It follows that the energy contained in the magnetic field of the magnetosphere tail will be

$$\varepsilon_B = (1/8) B_0^{1/2} (4\pi\rho_{\rm sh} V_{\rm sh}^2)^{3/4} (R_{\rm NS} h_{\rm sh})^{3/2}$$
$$= (1/8) B_0^{1/2} B^{*3/2} (R_{\rm NS} h_{\rm sh})^{3/2}.$$

Substituting our adopted values for the neutron star and shock,

$$B_0 = 10^{12}\ {\rm G}, \quad R_{\rm NS} = 10^6\ {\rm cm},$$
$$V_{\rm sh} = 4 \times 10^9\ {\rm cm/s}, \quad \rho_{\rm sh} = 10^{-8}\ {\rm g/cm^3}$$
$$\text{and } h_{\rm sh} = 10^9\ {\rm cm},$$

we finally obtain

$$B^* = (4\pi\rho_{\rm sh} V_{\rm sh}^2)^{1/2}$$
$$= 1.4 \times 10^6 (\rho_{\rm sh}/10^{-8})^{1/2} (V_{\rm sh}/4 \times 10^9)\ {\rm G},$$

$$r^* = R_{\rm NS}(B_0/B^*)^{1/3}$$
$$= 10^8 (R_{\rm NS}/10^6)(B_0/10^{12})^{1/3} (B^*/10^6)^{-1/3}\ {\rm cm},$$

[1] This condition is that B/ρ be proportional to the fluid element in which the magnetic field is frozen.

[2] This is analogous to the amplification of the magnetic field during the explosive compression of a conducting medium—a mechanism proposed by Sakharov [34] to produce very strong magnetic fields.

$$\varepsilon_B = 4 \times 10^{36}(B_0/10^{12})^{1/2} \times (B^*/10^6)^{3/2}(R_{\rm NS}/10^6)^{3/2}(h_{\rm sh}/10^9)^{3/2}\ \text{erg}.$$

For white dwarfs with $B_0 = 10^9$ G and $R_{\rm WD} = 10^9$ cm, the intercepted shock energy that is transformed into energy of the magnetic field is even greater than for the neutron-star case:

$$\varepsilon_B = 4 \times 10^{39}(B_0/10^9)^{1/2}(B^*/10^6)^{3/2} \times (R_{\rm WD}/10^9)^{3/2}(h_{\rm sh}/10^9)^{3/2}\ \text{erg}.$$

Recall that we adopted parameters for the shock "recoil" corresponding to a "compact" type Ib/c supernova. For other types of supernovas, the velocity and thickness of the shock, and therefore its kinetic energy, could be higher. This should lead to an increase in the value of ε_B in our model (see, for example, [35]).

(2) Let us now consider the situation that arises in a magnetosphere tail with length L, radius $d \approx r^*$ and magnetic field $B_t(l) = B^*(l/r^*)^{1/2}$ in which the conditions for development of a neutral current layer are realized. Charged particles accelerated in the shock front can appear in the tail when it is compressed by the shock. In addition, reconnection of the magnetic-field lines can also lead to particle acceleration (see, for example, [36–39]). We can estimate the characteristic energy the particles can obtain over the time required for the development of the magnetosphere tail to be $\tau_+ \approx L/V_{\rm sh} = h_{\rm sh}/V_{\rm sh}$, which is approximately equal to the time for its destruction $\tau_- \approx h_{\rm sh}/V_A \approx h_{\rm sh}/V_{\rm sh}$. The electric field E accelerating the particles perpendicular to the current layer can reach the fairly substantial magnitude

$$E = (d/c\tau)B_t \approx (r^*V_{\rm sh}/h_{\rm sh}c)B_t = 10^{-2}B^* \sim 300 \times 10^4\ \text{V/cm}.$$

The characteristic energy of the particles accelerated by this field will be determined by the balance between their acceleration and energy losses to synchrotron radiation in the field $B_t \approx B^*$:

$$d\varepsilon/dt = ecE - (2/3)(e^4B^2)(m^2c^3)\gamma^2.$$

We can then estimate the Lorentz factor of the radiating particles:

$$\gamma^2 = (3/2)(m^2c^4E)/(e^3B^2) = (3/2)(c/r_e\omega_c)(E/B) \approx (3/2)(r^*V_{\rm sh})/r_e\omega_c h_{\rm sh},$$

where the cyclotron frequency $\omega_c = eB/mc$ and $r_e = e^2/mc^2$. We obtain for $B \approx B_t \approx B^*$

$$\gamma = 10^4(r^*/10^8\ \text{cm})^{1/2}(V_{\rm sh}/4 \times 10^9\ \text{cm/s})^{1/2} \times (h_{\rm sh}/10^9\ \text{cm})^{-1/2}(B^*/10^6\ \text{G})^{-1/2}.$$

We see that the mean energy of the accelerated electrons is $\varepsilon_e \approx m_ec^2\gamma \approx 5$ GeV, which enables them to emit synchrotron radiation in the magnetic field of the tail at the frequency $\nu_s \sim \omega_c\gamma^2$, corresponding to the mean energy $\varepsilon_{\rm ph} \approx 500$ keV. This value is close to the maximum γ spectral flux densities of GRBs.

The degree of directivity of the nonthermal hard radiation emitted by the magnetosphere tail is determined, not only by the radiation of individual particles, but also by the overall geometry of the radiating region. It is well known that the directivity of synchrotron radiation is $\Delta\varphi \sim \gamma^{-1}$; i.e., for our case, $\Delta\varphi \approx 10^{-4}$. Due to this factor, the energy radiated in the neutron-star magnetosphere tail will be enhanced by a factor of $\sim (4/\Delta\varphi)^2$ compared to the spherically symmetrical case.

We already noted above that the decrease in the opening angle for the radiation cone of the γ rays $\Delta\varphi$ makes it possible to decrease the inferred energy released by the GRB by a factor of $(\Delta\varphi)^2$ (compared to the energy required if the radiation is isotropic). However, in this case, the real number of GRBs must exceed the observed number by a factor of $(\Delta\varphi)^{-2}$. Therefore, we must address the question of whether the value $\Delta\varphi \sim 10^{-4}$ in our model is consistent with the observed rate of supernovas taken to be responsible for GRBs at cosmological distances. It is not difficult to demonstrate that, if we assume that it is possible to observe GRBs right to the boundary of the visible Universe, reasonable consistency is obtained. If we have ~ 300 GRB/yr occurring in $\sim 10^{11}$ galaxies within the observable Universe, we obtain $\sim 3 \times 10^{-9}$ GRB/yr per galaxy. The mean supernova rate per galaxy can be taken to be ~ 0.3 supernova/yr (taking into account that the star-formation rate was higher at earlier cosmological epochs than today). Thus, we can immediately conclude that either only ~ 1 supernova of 10^8 supernovas in the Universe generates a GRB or each supernova is associated with a GRB, but its γ radiation is concentrated in a narrow cone with opening angle $\Delta\varphi = 10^{-4}$.

Thus, we have for neutron stars $\varepsilon_{\rm eff} = 16(\Delta\varphi)^{-2}\varepsilon_B \approx 10^{45}$ erg. According to our assumptions, the energy stored in the tail magnetic field is radiated in the form of electromagnetic radiation by accelerated particles (in the annihilation of magnetic fields during the passage of the shock) on characteristic times $\tau \approx L/V_A \approx h_{\rm sh}/V_{\rm sh} \approx 0.25$ s, as is typical of "short" GRBs (see, for example, [40]).

We already noted that a number of researchers have suggested that short GRBs ($T_{90} < 1$ s) may belong to a "local" population ($r < 10$ kpc), in which case energetic problems are removed. However, if

GRBs are directly associated with supernovas, a local character for GRBs is excluded on statistical grounds. Due to the high degree of collimation of the γ radiation in our model ($\Delta\varphi \sim 10^{-4}$), the real number of short GRBs should exceed the observed number ($\sim$10/yr) by a factor of $\sim (1/\Delta\varphi)^2$. Since each GRB should be accompanied by a supernova, there is no way to reconcile this value with the supernova rate in the Galaxy without invoking strong anisotropy for the radiation of the supernovas themselves (which we have rejected in our model).

(3) There remains one possibility to realize a local population of short GRBs, associated with the possibility that the development of a magnetosphere tail (and subsequent magnetosphere flare) could occur in association with much more common manifestations of stellar magnetic activity in close binaries with compact components. Magnetoactive stellar systems include cataclysmic variables, RS CVn stars, and "inter-binary flares" [41–43]. Although the energy released in the flares in such systems does not exceed 10^{35}–10^{38} erg, due to the magnetic connection between the components, it is possible that all this energy could be channeled to the compact component. Then, the action of the flare on the magnetosphere of the neutron star or white dwarf becomes comparable to the action of a supernova shock wave, given the small cross section for the shock interception at the Alfvén radius ($\sim 10^{-11}$). Taking into account the rate of flares in such systems (1/10 yr), their spatial density could reach $\sim 10^{-7}$–10^{-8} pc^{-3} yr^{-1}, which could plausibly be consistent with the observed and real frequencies of short GRBs if we suppose that the associated γ-ray flares can be observed to distances $\sim$20 kpc, but the optical flares initiating the GRBs only to distances < 20 pc. In this case, the ratio of the real number of bursts in a volume with $r = 20$ kpc to the observed number in a volume with $r = 20$ pc will be $(20\ \text{kpc}/20\ \text{pc})^3 \approx 10^9$ ($\sim$10/yr).

We should note here that the possibility of a connection between GRBs and flare stars has been discussed in the literature for a long time (e.g., [44–46]). These studies have cited similarities between the profiles of stellar flares and GRBs, as well as the plausible consistency in the GRB detection rate and the spatial density of flare stars (if both are local phenomena and have the same ratio $F_{\gamma R}/F_{\text{opt}}$). Of course, early studies did not separate GRBs into short and long bursts, and did not consider the hypothesis that the GRB radiation was strongly collimated. A number of authors subsequently turned to this possibility [47–49], especially in connection with flare stars displaying magnetic activity.

Thus, we conclude that, in our model, Galactic (local) GRBs with $T_{90} < 1$ s could be associated with close binaries consisting of a magnetically active flare star and a compact object (neutron star or white dwarf). At the same time, extragalactic GRBs with $T > 1$ s are associated with close binaries in which the compact object is subject to the action of a shock generated by the explosion of its companion as a supernova.

Since the shock kinetic energy intercepted at the Alfvén radius of the compact object is $\sim a^{-3/2}$, more powerful GRBs will arise in more compact systems. In addition, since the duration of a GRB is $\tau \approx L/V_A \sim h_{\text{sh}}/B^* \sim a^{-1}$, longer GRBs will be generated in closer systems. It is possible that this brings about the distinction between long (cosmological) and short (local) GRBs: the former arise in closer systems, while the latter arise in systems with larger separations. This makes it possible to understand the two-peaked nature of the distribution of GRB durations, with one maximum at $T_{90} \approx 0.3$ s (local GRBs) and the second at $T_{90} \approx 30$ s (cosmological GRBs) (see, for example, [50]).

In concluding this section, we note that, varying the input parameters of our model (the kinetic energy of the shock from the supernova E^0_{kin}, magnetic field at the surface of the compact object B_0, major axis of the stellar system a), taking into account the very narrow ($\sim 1'$) cone for the synchrotron radiation by the relativistic particles ($\gamma = 10^4$), we can obtain agreement with the energy released by cosmological GRBs ($E_{\text{GRB}} = 10^{53}$ erg recalculated in terms of spherically symmetric radiation (see, for example, [5])). It is easier to obtain larger values of E_{GRB} for systems with white dwarfs than for those with neutron stars. However, attempts to solve the "energy catastrophe" for cosmological GRBs by decreasing the opening angle for the γ radiation cone lead to statistical difficulties in comparisons of the observed rates of supernovas and GRBs. We noted above that the solution to this discrepancy may be associated with the fact that the supernova rate was much higher in the early epochs of evolution of galaxies (i.e., it increases with Z). This may be especially relevant for the central regions of the host galaxies, where, according to [51], bright GRBs are most often observed.

3. RELATIVISTIC EJECTION

There is no question that our model of a GRB as a magnetospheric flare (or flares) on a neutron star (or white dwarf) requires numerical simulations if we wish to obtain trustworthy information about the possible natures of long and short GRBs in the context of our model. However, even without such simulations, we can see that our "magnetospheric" model can give rise to a number of interesting and possibly verifiable

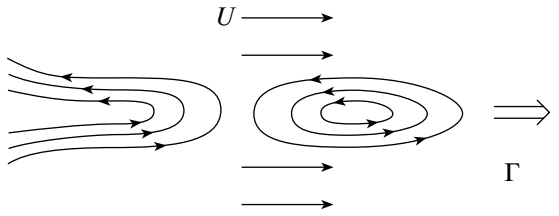

Fig. 2. Case when the shock energy is sufficient to tear off part of the tail as a result of global reconnection of magnetic force lines (the tearing instability). In this case, $T_{\rm GRB} > 1$ s, and the evolution of the relativistic blob of plasma (with Lorentz factor $\Gamma \sim 10^4$) flying toward the observer can explain the properties of the afterglows.

consequences and also that it poses a whole series of questions which we would like to answer. The main question is the nature of the X-ray and optical afterglows (for properties of the afterglows, see, for example, [5]). Let us consider this question in more detail in the context of our model.

In our view, the afterglows could be associated with the fact that, in some cases, the magnetosphere tail formed by the shock during its interaction with its magnetized companion could be torn as a result of the global reconnection of magnetic-field lines in the tail (the tearing instability; Fig. 2). This type of phenomenon is observed in strong chromospheric flares on the Sun [52, 53]. As a result, part of the tail could be torn off and acquire an appreciable bulk kinetic energy characterized by a Lorentz factor Γ whose magnitude will be comparable to that estimated earlier for the electrons accelerated in the tail current layer, $\gamma \approx 10^4$. Thus, a narrow ($l > d$), magnetized ($B^* \approx B$) relativistic ejection could be observed, with a stored internal energy $\varepsilon \approx \varepsilon_{\rm B}$. If a close binary consisting of a neutron star/white dwarf and a supernova is oriented "edge-on" to an observer and the ejection occurs roughly along the line of sight, we can estimate the power of the radiation of the ejected magnetized blob.

Let the magnetic field in a coordinate system moving with the ejected magnetized blob be B and the density of particles with mean Lorentz factor γ be n. The Lorentz factor γ will decrease with time as a result of the synchrotron radiation emitted by the charged particles. Within the blob, an equipartition regime, $B^2 = 8\pi mc^2\gamma n$, will be supported due to the continuous "micro-reconnection" of field lines. At the same time, since the particles are frozen in the magnetic field, their density will be $n \sim B$, so that $n = n_0 B/B_0$ (the subscript 0 refers to initial values). It follows that

$$B = 8\pi mc^2(n_0/B_0)\gamma.$$

We have in the case of adiabatic expansion of the blob conserving magnetic flux $d = d_0(B_0/B)^{1/2}$, and n and B will decrease with time. Since, for our parameter values ($n_0 \sim 10^{13}$ cm^{-3}, $L_0 = 10^9$ cm), the optical depth of the blob to Thomson scattering is small ($\tau = n_0 L_0 \sigma_{\rm T} \ll 1$), we can consider the emitted radiation to freely escape. Therefore, the cooling is determined by the synchrotron losses:

$$mc^2(d\gamma/dt) = eEc - (2/3)(e^4B^2/m^2c^3)\gamma^2,$$

where E is the induced electric field perpendicular to the ejection direction, which arises due to the time variation of the magnetic field $E = -(r^*/c)(dB/dt)$. We can now easily obtain an expression for the evolution of the mean energy of the particles:

$$d\gamma/dt[1 + (8\pi r^* e n_0/B_0)] = -(2/3)(e^4/m^3c^5)(8\pi mc^2(n_0/B_0))^2\gamma^4.$$

The term in square brackets describes the betatron cooling of the particles as the magnetic field is decreased:

$$(8\pi r^* e n_0)/B_0 = 2r^*\omega_{\rm po}^2/c\omega_{\rm co},$$

where $\omega_{\rm po}$ is the plasma frequency of the particles in the ejected blob and $\omega_{\rm co}$ is the cyclotron frequency at the initial time t_0. For our case, with $\omega_{\rm po}^2 = 3 \times 10^{22}$ s^{-2} and $\omega_{\rm co} = 2 \times 10^{13}$ s^{-1}, we have $r^* = 10^8$ cm, $r^*\omega_{\rm po}^2/c\omega_{\rm po}^2 \gg 1$, and we can write

$$\gamma^{-3} - \gamma_0^{-3} = t/\tau,$$

where $\tau = r^*\omega_{\rm co}/4\omega_{\rm po}^2 r_e \approx 2 \times 10^4$ yr. If the times considered are not too small, we have in the coordinate system moving with the blob ($t > \tau\gamma_0^{-3}$) $\gamma = (t/\tau)^{-1/3}$ and $B = (t/\tau)^{-1/3}$.

The characteristic frequency $\omega = \omega_c\gamma^2$ at which the relativistic particles emit synchrotron radiation will change with time:

$$\omega = (2\omega_{\rm po}^2/\omega_{\rm co})(t/\tau)^{-1} \sim 1/t.$$

With this $\omega(t)$ dependence, the observed frequency $\omega' = \Gamma\omega$ and time in the observer's rest frame $t' = t/\Gamma$ will be related by the expression

$$t' = 2\tau(\omega_{\rm po}^2/\omega_{\rm co}\omega') \equiv (1/2)(r^*/r_e)(1/\omega') \sim 1/\omega'.$$

We can see that the radiative cooling time in the observer's frame at a given frequency will be $t'[{\rm s}] = 2 \times 10^5/(h\omega')$ [eV]. For the photon energy $h\omega' \approx 0.3$ MeV characteristic for GRBs, the cooling time is approximately 10 s. This corresponds to the maximum in the distribution of durations of long GRBs corresponding to a decrease to 90% of their peak

luminosity (T_{90}). Observations indicate that it is precisely long GRBs ($T_{90} > 10$ s) that are sometimes accompanied by afterglows in the X-ray and/or optical. In our model, the X-ray emission ($h\omega' = 100$ eV) will have a duration on the order of several days, while the duration of the optical emission ($h\omega' \approx 1$ eV) will be several months, consistent with the observational data.

It is not difficult to estimate the rate of variation of the afterglow intensity for our assumptions: $I(\omega') \sim (\omega')^{4/3} \sim (t')^{-1.33}$. The observations (see, for example, [5]) show the dependence $I \sim (t')^{-1.2}$, consistent with our estimates. In addition, the colors of the optical afterglows show little time variability [54], also consistent with our estimates for the time variations expected for the intensity and characteristic frequency of the afterglows: $\omega' \sim (t')^{-1}$ and $I \sim (t')^{-1.33}$.

It is likely that, in many cases, the energy of the shock turns out to be insufficient to tear off the magnetosphere tail from the magnetic companion to the supernova, in which case the GRB will not display an afterglow. This situation is most probable for less energetic GRBs, which will also be shorter GRBs ($T_{90} < 1$ s). It is possible that this is precisely why afterglows have not been observed for short GRBs.

In concluding this section, we note that X-ray emission features have recently been detected in the afterglows of four GRBs (GRB 970828, GRB 991216, GRB 060214, and GRB 970508), as well as a transient absorption feature in the case of GRB 990705, which have been interpreted as the K_α (6.4 keV) line of highly ionized iron [55–57]. These lines have large widths ($> 10\,000$ km/s) and intensities corresponding to $M_{\rm Fe} \geq 0.1 M_\odot$. They appear $\sim 10^5$ s after the γ-ray burst, indicating distances to the region in which they are formed of $\sim 10^{15}$–10^{16} cm.

The nature of these lines remains unclear (see [58–60]), but one has the impression that their appearance requires the explosion of a supernova that has ejected a massive expanding envelope in the precursor stage, which has moved to distances of $\sim 10^{15}$–10^{16} cm over 10^5 s. The interaction of this envelope with the supernova shock could provide the degree of ionization of iron required to give rise to emission in the K_α line (an analog of Lyα in the hydrogen-like ion of Fe). It is possible in the case of a narrow γ-ray burst that some contribution to the iron-line radiation could be made by the iron crust of the neutron star, which is heated to high temperatures during the passage of the very hot shock and the raining of high-energy charged particles from the magnetosphere tail onto the surface of the neutron star (an "inverse" γ-ray burst). It is interesting that a broad K_α line was observed during a soft γ-ray flare in the object SGR 1900+14, which is a soft γ-ray repeater [61] (for a discussion of the nature of such sources, see, for example, [62] and [63]).

4. CONCLUSION

To remove the "energetic catastrophe" associated with cosmological GRBs, a number of studies have suggested that the γ-ray radiation is very strongly collimated (with radiation-cone opening angles $\Delta\varphi \approx 1^\circ$), which boosts the observed radiation by a factor of $(\Delta\varphi)^2 > 10^3$ compared to models in which the γ radiation is isotropic. In most of these studies, this strong collimation is associated with analogous anisotropy in a supernova explosion, which, in turn, gives rise to the observed GRB energetics.

We have considered another mechanism for the formation of a narrow beam of γ radiation during a GRB. We associate this phenomenon with a magnetospheric flare in the narrow magnetospheric tail of a neutron star or white dwarf, which develops under the action of a shock wave from an isotropic supernova whose precursor was in a binary pair with the compact magnetized star.

As an example, we have considered a binary with major axis $a \sim 10^{13}$ cm consisting of a blue supergiant ($M_* = 20 M_\odot$, $R_* = 50 R_\odot$) and a neutron star ($B_0 = 10^{12}$ G) or white dwarf ($B_0 = 10^9$ G) in which the supergiant explodes as a "compact" type Ib/c supernova (such as SN 1987a). During this explosion, the "recoil" shock wave from the supernova will interact with the dipolar magnetic field of the compact companion, forming a narrow magnetosphere tail in the direction of its propagation ($L = 10^9$ cm, $B_t = 10^6$ G). The magnetic energy stored in this tail can be liberated over a time of about $h_{\rm sh}/V_A \sim 1$ s, $\varepsilon \approx 4 \times 10^{36}$ erg/s for a neutron star or 4×10^{39} erg/s for a white dwarf. This energy release ε_B shows the following dependence on the parameters of the problem: $\varepsilon = f(E^\circ_{\rm kin}, B_0^{1/2}, B_t^{3/2}, R^{*3/2}, h_{\rm sh}^{3/2}, a^{-3/2})$. The strong electric field in the tail $E \approx 3 \times 10^6$ V/cm can accelerate electrons to energies $E \approx 5$ GeV, corresponding to Lorentz factors $\gamma = 10^4$. These electrons can lose energy via synchrotron radiation with characteristic photon energies ~ 0.5 MeV in a narrow cone with opening angle $\Delta\varphi \sim 10^{-4}$ ($\sim 1'$). Thus, taking into account Doppler beaming of the radiation, it is possible to provide the observed energies for GRBs $\varepsilon_{\rm GRB} = \varepsilon_B \gamma^2 \approx 4 \times 10^{44}$ erg/s for a neutron star or 4×10^{47} erg/s for a white dwarf.

Varying $E^\circ_{\rm kin}$ and a, it is possible to bring the calculated value $\varepsilon_{\rm GRB}$ into agreement with the observed energies of cosmological GRBs (to 10^{50}–10^{53} erg).

If short GRBs ($T < 0.1$ s) prove to be local phenomena, they can be explained in our model simply by supposing that the companion of the neutron star or white dwarf is not a supernova precursor but instead is a flaring dwarf (such as a cataclysmic variable). In this case, short GRBs could have a recurrent character.

In some cases, the magnetosphere tail formed by the shock wave during its interaction with the magnetized compact companion may be torn off as a result of global reconnection of the magnetic-field lines (tearing instability), with a local release of magnetic energy in the region of the separation. As a result, the outer part of the tail acquires an appreciable bulk kinetic energy ($\Gamma \approx 10^4$) and forms a narrow, magnetized blob moving with relativistic speed. With time, the size of the ejected blob of plasma will increase, conserving magnetic flux: $d = d_0(B_0/B)^{1/2}$, and the particle density and magnetic field in the blob will decrease. Since the optical depth to Thomson scattering for the adopted parameters ($n_0 = 10^{13}$ cm^{-3}, $l = 10^9$ cm) is much less than unity, the radiation emitted by the relativistic particles can freely escape over a time on the order of 10 s for γ rays with energies ~ 0.3 MeV, several days for X rays (hundreds of eV), several months for optical photons (eV), and several years for radio photons. Thus, the expanding relativistic blob can give rise to the observed properties of the GRB itself and also of the afterglow, whose duration should depend on the energy of the radiated photons. Our estimate of the rate of fading of the afterglow yielded the dependence $\sim t^{-1.33}$, which is close to the observed behavior. The spectral index of the afterglow radiation will vary little with time, since $I(\omega') \sim (\omega^{1.33})$. One possibility is that the energies of the shocks associated with short GRBs are insufficient to tear off the magnetosphere tail, so that they do not display the phenomenon of afterglows.

We also note that, given the synchrotron nature of the radiation of both the GRB itself and its afterglow (at softer energies, including the radio) in our model, the appearance of a modest amount of circular polarization due to the alignment of the spins of the radiating electrons along the magnetic field in the magnetized relativistic blob cannot be ruled out (see, for example, [64]). In addition, we cannot exclude the possible manifestation of "superluminal" motions in radio images of the expanding plasma blobs moving nearly along the line of sight with relativistic speeds obtained with Very Long Baseline Interferometry (as is observed for "microquasars;" see, for example, [65]). The ejection will be one-sided, and its speed must be measured relative to the position of some compact radio source that is nearby on the sky (via so-called phase-referencing observations).

5. ACKNOWLEDGMENTS

In conclusion, the authors express sincere thanks for useful discussions to G.S. Bisnovatyĭ-Kogan, V.G. Kurt, V.V. Sokolov, and D.A. Kompaneĭts. This work was supported by the Russian Foundation for Basic Research (project nos. 01-02-16274, 02-02-16762), the "Cosmomicrophysics" project of the State Science and Technology program "Astronomy," and the program "Non-stationary processes in astronomy" (theme 5).

REFERENCES

1. C. A. Meegan *et al.*, www.batse.msfc.nasa.gov/data (1998).
2. J. Grainer, www.Aip.de/∼jcg/grbrsh.html.
3. S. R. Kulkarni, S. G. Djorgovski, S. C. Odewaln, *et al.*, Nature **348**, 389 (1999).
4. P. M. Vreeswijk, A. Fruchter, L. Kap, *et al.*, Astrophys. J. **546**, 672 (2001).
5. S. G. Djorgovski, D. A. Frail, S. R. Kulkarni, *et al.*, astro-ph/0106574.
6. G. S. Bisnovatyi-Kogan, Astron. Astrophys., Suppl. Ser. **138**, 541 (1999); astro-ph/0103319.
7. D. B. Cline *et al.*, Astrophys. J. **527**, 827 (1999).
8. D. B. Cline, C. Matthey, and S. Otwinovski, astro-ph/0105059.
9. V. S. Imshennik and D. K. Nadezhin, Usp. Fiz. Nauk **156**, 561 (1988).
10. L. Wang and J. C. Wheeler, Astrophys. J. **504**, L87 (1998).
11. E. Baron, Nature **395**, 635 (1988).
12. S. Holland, J. P. U. Fynbo, J. Hjorth, *et al.*, Astron. Astrophys. **371**, 52 (2001).
13. J. N. Reeves, D. Watson, J. P. Osborne, *et al.*, Nature **416**, 512 (2002).
14. V. V. Sokolov, astro-ph/0102492; astro-ph/0107399.
15. R. M. Kippen, M. S. Briggs, J. M. Kommers, *et al.*, Astrophys. J. **506**, L27 (1998).
16. B. Paczynski, Ann. (N.Y.) Acad. Sci. **688**, 321 (1993).
17. S. I. Blinnikov, I. D. Novikov, T. V. Perevodchikova, and A. G. Polnarev, Pis'ma Astron. Zh. **10**, 422 (1984) [Sov. Astron. Lett. **10**, 177 (1984)].
18. A. M. Cherepashchuk and K. A. Postnov, astro-ph/0012512.
19. B. Paczynski, astro-ph/0103384.
20. R. Cen, Astrophys. J. Lett. **524**, L51 (1999).
21. L. Wang and J. C. Wheeler, Astrophys. J. **504**, L87 (1998).
22. R. Cen, Astrophys. J. **507**, L131 (1998).
23. L. Nicastro, F. Nigro, N. D'Amico, *et al.*, Astron. Astrophys. **368**, 1055 (2001).
24. G. S. Bisnovatyĭ-Kogan, Astrofizika **32**, 313 (1990).
25. G. S. Bisnovatyi-Kogan, Astron. Zh. **47**, 813 (1970) [Sov. Astron. **14**, 652 (1971)].
26. B. Paczynski, Astrophys. J. Lett. **365**, L9 (1990).
27. G. S. Bisnovatyi-Kogan, Astrophys. Space Sci. **276**, 259 (2001).

28. M. Milgrom and V. V. Usov, Astrophys. J. **531**, L127 (2000).
29. S. I. Blinnikov, V. S. Imshennik, and D. K. Nadezhin, Astron. Zh. **67**, 1181 (1990) [Sov. Astron. **34**, 595 (1990)].
30. R. J. Protheroe and W. Bednarek, astro-ph/9904279.
31. A. Dar and A. De R'yula, astro-ph/0012227.
32. H. Umeda, astro-ph/9911135.
33. E. Morietta, A. Burrows, and B. Fryxell, Astrophys. J., Suppl. Ser. **128**, 615 (2000).
34. A. D. Sakharov, Usp. Fiz. Nauk **88**, 725 (1966) [Sov. Phys. Usp. **9**, 294 (1966)].
35. J. Scalo and J. C. Wheele, astro-ph/0105369.
36. T. Magura, S. Mineshige, Y. Takaaki, and K. Shibata, Astrophys. J. **466**, 1054 (1996).
37. K. Shibata and T. Yokayma, Astrophys. J. **526**, L49 (1999).
38. H. C. Spruit, F. Daigne, and G. Grenkhahn, Astron. Astrophys. **369**, 694 (2001).
39. A. I. Podgornyĭ and I. M. Podgornyĭ, Astron. Zh. **78**, 71 (2001) [Astron. Rep. **45**, 60 (2001)].
40. M. Tavani, Astrophys. J. **497**, L21 (1998).
41. R. E. Gershberg, *Low-Mass Flare Stars* [in Russian] (Nauka, Moscow, 1978).
42. A. V. Ipatov and A. V. Stepanov, Vistas Astron. **41**, 203 (1997).
43. J. M. Ferreira, Astron. Astrophys. **335**, 248 (1998).
44. E. A. Karitskaya, Astron. Zh. **52**, 189 (1975) [Sov. Astron. **19**, 112 (1975)].
45. M. N. Vahia and A. R. Rao, Astron. Astrophys. **207**, 55 (1988).
46. E. P. Liong and H. Li, Astron. Astrophys. **273**, L53 (1993).
47. A. R. Rao and M. N. Vahia, Astron. Astrophys. **281**, L21 (1994).
48. J. Greiner and C. Motch, Astron. Astrophys. **294**, 177 (1995).
49. B. I. Luchkov and O. M. Pomesheva, Astron. Zh. **75**, 79 (1998) [Astron. Rep. **42**, 68 (1998)].
50. I. V. Belousova, A. Mizaki, T. M. Roganova, and I. L. Rozental', Astron. Zh. **76**, 841 (1999) [Astron. Rep. **43**, 734 (1999)].
51. J. S. Bloom, S. R. Kulkarni, and S. G. Djorgovski, astro-ph/0010176.
52. K. Shibata, S. Masuda, M. Shimojo, *et al.*, Astrophys. J. **451**, L83 (1995).
53. K. V. Getman and M. A. Livshits, Astron. Zh. **77**, 295 (2000) [Astron. Rep. **44**, 255 (2000)].
54. V. Simon, R. Hudec, G. Rizzichini, *et al.*, astro-ph/0108416.
55. D. Lazzati, astro-ph/0011580.
56. F. Pacrels, astro-ph/0004188.
57. L. Amati, F. Frontera, H. Vietri, *et al.*, astro-ph/0012318.
58. P. Meszaros and M. J. Rees, astro-ph/0104402.
59. D. Lazzati, G. Ghisellini, and H. Vietri, astro-ph/0104086.
60. K. Kotake and S. Nagataki, astro-ph/0104485.
61. E. Strohmayer and A. I. Ibrahin, astro-ph/0005431.
62. Ya. I. Istomin and B. V. Komberg, Astron. Zh. **77**, 852 (2000) [Astron. Rep. **44**, 754 (2000)].
63. R. C. Duncan, astro-ph/0103235.
64. D. A. Varshalovich and B. V. Komberg, Astron. Zh. **48**, 1085 (1971) [Sov. Astron. **15**, 858 (1972)].
65. I. F. Mirabel, L. F. Rodriguez, B. Cordier, *et al.*, Nature **358**, 215 (1992).

Translated by D. Gabuzda

Astronomy Reports, Vol. 46, No. 11, 2002, pp. 918–924. Translated from Astronomicheskiĭ Zhurnal, Vol. 79, No. 11, 2002, pp. 1019–1026.

A Spectropolarimetric Study of Ellerman Bombs

L. K. Kashapova

Institute of Solar–Terrestrial Physics, P. O. Box 4026, Irkutsk, 664033 Russia

Received February 5, 2002; in final form, May 23, 2002

Abstract—We have studied four 10 to 40 minute sets of Hα spectropolarimetric observations of five Ellerman bombs (a total of 241 spectropolarimetric recordings) selected from data for more than 200 Ellerman bombs obtained with the Large Solar Vacuum Telescope at the Baĭkal Astrophysical Observatory. The degree of polarization P and azimuth of the plane of polarization were derived from quasi-simultaneous observations of the Stokes parameters Q/I and U/I. We interpret the observed linear polarization as impact polarization. A method for comparing the polarization parameters of Ellerman bombs observed at different times and distances from the center of the solar disk is suggested, which can be used to relate variations of the polarimetric parameters with the lifetimes of Ellerman bombs. A comparison between the observations and theoretical calculations indicates that the observed Ellerman bombs were due to electron beams with energies of several hundred keV. © *2002 MAIK "Nauka/Interperiodica"*.

1. INTRODUCTION

Ellerman bombs (EBs) or "moustaches," are short-lived emission objects whose sizes range from the diffraction limit of modern 1-m-class telescopes to 5″. They are observed as extended and very narrow emission wings around strong absorption lines; no substantial perturbations in the cores of the lines are visible. The morphology, evolution, and dynamics of EBs have been studied in detail [1–5]; however, the nature of these objects remains unclear. In one recent study of the morphology of EBs [6], the observed objects were divided into two classes: those not corresponding to moving magnetic-field features (class I, around 64% of all EBs) and those associated with such structures (class II). The sizes, lifetimes, and brightnesses of EBs belonging to the two classes are not appreciably different.

Several mechanisms for the formation of EBs have been suggested. One hypothesis [7] is that Ellerman bombs originate in laminar flows deep in the chromosphere, where the plasma is divided into at least two layers, with the denser material situated in lower layers. Hydrodynamical instabilities can raise the lower layer into the upper, less dense, layer. As a result, a vortical layer develops, which mixes the fluxes and forms a magnetic-flux "bubble" or "drop" that is heated by ohmic dissipation. Qiu *et al.* [8] studied Ellerman bombs in the blue wing of the Hα line and in the ultraviolet (UV). The optical observations were obtained at a wavelength of Hα-1.3 Å, for which the radiation formed slightly below 400 km above the boundary of the photosphere, while the UV observations were carried out in a narrow section of the UV continuum at 1600 Å, formed in the region of the temperature minimum region. It was first shown that the processes observed at optical and UV wavelengths are well correlated dynamically for most Ellerman bombs that are bright in the blue Hα wing. Based on this fact, Qiu *et al.* [8] suggested that the source of heating of some EBs is located near the temperature minimum region, while the source of heating for others is even deeper, in the photosphere. The bombardment of the chromosphere by beams of energetic particles is considered as a mechanism for exciting EBs in [9, 10]. One advantage of this model is that it can explain the observed linear polarization of Ellerman bombs, along with their brightness. However, Nindos and Zirin [6] restrict the suitability of this mechanism and conclude that impact polarization is not important for EBs, at least those identified as belonging to class II.

The impact polarization in the Hα line arising in a solar flare due to the effect of electron beams on the chromosphere was calculated in the recent study [11]. Zharkova and Syniavskii [11] concluded that the Hα profiles display 2 to 25% linear polarization only in the core of the line, while the line wings are completely depolarized by thermal collisions. In the absence of electron beams, the linear polarization is due to the chromospheric radiation and reaches 2–3%. Thus, the observed polarization of Ellerman bombs must be explained and can also make an important contribution to our overall understanding of the origin of the linear polarization of the solar atmosphere. The degree of polarization, the azimuth of the plane of polarization, the presence of polarization in the center and/or wings of the line, and the polarization variations during the lifetime of the objects are all very

1063-7729/02/4611-0918$22.00

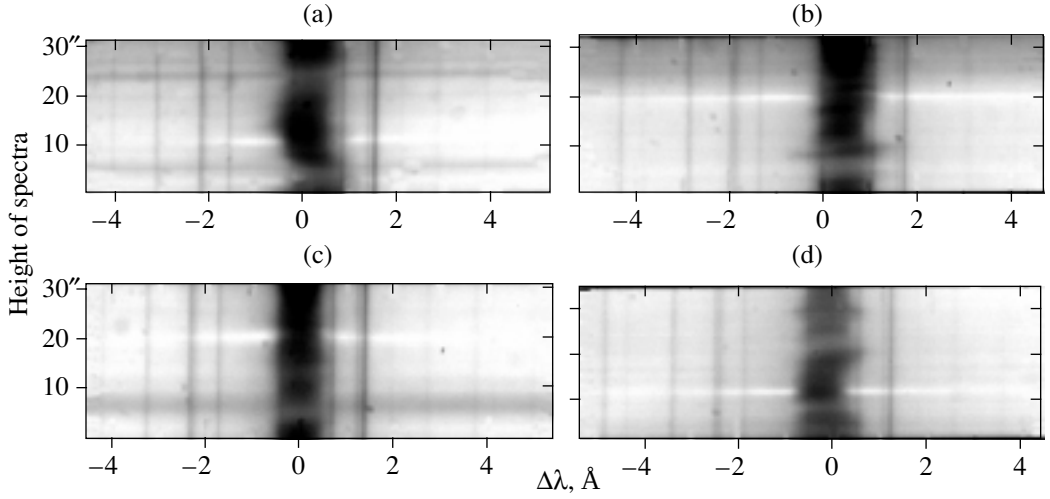

Fig. 1. Spectrograms of Ellerman bombs obtained on (a) July 4, (b) July 5, (c) July 14, and (d) August 7, 1999.

useful pieces of information for our understanding of the mechanism exciting the EBs. However, the polarization of EBs has not been studied as actively as have their structure and motions.

The first studies of the polarization of EBs are those of Babin and Koval' [12–16], based on both spectral observations and observations with a birefringent filter in the region of the Hα line, with photographic recording in both cases. In all cases, linear polarization was detected in the wings of the EBs, with the degree of polarization being 3–10%. In close pairs of EBs (when the total size of the region did not exceed 4″), stronger polarization was observed for the weaker EB. According to these observations, the plane of polarization of EBs is predominantly parallel to the AFS fibers. Babin and Koval' also noted that the azimuth of the polarization plane is different even for spatially close EBs and can vary substantially during their lifetimes.

Firstova [17] presented spectropolarimetric observations of EBs in the Hα and Hβ lines. Polarization was detected at the line centers and did not exceed 7%. Firstova [17] suggested that substantial polarization is observed only in the first minutes of an EB's lifetime. Based on these results, she suggested that the observed polarization was impact polarization.

Rust and Keil [18] obtained observations of EBs with a Fabry–Perot interferometer (with width 6 Å) centered on the Hα line. A digital video system was used to record the images. The integration time was 2–120 s, with the polarizer axis fixed. The azimuth of the polarization plane was not determined from these observations; in a total of 32 objects studied, the polarization did not exceed 8%.

We have also carried out studies of Ellerman bombs [19, 20]; polarization was observed primarily at the line center and did not exceed 13% in [19] and 9.5% in [20]. In most cases, the polarization plane was radial. However, we also detected time variations of the polarization plane.

Here, we analyze the intensities and polarizations of long-lived EBs with high spatial and temporal resolution, to study processes occurring during the lifetimes of these objects.

2. OBSERVATIONS

Spectropolarimetric Hα observations of EBs were carried out in the Summer of 1999 with the Large Solar Vacuum Telescope [21]. The polarizer consisted of a Wollaston prism after the spectral slit and two half-wave plates. One of these, located behind the Wollaston prism, was used to equalize the intensities of two spectral bands, decreasing the effect of instrumental polarization originating in the grooves of the grating. The second half-wave plate was installed in front of the slit. During the observations, it sequentially occupied two positions relative to the slit, offset by 0° and 22.5°. In this way, we were able to derive the Stokes parameters Q/I and U/I. The detector

Table 1. Parameters of the spectropolarimetric observations

Slit width	100 micron ≈ 0.5″
Spectral order	II (left)
Spatial resolution	0.175″/pix.
Spectral dispersion	0.013 Å/pix.
Exposure time	0.05 s

Table 2. Observational parameters of EBs

Set	Date	Number of frames	Beginning of observations, UT	Duration	NOAA	Nearby objects
A	July 4, 1999	99	$08^h45^m52^s$	40^m08^s	8614 (N14E47)	Pores
B	July 5, 1999	30	06 10 08	09 49	8611 (S25W35)	Penumbra of the spot
C	July 14, 1999	45	07 10 43	17 51	8627 (S14E06)	Pore
D	Aug. 7, 1999	67	08 30 19	27 01	8656 (N18W33)	

was a TE/CCD-512TK CCD camera produced by Princeton Instruments, Inc.

Due to their small size, the observed properties of Ellerman bombs are very sensitive to the spatial resolution, which varied from 0.5″ to 1.2″, depending on the atmospheric conditions during the observations. To decrease the effect of tremor, all time series were obtained with the minimum exposure possible for the CCD camera. A total of more than 200 time series for the Ellerman bombs were obtained.

To address the problem at hand, our observations of Ellerman bombs had to satisfy two important requirements: that the duration of the time series be comparable with the average lifetime of an Ellerman bomb and that the series have high temporal resolution. Various studies have suggested lifetimes for EBs ranging from several minutes to an hour [1]. Bruzek [2] observed several EBs with lifetimes of several hours. Payne [3] and Nindos and Zirin [6] give average lifetimes of about 14 min. According to the observations of [6], only 6–7% of EBs have lifetimes < 7 min, while 15–17% have lifetimes > 20 min. Thus, if an EB was observed for longer than 7 min, we can assume that the observation spanned the majority of its lifetime. Taking these requirements into account, we selected four of more than 200 time series of observations of EBs made up of from 33 to 99 consecutive frames. Table 1 presents the parameters of the observations and Fig. 1 the observed spectra. The dates of the observations, number of frames in a series, beginning times and durations of the observations (UT), number and coordinates of the groups of selected EBs, and the names of objects observed simultaneously with the EBs are presented in Table 2. All the EBs were observed in actively developing groups. In series B, a pair of Ellerman bombs were observed in a single active region, one of which disappeared 6 min after the beginning of the observations.

3. DATA REDUCTION

After the standard preliminary reduction of the CCD spectra, a cross section of each EB along the dispersion was extracted in both orthogonal strips of the spectrum. The resulting line profile was corrected for the continuum level. Matching the Hα profile with the continuum in each strip appreciably decreased the effect of instrumental polarization [17]. The parameters Q/I and U/I were calculated using the formula $(I_\parallel - I_\perp)/(I_\parallel + I_\perp)$, where $I_\parallel$ and $I_\perp$ are the intensities of the ordinary and extraordinary rays. The intensity I was calculated as $I = (I_\parallel + I_\perp)/2$. Figure 2 presents the line profiles with the corresponding parameters Q/I and U/I along the dispersion for two EBs.

Consecutive observations of Q/I and U/I can be considered quasi-simultaneous, since the time between the exposures was small (< 10 s). In this case, we can calculate the degree of polarization P and the angle χ between the plane of polarization and the slit:

$$P = \sqrt{(Q/I)^2 + (U/I)^2},$$
$$\chi = \frac{1}{2} \times \arctan\left(\frac{U/I}{Q/I}\right).$$

In this way, P and χ were calculated for the "quasi-times" of the observations, i.e., for average times between the times at which Q/I and U/I were obtained.

For each series of observations, the angle γ_0 between the direction toward the center of the solar disk and the spectral slit was acquired. We used γ_0 to determine the angle γ—the azimuth of the polarization plane relative to the direction toward the center of the solar disk. The rms error of the relative intensity in the spectral region studied did not exceed 0.008. The accuracy of the EB measurements was shown to be the same. The rms errors in the degree of polarization P and the angle χ (and, hence, in γ) did not exceed 0.8% and 2°, respectively. We can see from Fig. 2 that the Stokes parameters in the quiescent region are close to zero in the entire observed spectral interval, indicating that the instrumental polarization did not exceed the measurement errors. According to the results of previous observations [17, 20] and theoretical calculations [11, 22, 23], this accuracy is sufficient for deriving evidence for impact linear polarization in

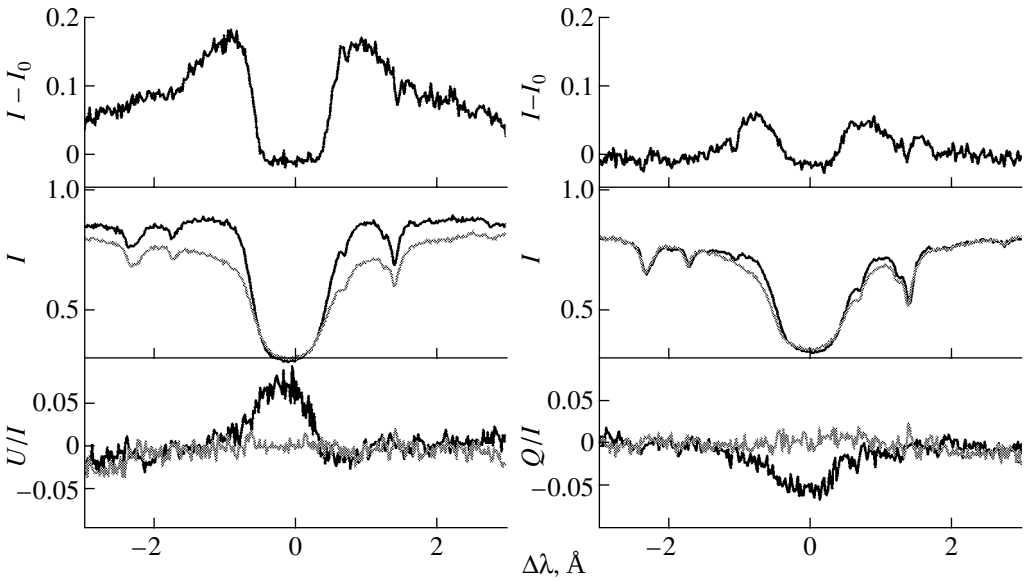

Fig. 2. Variations along the dispersion for the Stokes parameters, the relative intensity, and the difference between the intensities in a quiet region and an Ellerman bomb. In middle and lower panels, the grey curve corresponds to the quiet region and the black curve to the Ellerman bomb.

EBs. Thus, this procedure can be used to study linear polarization in EBs.

4. RESULTS

The profile intensities, Stokes parameters Q/I and U/I, and the degree of polarization and azimuth of the polarization plane were obtained for five EBs. To study temporal variations in the brightness of the EBs, we used the difference of the intensity in the EB and in the quiescent region $I - I_0$ for the red and blue wings. The Stokes parameters Q and U for each time were determined at the line center, since, in all cases, polarization was detected only at the center of the Hα line. Figure 3 presents the time dependences of the degree of polarization and azimuth of the polarization plane for each EB. The results of the simultaneous observations of the two EBs in series B are presented in one graph.

The high-time-resolution data made it possible to follow variations of the intensity in the wings of the EBs. The observed profiles were asymmetrical for essentially all five EBs. The asymmetry was maintained during the entire lifetime of the EB in series D, where the blue wing was brighter, and in series A, where the red wing was slightly brighter than the blue wing. An asymmetry toward the blue is also noted for both EBs in series B at the beginning of the observations; however, the red wing becomes brighter at the end of the observations. A similar pattern was also observed for the EB in series C: in the first minutes of the observations, an asymmetry toward the red was noted, which then shifted to the blue side, with the red wing becoming brighter again approximately 8 min later. We can see from Fig. 3 that there is no apparent relationship between the asymmetry of the Hα intensity profiles in the EBs and their degree of polarization or the azimuth of the polarization plane.

In two series (A and D), there were objects along the line of sight that were projected onto the EBs. The Hα line in these objects was in absorption and was bent in the form of an arch with radial velocities from -30 to $+50$ km/s, with the matter above the Ellerman bomb moving upwards. At the initial observation times in series B, the centers of the Hα lines in both EBs shifted toward the red with a velocity of about 30 km/s, which does not coincide with the velocity of about 8 km/s for the upward motion of matter observed in most EBs [4].

The highest degree of polarization was about 10%, detected for the EB in series D; the maximum polarizations in the EBs in series A and C were 6–7%. As a rule, the maximum polarization for all the EBs was detected at the beginning of the observation. During most of the EB's lifetime, the degree of polarization was 2–5%, consistent with both the observations of Firstova [17] and the results of Rust and Keil [18]. Note that, in the close pair of EBs in series B, the brighter EB displays a lower degree of polarization than the weaker EB; a similar effect was described by Babin and Koval [13].

For all the EBs, the azimuth of the polarization plane when the degree of polarization was maximum was close to 60°–70°.

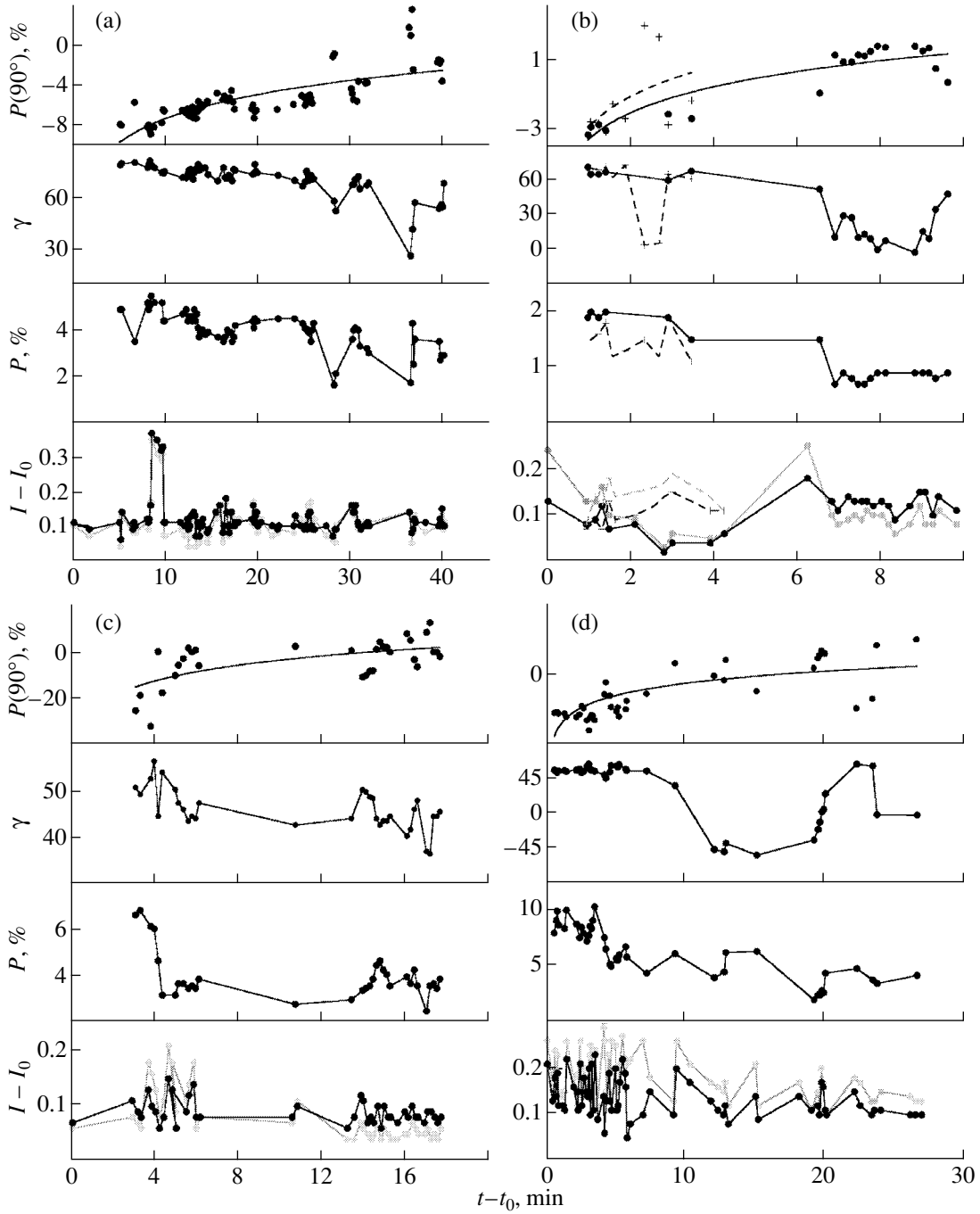

Fig. 3. Temporal variations of the parameters of the EBs observed on (a) July 4, 1999 (series A), (b) July 5, 1999 (series B), (c) July 4, 1999 (series C), and (d) August 7, 1999 (series D). From bottom to top, the plots show the differences of the intensity in the red (black curve) and blue (grey curve) wings of the Hα line, the degree of polarization P, the azimuth of the polarization plane γ, and the variations of the parameter $\mathbf{P}(90°)$ for all four time series. All parameters for the two EBs observed simultaneously are presented in the graph for July 5, 1999; the pluses and dashed curve correspond to the first EB, and the dots and solid curve, to the second EB.

All the Ellerman bombs displayed a rotation of the polarization plane during their lifetimes. This effect was noted before by Firstova [17] and Babin and Koval' [15]. Figure 3 presents a larger amount of observational material demonstrating this effect, confirming its reality.

A comparison between the data and theoretical calculations for impact polarization [11, 22] suggest that the most likely explanation for the observed linear

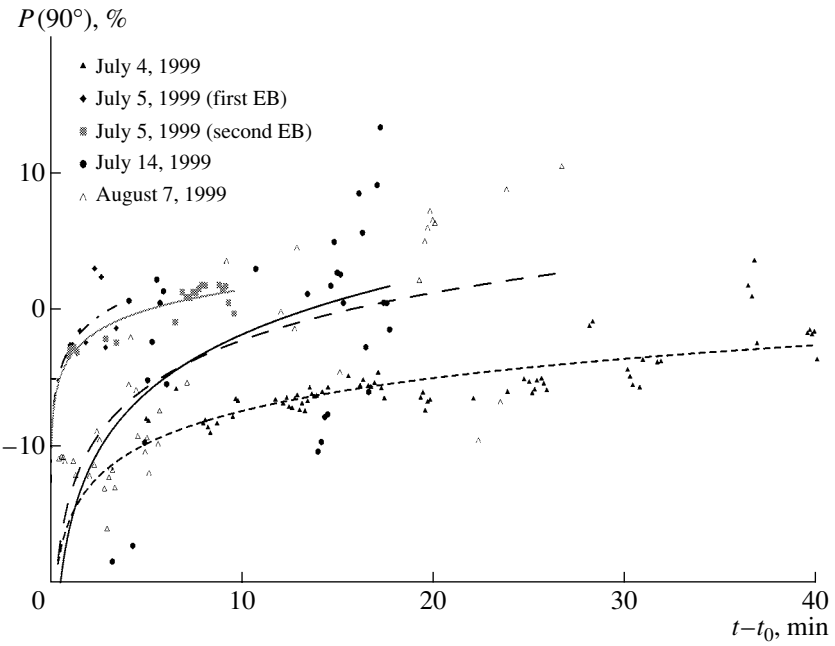

Fig. 4. Time variations of the parameter $\mathbf{P}(90°)$ for all the observed EBs.

polarization is impact polarization due to beams of energetic particles. The main evidence for this is the presence of polarization in the core of the Hα line and the depolarization of the wings (Fig. 2). Based on this idea, we suggest a method for comparing polarization data for solar objects obtained at different distances from the center of the solar disk.

Knowing the angle γ and the degree of polarization P, we can determine the projection of the polarization vector onto the direction from the EB to the disk center by calculating the parameter

$$Q_\circ(\theta) = P\cos 2\gamma.$$

Further, knowing the angle θ between the radius vector of the Sun and the line of sight, or the direction of the motion of the radiated photon, we can calculate the polarization observed at right angles to the incident beam using the formula [24]

$$\mathbf{P}(90°) = Q_\circ(\theta)/(Q_\circ(\theta)\cos^2\theta + \sin^2\theta).$$

This is essentially the polarization that can be observed if the object is at the limb and the beam falls vertically from the corona. According to the theory of impact polarization, this is the maximum polarization that can be detected. Although these transformations are somewhat artificial, they make it possible to compare the polarimetric parameters of EBs located at different distances from the center of the disk with both those of other EBs and with theoretical calculations. Figure 3 presents the time dependences of $\mathbf{P}(90°)$ for all four EB series.

5. DISCUSSION AND CONCLUSIONS

Our observations of five Ellerman bombs did not reveal any relationship between the intensity, degree of polarization, and azimuth of the polarization plane. This may provide indirect evidence that the EBs originate due to the bombardment of the chromosphere by energetic particle beams. For example, it was shown in [25] based on the example of protons that, in the process of the bombardment, the Hα line intensity increases simultaneously with the density of the background protons and electrons, resulting in partial depolarization.

According to our data, the azimuth of the polarization plane was about 60°–70° in the first minutes of the EBs' lifetimes. As was shown in [22], the orientation of the azimuth of the polarization plane close to the tangential direction corresponds to the bombardment of the chromosphere by an electron beam. Thus, our results suggest that the beams that excited the observed EBs consisted primarily of electrons.

The time dependence of $\mathbf{P}(90°)$ for all the EBs indicates that it varies from negative to positive values. According to [22, 23], negative values correspond to higher energy particles than positive values (the sign changes for energies near 200 KeV). Comparing the resulting dependences for $\mathbf{P}(90°)$ for all the EBs, we see that the values for this parameter at the initial times vary from −3% to 20% (Fig. 3). The best fit for the time dependences for $\mathbf{P}(90°)$ is given by a natural logarithmic function. These functions were extrapolated for the initial time of the observations for

all the EBs (Fig. 4), when $\mathbf{P}(90°)$ can be estimated to be 15–20%. When the results of theoretical calculations and laboratory experiments presented in [22] are applied to the $\mathbf{P}(90°)$ values obtained, the energy of the electron beam can be estimated to be several hundreds of keV and appears to decrease with time.

Comparing the time dependences for all five cases (Fig. 4), we see that the energy of all the EBs decreases dramatically within the first 5 min, after which the variations become smoother. However, the shapes of the different curves are somewhat different. The smoothest variation is observed in series A, which is the longest-lived. The steepest increase is seen in series B. Of the two EBs in series B, the first to die out was the one whose curve increased more steeply. It is quite possible that the velocity and the type of variation of the polarization and, accordingly, of the particle energy, affects the lifetime of the EB: the smoother the variations, the longer the lifetime. Note also that the shortest lifetime was observed for an EB located near the penumbra of a large spot.

In conclusion, although our proposed interpretation requires magnetic-field reconnection and therefore cannot be unconditionally adopted as an explanation for the origin of all Ellerman bombs, our results provide evidence that at least some EBs may be the result of impact polarization. Spectropolarimetric observations can be used to identify EBs of this type and to study the processes occurring in them.

6. ACKNOWLEDGMENTS

The author thanks N.M. Firstova for assistance in the observations and useful discussions. This work was supported by the Russian Foundation for Basic Research (project nos. 00-02-16068 and 02-02-06211), the Program for State Support of Leading Scientific Schools (grant 00-15-96659), and the State Science and Technology Project in Astronomy.

REFERENCES

1. A. B. Severny, *The Solar Spectrum,* Ed. by C. de Jager (Reidel, Dordrecht, 1965), p. 21.
2. A. Bruzek, Sol. Phys. **26**, 94 (1972).
3. T. E. W. Payne, in *American Astronomical Society Meeting, 1993,* Vol. 183, 68.01.
4. H. Kurokawa, I. Kawaguchi, Y. Funakoshi, and Y. Nakai, Sol. Phys. **79**, 77 (1982).
5. A. N. Koval', Izv. Krym. Astrofiz. Obs. **44**, 94 (1972).
6. A. Nindos and H. Zirin, Sol. Phys. **182**, 381 (1998).
7. D. A. Diver, J. C. Brown, and D. M. Rust, Sol. Phys. **168**, 105 (1996).
8. J. Qiu, M. D. Ding, H. Wang, *et al.*, Astrophys. J. **544**, L157 (2000).
9. M. D. Ding, J. C. Hénoux, and C. Fang, Astron. Astrophys. **332**, 761 (1998).
10. J. C. Hénoux, C. Fang, and M. D. Ding, Astron. Astrophys. **337**, 294 (1998).
11. V. V. Zharkova and D. V. Syniavskii, Astron. Astrophys. **354**, 714 (2000).
12. A. N. Babin and A. N. Koval', Izv. Krym. Astrofiz. Obs. **73**, 3 (1985).
13. A. N. Babin and A. N. Koval, Sol. Phys. **98**, 159 (1985).
14. A. N. Babin and A. N. Koval', Izv. Krym. Astrofiz. Obs. **75**, 52 (1986).
15. A. N. Babin and A. N. Koval', Izv. Krym. Astrofiz. Obs. **77**, 9 (1987).
16. A. N. Babin and A. N. Koval', Izv. Krym. Astrofiz. Obs. **80**, 110 (1988).
17. N. M. Firstova, Sol. Phys. **103**, 11 (1986).
18. D. M. Rust and S. L. Keil, Sol. Phys. **140**, 55 (1992).
19. S. A. Kazantsev, N. M. Firstova, L. K. Kashapova, *et al.*, Astron. Zh. **75**, 792 (1998) [Astron. Rep. **42**, 702 (1998)].
20. N. M. Firstova, A. V. Boulatov, and L. K. Kashapova, in *Solar Polarization,* Ed. by K. N. Nagendera and J. O. Stenflo (Kluwer, Dordrecht, 1999), p. 451.
21. V. I. Skomorovsky and N. M. Firstova, Sol. Phys. **163**, 209 (1996).
22. J. C. Hénoux and G. Chambe, J. Quant. Spectrosc. Radiat. Transf. **44**, 193 (1990).
23. L. Fletcher and J. C. Brown, Astron. Astrophys. **294**, 260 (1995).
24. J. C. Hénoux, D. Heristchi, G. Chambe, *et al.*, Astron. Astrophys. **119**, 233 (1983).
25. E. Vogt, S. Sahal-Brechot, and J.-C. Hénoux, Astron. Astrophys. **324**, 1211 (1997).

Translated by K. Maslennikov

Astronomy Reports, Vol. 46, No. 11, 2002, pp. 925–931. Translated from Astronomicheskiĭ Zhurnal, Vol. 79, No. 11, 2002, pp. 1027–1033.

The Effect of Acoustic Waves on Spectral-Line Profiles in the Solar Atmosphere: Observations and Theory

R. I. Kostyk* **and E. V. Khomenko**

Main Astronomical Observatory, National Academy of Sciences of Ukraine, ul. Zabolotnogo 27, Kiev, 03680 GSP Ukraine

Received February 11, 2002; in final form, May 23, 2002

Abstract—The fine structure of the FeI λ 532.4185-nm line of neutral iron is studied with high spatial (0.5″) and temporal (9.3 s) resolution using observations of a quiet region at the center of the solar disk. The character of the line asymmetry depends strongly on the nature of the velocity field, i.e., on whether it is due to convective or wave motions. The magnitude of the asymmetry due to acoustic waves is comparable to that due to convective motions. The propagation of acoustic waves in moving granules and intergranular lanes is studied by solving a system of hydrodynamical equations in a three-dimensional model for the solar atmosphere. The temporal variations in the bisector of the line synthesized in a non-LTE approximation agree well with the observational data. © *2002 MAIK "Nauka/Interperiodica".*

1. INTRODUCTION

The idea that nonthermal broadening of spectral lines, including line asymmetries, could be interpreted as an effect of acoustic waves was expressed as early as 1948 by Bierman [1]. However, the profile of the absorption coefficient for the uniform medium in which the acoustic waves propagated was calculated only 20 years later, by Eriksen and Maltby [2] and Babiĭ and Al'tman [3]. They considered the case when the velocity of the absorbing particles, gas pressure, and temperature vary in phase; i.e., the acoustic wave propagation was assumed to be adiabatic. Later, after taking into account radiation damping when calculating the profiles of spectral lines in the solar atmosphere, Teplitskaja [4] and Kostik and Orlova [5] concluded that the wave motions result in only a small asymmetry of the absorption lines compared to the observed lines. However, in our view, the comparison of the results of the numerical modeling with the observations was not carried out entirely correctly, since the observed line asymmetries could be due to both waves and convective motions. This same drawback is inherent in numerous subsequent studies concerning the asymmetries of Fraunhofer lines, especially those based on observations with high spatial and temporal resolution. Only Hanslmeier *et al.* [6, 7] have presented the average bisectors of lines observed in granules and intergranular lanes filtered from the wave motions, enabling them to show that the waves in intergranular lanes affect the line bisector shape more strongly. Unfortunately, Hanslmeier *et al.* [6, 7] turned their attention primarily to convective motions, whereas the line bisectors due to wave motions were not studied in detail.

The aim of the present work is to study the effect of a propagating wave on the line bisectors and to compare this effect with the influence of convective motions. The observational data will be compared with the results of numerical modeling, and, in contrast to previous studies, the wave propagation in a moving medium will be considered.

2. OBSERVATIONAL RESULTS

The observations were carried out by N. Shchukina in August 1996 on the 70-cm German vacuum tower telescope (VTT), installed at the Observatorio del Teide of the Instituto de Astrofisica de Canarias (Tenerife). The design of the telescope is described in detail by Schröter *et al.* [8]. The FeI λ 532.4185-nm line of neutral iron was observed. The spectral studies were conducted near the solar-disk center outside of active regions, and were accompanied by video recordings in the Hα hydrogen line and K CaII ionized-calcium line. The detector was a CCD camera composed of 1024 × 1024 pixels (2 × 2 cm) joined in pairs. The size of the spectral region detected by this array is 0.2 nm near a wavelength of 600 nm. The size of a double pixel corresponds to 0.174″ at the solar surface. The width of the entrance slit of the spectrograph was 80 μm, or 0.38″ at the solar disk. Therefore, the field of view of the telescope was 0.38″ × 89″. The line was measured for 31 min in intervals of about 9.3 s. The jitter of the solar surface

*E-mail:kostik@mao.kiev.ua

1063-7729/02/4611-0925$22.00 © 2002 MAIK "Nauka/Interperiodica"

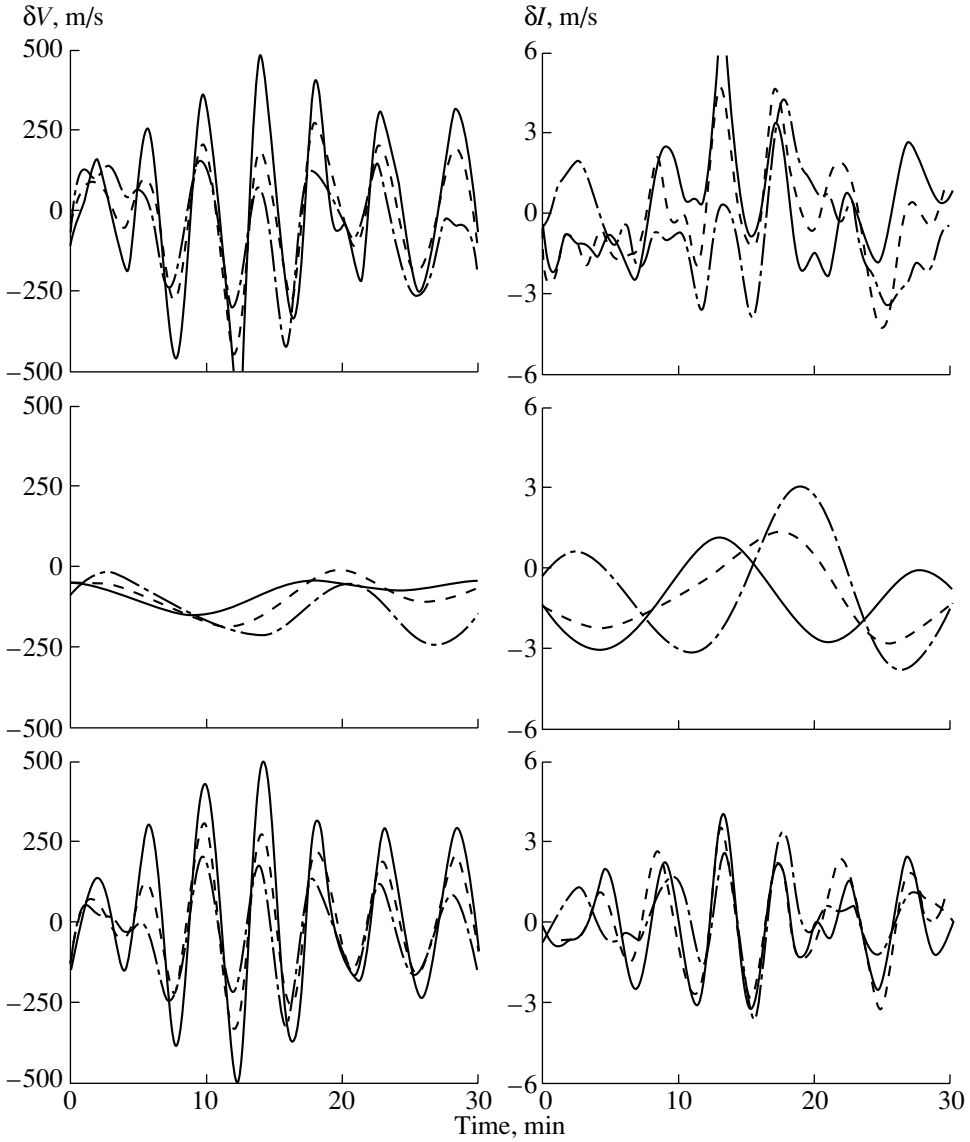

Fig. 1. Time variations in the velocity (left) and intensity (right) of the FeI λ 532.4185-nm line for a fixed position on the solar disk. The solid curve corresponds to $H = 500$ km, the dashed curve to $H = 300$ km, and the dot–dash curve to $H = 10$ km. The observational data are presented in the top panels, the convective components of the intensity and velocity in the central panels, and the wave components in the bottom panels.

at the spectrograph entrance slit during the observations was less than $0.35''$.

The FeI λ 532.4185-nm line is strong. Its central residual intensity in the spectrum of the atmosphere of the quiet solar-disk center relative to the local continuum is $r = 0.139$. The calculations of Shchukina and Trujillo Bueno [9], which take into account deviations from local thermodynamic equilibrium, indicate that the region of formation of this line covers heights from $H = 10$ km (the continuum) to $H = 500$ km (the central intensity). Thus, the emission at the center of this line is formed near the temperature minimum, where considerable variations in brightness and velocity due to wave motions are expected.

Following the standard procedure, all 200 images of this line were corrected for the dark current, changes in the Earth's atmospheric transparency in the course of the observations, and variable sensitivities of individual pixels.

Variations in the intensity $\delta I_k(i,j)$ and velocity $\delta V_k(i,j)$ with respect to their mean values were measured for each individual image ($j = 1$–200), each spectral track ($i = 1$–512), and several levels of the line profile ($k = 1$–11, which correspond to 11 different heights in the solar atmosphere from 10 to 500 km). The spatial and temporal variations in these parameters are due to both convective and wave motions. To separate these components of the intensity

and velocity fields, we constructed a k–ω diagnostic diagram, in which power is presented as a function of the temporal (ω) and spatial (k) frequencies. In accordance with this diagram, we restricted wave motions to the temporal frequencies $\omega = 1.8$–5.7 mHz and convective motions to frequencies below 2.2 mHz. In terms of the spatial frequencies, the division between wave and convective motions was at $k = 0.18$. The reduction of the observations and the (k–ω) diagnostic diagram are presented in more detail in our previous papers [10, 11].

Examples of temporal variations in the velocity and intensity of the FeI λ 532.4185-nm line at one position on the solar disk ($i = 97$) are shown in the left and right columns of Fig. 1. The solid curve corresponds to a height of $H = 500$ km ($k = 1$); the dashed curve, to $H = 300$ km ($k = 5$); and the dot–dash curve, to $H = 10$ km ($k = 11$). The observed dependences are shown in the two top panels, while the convective and wave components of the intensity and velocity are shown in the middle and bottom panels, respectively. The amplitude of the wave component of the velocity increases with height, while this tendency is less evident for the intensity.

Using the data of Fig. 1, we drew bisectors of the lines, presented in Fig. 2. The curves correspond to various times. The data before separation into components are shown in the top panel, and the bisectors due only to convective and wave motions are shown in the middle and bottom panels, respectively. The line bisectors are drawn with intervals of 9.3 s. The shifts for different levels of the line profile were measured with respect to their mean shift at $k = 1$, i.e., relative to the central intensity. The difference between the line-bisector variations before separating the velocity field into components and the variations due only to convective motions is very clear. The scatter of the shifts in the latter case is considerably less. As expected, the scatter of the shifts due to convective motions decreases from the wings to the core of the line, since the speed of the convective motion decreases with height in the solar atmosphere. The characteristic behavior of the line bisectors due only to acoustic waves (Fig. 2c) differs considerably from that in Fig. 2b: shifts in the line core are almost twice as large as in the wings, in accordance with the increase in the amplitude of the wave motions with increasing height in the solar atmosphere. Thus, the effect of the wave motions on the bisector shape turns out to be appreciable and cannot be ignored in observations with high spatial and temporal resolution.

Figure 3a presents the shifts of the center of the FeI λ 532.4185-nm line ($H = 500$ km, $k = 1$) due to convective motions, averaged over all spectral tracks ($i = 1$–512) and the entire observation time ($j = 1$–200), as functions of the intensity in the continuum

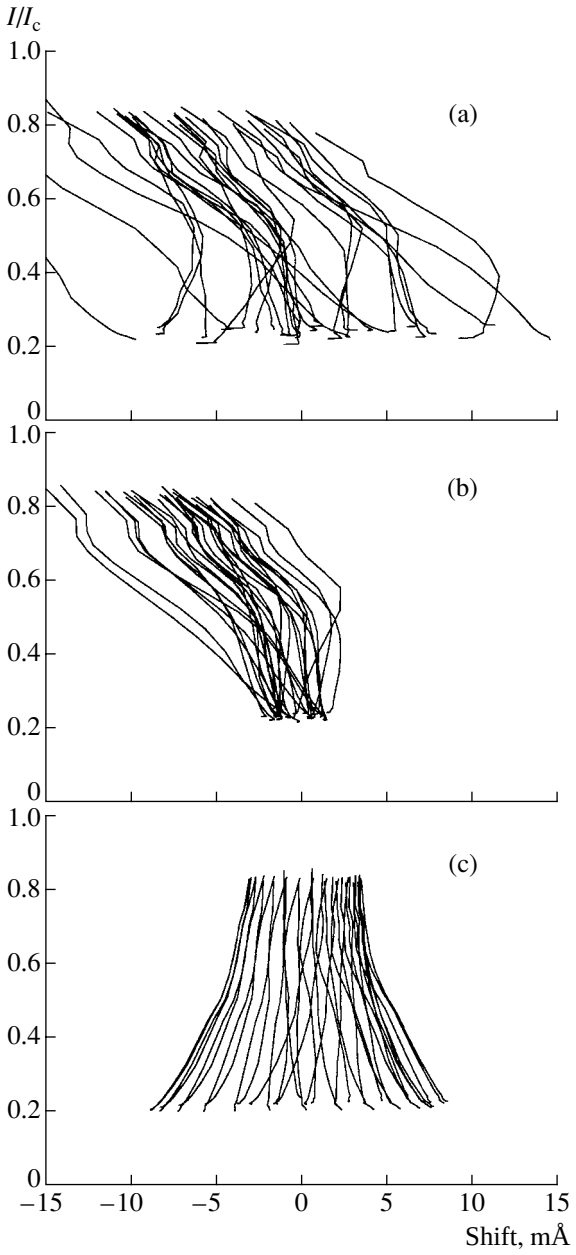

Fig. 2. Bisectors of the FeI λ 532.4185-nm line for various times: (a) data before separation into convective and wave components; (b) bisectors due only to convective motions; (c) bisectors due only to wave motions.

($k = 11$). We can see that the central intensity above granules is shifted toward the violet, and the central intensity above intergranular lanes shifted toward the red. The greater the contrast of the granule (or intergranular lane) in the continuum, the larger the shift at height $H = 500$ km. Thus, even in the region of the temperature minimum, the field of the convective motion is not disrupted: material rises above the granules and descends between them. The velocity of descending turbulent elements at $H = 500$ km

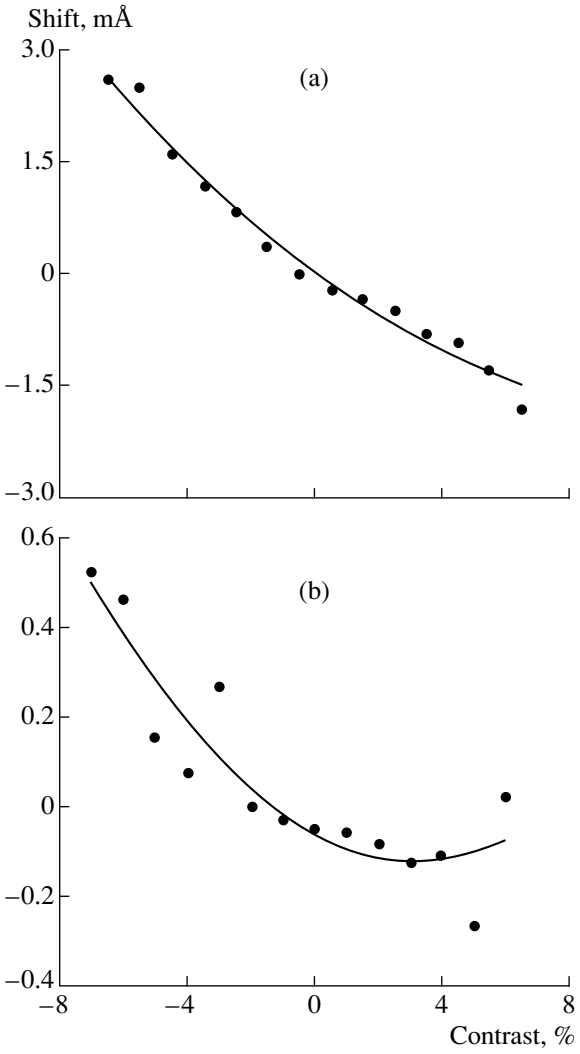

Fig. 3. Shifts of the center of the FeI λ 532.4185-nm line in the solar atmosphere at height $H = 500$ km averaged over time (31 min) and space ($0.38'' \times 89''$) due (a) only to convective motions and (b) only to wave motions as functions of the intensity in the continuum ($H = 10$ km).

is, on average, greater than the velocity of rising elements, as is the case at the level of formation of the continuum. In the case of the wave motions, the shifts of the line center averaged over space and time are not equal to zero, as would be expected based on general considerations, and depend weakly (within the errors) on the continuum intensity (Fig. 3b), with the shifts being greater above the dark intergranular lanes than above bright granules. This is a consequence of the different characters of the propagation of acoustic waves over granules and intergranular lanes found in our previous work [11]. First, the amplitudes of oscillatory motions are greater above intergranular lanes than above the granules, and second, waves above granules are approximately standing waves.

3. MODELING THE OSCILLATIONS

We shall not discuss line asymmetries due to convective motions here. Both two-dimensional [12, 13] and three-dimensional [14, 15] hydrodynamical models of the solar granulation can describe these motions quite satisfactorily. Our aim is to consider wave propagation in the corresponding models, to calculate the profile of the FeI λ532.4185-nm line, and to compare the calculated asymmetry with the observational data.

The hydrodynamical equations of conservation of momentum, mass, and energy can be written

$$\rho\frac{d\mathbf{V}}{dt} = -\boldsymbol{\nabla}P + \mathbf{g}\rho, \tag{1}$$

$$\frac{\partial\rho}{\partial t} = -\boldsymbol{\nabla}(\rho\mathbf{V}), \tag{2}$$

$$\frac{dQ}{dt} = c_v\frac{dT}{dt} - \frac{RT}{\rho}\frac{d\rho}{dt}, \tag{3}$$

where the usual notation has been used. In addition, we have assumed that the atmosphere is vertically stratified and uniform in the horizontal direction; there is no magnetic field; and the effects of viscosity, heat transfer, and rotation can be neglected.

Let us calculate the temperature and density distributions and the velocity variations in the solar atmosphere due to wave motions under the following assumptions: the waves propagate only in the vertical (z) direction, deviations from adiabatic wave propagation are due to radiative damping, and the equation of state has the form

$$\frac{T_1}{T_0} = \frac{P_1}{P_0} - \frac{\rho_1}{\rho_0}. \tag{4}$$

To solve the above system of differential equations, we will separate the entire photosphere into a series of isothermal layers moving with constant velocities. The equations will be linearized in each layer, assuming that the velocity is composed of a convective component V_0 (which is constant in time) and a perturbation produced by the wave:

$$T = T_0 + T_1, \quad P = P_0 + P_1, \qquad \rho = \rho_0 + \rho_1, \quad V = V_0 + V_1. \tag{5}$$

Substituting (5) into (1)–(3) and neglecting second-order terms in the perturbations, we obtain the system of dimensionless equations

$$\frac{\partial W_1}{\partial t} + W_0\frac{\partial W_1}{\partial z} = -\frac{\partial}{\partial z}(R + \Theta) + 2\Theta, \tag{6}$$

$$\frac{\partial R}{\partial t} + W_0\frac{\partial R}{\partial z} = 2W_0R - \frac{\partial W_1}{\partial z} + 2W_1, \tag{7}$$

$$\frac{\partial\Theta}{\partial t} + W_0\frac{\partial\Theta}{\partial z} = -\frac{1}{\tau_r}\Theta - (\gamma - 1)\frac{\partial W_1}{\partial z}. \tag{8}$$

The vertical velocity of the particle oscillations W is measured in (6)–(8) in units of the isothermal sound speed ($W_{0,1} = V_{0,1}/C_s$); the distance z, in units of twice the pressure scale height. The values of Θ and R are $\Theta = T_1/T_0$ and $R = \rho_1/\rho_0$, and τ_r is the characteristic relaxation time for thermal inhomogeneities [16]. We will seek a solution of the system of equations (6)–(8) in the form

$$W_1, \Theta, R \sim e^{z(1-k_i)} e^{-ik_r(t\,V_{ph} - t\,W_0 - z)}, \qquad (9)$$

where $V_{ph} = \omega/k_r$ is the phase velocity of the wave and k_r and k_i are the real and imaginary parts of the vertical wavenumber k_z. As a result, the system of differential equations (6)–(8) will be reduced to a system of algebraic equations for k_z. The accuracy of the approximate method described above was tested by Mihalas and Toomre [17] for the particular case when the exact solution is known. It was shown that the resulting $k_z(z)$ agrees well with the exact dependence if the temperature gradient is linear and the oscillations are adiabatic.

Substituting (9) into (6)–(8) and using (4), we find the speed of the particle oscillations in the vertical direction W_1 and the temperature and density fluctuations due to the wave:

$$W_1 = V_{0W} e^{z(1-k_i)} \sin((\omega - W_0 k_r)\, t - k_r z), \quad (10)$$

$$T_1/T_0 = |\Theta|\ e^{z(1-k_i)} \times \sin((\omega - W_0 k_r)\, t - k_r\, z + \varphi_{TV}), \qquad (11)$$

$$\rho_1/\rho_0 = |R|\, e^{z(1-k_i)} \times \sin((\omega - W_0 k_r)\, t - k_r\, z + \varphi_{\rho V}). \qquad (12)$$

The expression φ_{TV} in (11) denotes the phase shift between oscillations of the temperature and velocity; and the expression $\varphi_{\rho V}$ in (12), the phase shift between oscillations of the density and velocity. The corresponding expressions are very cumbersome, and we do not present them here.

Recall that the solution of (6)–(9) for $V_0 = \text{const}$ (i.e., when the convective velocity is not taken into account) was first derived by Noyes and Leighton [18] (see also [19–22]).

We introduced the variations in velocity, temperature, and density described by (10)–(12) into the three-dimensional hydrodynamical model for the solar atmosphere of [15], kindly provided by M. Asplund. The simulated region of the solar surface covers $6.0 \times 6.0 \times 3.8$ Mm with a spatial resolution of $30 \times 30 \times 46$ km. The variations in the thermodynamic parameters were taken for a single time. We arbitrarily chose one horizontal cross section containing five granules and five intergranular lanes for our subsequent computations. Further, this two-dimensional model was transformed into 50 one-dimensional models for the granules and intergranular lanes with various contrasts. We obtained mean models for a granule and intergranular lane by averaging these models. Finally, we used (10)–(12) to calculate the temporal variations in the thermodynamic quantities (over 31 min) for each of these two one-dimensional models and for the standard spatially-averaged model MACKKL [23]. The temporal step was 9.3 s, as in the actual observations. Oscillations for eight different frequencies in the range 2–5.5 mHz were computed. These frequencies were chosen in accordance with the spectral resolution of the observational time series, whose duration was 31 min. The initial velocity and phase of the oscillations at height $H = 10$ km over the continuum level were taken from the observations for the corresponding frequencies. Finally, we calculated the profile of the observed FeI λ 532.4185-nm line for each model and each time (a total of 200 combinations). Since the core of this line is formed at a large height in the solar atmosphere, deviations from local thermodynamic equilibrium had to be taken into account [24]. We used the NATAJA software package, kindly provided by N. Shchukina. This software includes a realistic model for the iron atom (containing 250 levels and 500 radiative transitions) [25] and is based on efficient iterative numerical methods for solving the equations of multilevel transfer in multidimensional media [26].

The bisectors of the spectral line synthesized using this method are presented in Fig. 4 for various times. These bisectors were calculated with respect to those for unperturbed models. The wave component of the observed bisectors is reproduced in Fig. 4a. The bisectors for the mean granule model are shown in Fig. 4b, for the mean intergranular-lane model in Fig. 4c, and for the MACKKL model in Fig. 4d. There are some differences in the behavior of the bisectors for these three models. First, the bisector curve in the granule model is smoother, whereas there is a sharp increase in the scatter of the bisectors at small intensities in the intergranular-lane model. Second, the average scatter is slightly greater in the intergranular-lane model due to the larger amplitudes of the oscillations in intergranular lanes. The observed values of the bisectors were drawn for a fixed track with a duration of 31 min. Since the mean lifetime of a granule is ~8 min, they cannot correspond to oscillations above a granule or intergranular lane. On the whole, there is satisfactory agreement with the modeling results: the asymmetry of the observed and synthesized line profiles depends on time and increases from the line wing to its core, while the scatter of the shifts of the line center is within ± 10 mÅ in both cases.

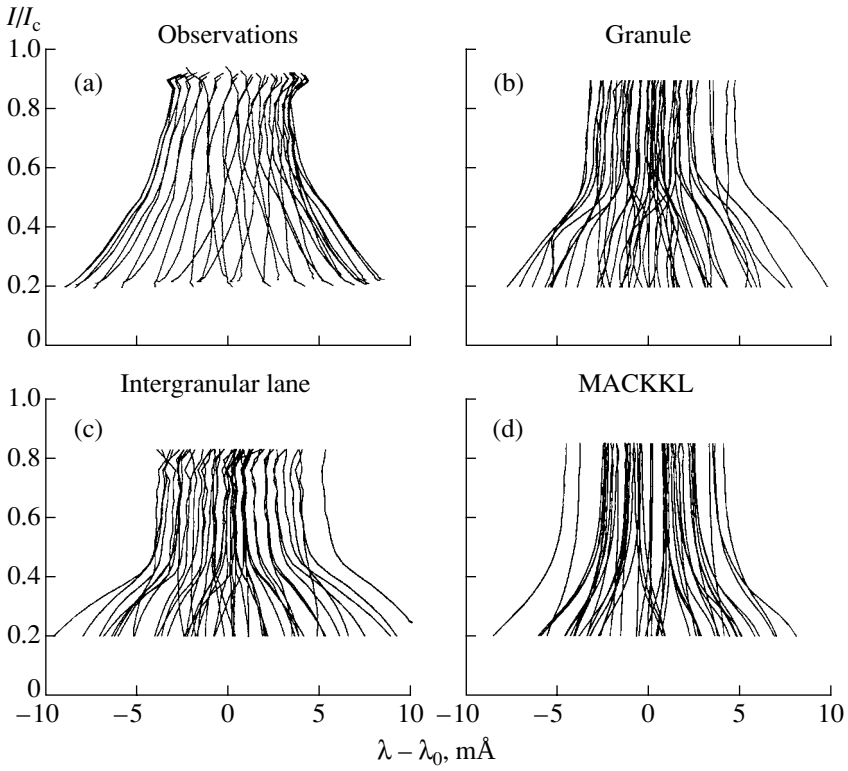

Fig. 4. Bisectors of the FeI λ 532.4185-nm line as (a) observed and calculated for (b) a granule, (c) an intergranular lane, and (d) the spatially averaged solar surface at various times.

Thus, acoustic waves appreciably deform the line profiles. In observations with high spatial and temporal resolution, the magnitude of the asymmetry due to acoustic waves is comparable to that due to convective motions.

4. CONCLUSION

We have studied the fine structure of the FeI λ 532.4185-nm neutral-iron line using observations of the quiet solar-disk center with high spatial and temporal resolution. The character of asymmetries in the line profile depends strongly on their origin: whether they are produced by convective or wave motions. The central intensity of this line (which is formed at a height of $H = 500$ km above the level of formation of the continuum in the solar atmosphere) is shifted toward the violet above granules and toward the red above intergranular lanes. In other words, the convective motions penetrate high into the atmosphere, all the way to the temperature minimum.

We investigated the propagation of acoustic waves in moving granules and intergranular lanes by solving a system of hydrodynamical equations and using a three-dimensional model for the solar atmosphere. The profile of the FeI λ 532.4185-nm neutral-iron line was synthesized using a non-LTE approximation. The character of the time variations in the bisector of the synthesized line is in good agreement with the observational data.

ACKNOWLEDGMENTS

This work was partially supported by the Ukrainian Foundation for Basic Research (project no. 02.07/00044), as well as by NATO grant PST.CLG 975012 and INTAS grant 00-00084. We are grateful to M. Asplund for providing the three-dimensional model of the solar atmosphere, N. Shchukina for access to the NATAJA software package, and R. Rutten for hospitality and fruitful discussions during our visit to the Utrecht Astronomical Institute (The Netherlands).

REFERENCES

1. L. Bierman, Z. Astrophys. **25**, 161 (1948).
2. G. Eriksen and P. Maltby, Astrophys. J. **148**, 833 (1967).
3. B. T. Babiĭ and A. D. Al'tman, Soln. Dannye, No. 5, 103 (1969).
4. R. B. Teplitskaja, Sol. Phys. **6**, 18 (1969).
5. R. I. Kostik and T. V. Orlova, Sol. Phys. **36**, 279 (1974).
6. A. Hanslmeier, A. Kučera, J. Rybák, *et al.*, Astron. Astrophys. **356**, 308 (2000).

7. A. Hanslmeier, A. Kučera, J. Rybák, and H. Wöhl, in *The Dynamic Sun,* Ed. by A. Hanslmeier, M. Messerotti, and A. Veronig (Kluwer, Dordrecht, 2001), p. 267.
8. E. H. Schröter, D. Soltau, and E. Wiehr, Vistas Astron. **28**, 519 (1985).
9. N. G. Shchukina and J. Trujillo Bueno, Sol. Phys. **172**, 117 (1997).
10. R. I. Kostyk and N. G. Shchukina, Pis'ma Astron. Zh. **25**, 781 (1999) [Astron. Lett. **25**, 678 (1999)].
11. E. U. Khomenko, R. I. Kostik, and N. G. Shchukina, Astron. Astrophys. **369**, 660 (2001).
12. M. Steffen, H. G. Ludwig, and A. Kruss, Astron. Astrophys. **213**, 371 (1989).
13. A. S. Gadun, Kinematika Fiz. Nebesnykh Tel **11**, 44 (1995).
14. A. Nordlund, *Small-Scale Dynamical Processes in Quiet Stellar Atmospheres,* Ed. by S. L. Keil (Sac. Peak. Observatory, Sunspot, 1984), p. 181.
15. M. Asplund, A. Nordlund, R. Trampedach, *et al.*, Astron. Astrophys. **550**, 970 (2001).
16. E. A. Spiegel, Astrophys. J. **126**, 202 (1957).
17. B. W. Mihalas and J. Toomre, Astrophys. J. **263**, 386 (1982).
18. R. W. Noyes and R. B. Leighton, Astrophys. J. **138**, 631 (1963).
19. B. Shmieder, Sol. Phys. **47**, 435 (1976).
20. C. Marmolino and R. T. Stebbins, Sol. Phys. **124**, 23 (1989).
21. L. Bertello and B. Caccin, Astron. Astrophys. **231**, 509 (1990).
22. C. Marmolino and G. Severino, Astron. Astrophys. **242**, 271 (1991).
23. P. Maltby, E. H. Avrett, M. Carlsson, *et al.*, Astrophys. J. **306**, 284 (1986).
24. N. G. Shchukina and J. Trujillo Bueno, Astrophys. J. **550**, 970 (2001).
25. N. G. Shchukina and J. Trujillo Bueno, Kinematika Fiz. Nebesnykh Tel **14**, 315 (1998).
26. L. H. Auer, P. Fabiani Bendicho, and J. Trujillo Bueno, Astron. Astrophys. **292**, 599 (1994).

Translated by Yu. Dumin

Astronomy Reports, Vol. 46, No. 11, 2002, pp. 932–941. Translated from Astronomicheskiĭ Zhurnal, Vol. 79, No. 11, 2002, pp. 1034–1043.

Triple Encounters in the Linear Three-Body Problem with Equal Masses

V. V. Orlov[1], A. V. Petrova[1], and A. I. Martynova[2]

[1] *St. Petersburg State University, St. Petersburg, Russia*

[2] *St. Petersburg Forestry Academy, St. Petersburg, Russia*

Received December 6, 2001; in final form, May 23, 2002

Abstract—The paper considers triple encounters in the linear three-body problem for the case of equal masses. Triple encounters are described using two parameters: the virial coefficient k and the angle φ such that $\tan\varphi = \dot{r}/\dot{\rho}$, where $\dot{r}$ and $\dot{\rho}$ are the velocities of the "central" body relative to each of the "outer" bodies. The equations of motion are integrated numerically up to one of the following times: the time for a receding body to turn, the time for this body to reach some critical distance, the time for some escape criterion to be fulfilled, or to some critical time. Evolutionary scenarios for the triple system are determined as a function of the initial conditions. The dependences of the ejection length on k and $\dot{\varphi}$ are derived. The initial conditions corresponding to escape form a continuous region with $k > 0.5$. The regions into which the right and left bodies depart alternate and are symmetrical about the lines of triple close encounters ($\varphi = 45°, 225°$). Regions of stable motions in the vicinity of the central periodic orbit of Schubart ($k \simeq 0.206; \varphi = 135°, 315°$) are identified. Linear structures emanate from the peak of the region of stability, which divide the region for the initial conditions into alternating zones with identical evolutionary scenarios. © *2002 MAIK "Nauka/Interperiodica".*

1. INTRODUCTION

The three-body problem is a classical problem of analytical dynamics. Appreciable progress in our understanding of the qualitative behavior of the solutions has been achieved thanks to numerical modeling. For example, using the results of numerical simulations, Szebehely [1] proposed the following classification for the states in the general three-body problem with negative total energy:

(1) simple interaction;

(2) ejection with return;

(3) escape;

(4) stable revolution;

(5) Lagrangian equilibrium solutions;

(6) close encounters and periodic orbits.

Agekyan and Martynova [2] proposed to supplement this classification with another state: (0) triple close encounters. This state occurs when all three bodies are located inside a sphere such that, for any positions inside this sphere, the system components approach more closely than when the conditions for the virial theorem are satisfied. The center of this sphere coincides with the center of mass of the triple system. Numerical simulations have shown that precisely this state can lead to the escape of one of the bodies from the triple system [3–5].

A number of papers have concentrated on studies of triple encounters (see, for example, [5–10] and references therein). These works separate triple encounters into two main types:

—**fly-bys**, when one of the components flies near the center of mass of a transient double formed by the other two bodies;

—**exchanges**, when there is a series of double encounters by the bodies.

Whether or not a escape occurs after a given triple encounter depends strongly on the closeness of the encounter. The closer a triple encounter, the more likely that it will lead to the disruption of the triple system (see, for example, [11]). However, even very close triple encounters do not always lead to escapes. On the other hand, fairly wide triple encounters can sometimes result in escapes [5]. Therefore, the problem of searching for some additional parameters associated with triple encounters that are correlated with the distance of an ejection following a triple encounter is of interest.

In triple systems with equal-mass components, "fly-by" close triple encounters more often lead to escapes than "exchange" encounters [5]. Agekyan and Anosova [8] and Orlov *et al.* [10] considered fly-by triple-encounter states for given sets of encounter parameters and found a region of parameter values corresponding to the escape of the body flying by after the triple encounter.

In the current paper, we consider the linear three-body problem for the case of equal masses, in which

1063-7729/02/4611-0932$22.00

only exchange triple encounters are realized. The linear three-body problem corresponds to the simplest one-dimensional case, when the three bodies always lie along a single line and move along this line. An analytical treatment of the final motions in this problem is presented by Yoshida [12]. Extensive numerical studies of orbit types have been carried out by Hietarinta and Mikkola [13] (see also references therein), who identified regions of initial conditions corresponding to rapid disruption of the triple system, prolonged evolution ending in disruption (so-called resonance scattering), and quasi-periodic motions near resonance. They note the important role of the central Schubart [14] periodic orbit in the formation of the total phase portrait of the system. In this orbit, the central body undergoes successive double close encounters with the outer bodies separated by equal time intervals.

Here, we consider the result of a single exchange triple encounter in the linear three-body problem. In this case, the triple encounter is a series of double close encounters of the central body with each of the outer bodies. This series ends in the ejection or escape of one of these outer bodies.

2. METHOD OF INVESTIGATION

We consider triple encounters in the linear three-body problem for the case of equal masses. We denote the distance between the left outer body and the central body r; and the distance between the right outer body and the central body, ρ. Let the gravitational constant and the masses of the bodies be equal to unity. Then, the equations of motion take the form

$$\ddot{r} = -\frac{2}{r^2} + \frac{1}{\rho^2} - \frac{1}{(r+\rho)^2} \tag{1}$$

and

$$\ddot{\rho} = -\frac{2}{\rho^2} + \frac{1}{r^2} - \frac{1}{(r+\rho)^2}. \tag{2}$$

The system of equations of motion has the total energy

$$\frac{1}{3}(\dot{r}^2 + \dot{r}\dot{\rho} + \dot{\rho}^2) - \frac{r^2 + 3r\rho + \rho^2}{r\rho(r+\rho)} = h\,. \tag{3}$$

For a system with negative total energy, we can adopt $h = -1$ without loss of generality.

In a linear treatment, a triple encounter is a series of successive double encounters of the central body and each of the outer bodies. Therefore, there will inevitably come a time in a "triple encounter" state when the central body passes through the center of mass of the triple system. At this time, we have, by virtue of the equality of the masses of the bodies, $r = \rho$. We will specify initial conditions precisely at this time.

In this case, the problem has two parameters. One is the closeness of the encounter and the second is the relationship between the velocities $\dot{r}$ and $\dot{\rho}$. We adopt the virial coefficient k of the triple system—the ratio of the kinetic energy to the absolute magnitude of the potential energy—as a closeness parameter. According to (3),

$$k = \frac{1}{3}\frac{(\dot{r}^2 + \dot{r}\dot{\rho} + \dot{\rho}^2)[r\rho(r+\rho)]}{r^2 + 3r\rho + \rho^2}. \tag{4}$$

When $h < 0$, the parameter $k \in [0, 1)$. When $k = 0$, the components are stationary at the initial time. In this case, there will be a triple close encounter of the bodies.

As a second parameter characterizing the ratio of the velocities $\dot{r}$ and $\dot{\rho}$, we adopt the quantity φ, such that

$$\tan\varphi = \frac{\dot{r}}{\dot{\rho}}. \tag{5}$$

This parameter lies in the range $\varphi \in [0, 2\pi]$.

The initial distances r and ρ between the components for the chosen initial positions of the bodies depend only on k:

$$r = \rho = \frac{5}{2}(1-k). \tag{6}$$

We express the velocities $\dot{r}$ and $\dot{\rho}$ in terms of k and φ:

$$\dot{r} = q\sin\varphi \tag{7}$$

and

$$\dot{\rho} = q\cos\varphi, \tag{8}$$

where

$$q = \sqrt{\frac{3k}{(1-k)(1+\sin\varphi\cos\varphi)}}. \tag{9}$$

The values of k and φ were varied as follows:

$$k = 0.01(0.01)0.99, \tag{10}$$

$$\varphi = 1^\circ(1^\circ)360^\circ. \tag{11}$$

For each set of initial conditions, the computations were continued either until the ejected outer body turned ($\dot{R} < 0$), where

$$R = \max\left(r + \frac{\rho}{2},\quad \rho + \frac{r}{2}\right), \tag{12}$$

until the condition for escape of the body from the triple system was satisfied, until the critical distance $R_c = 30$ (conditional escape), or until the critical time $t_c = 100$. We used the criterion of Marchal [15] and Yoshida [16] for the escape criterion. In this case, the

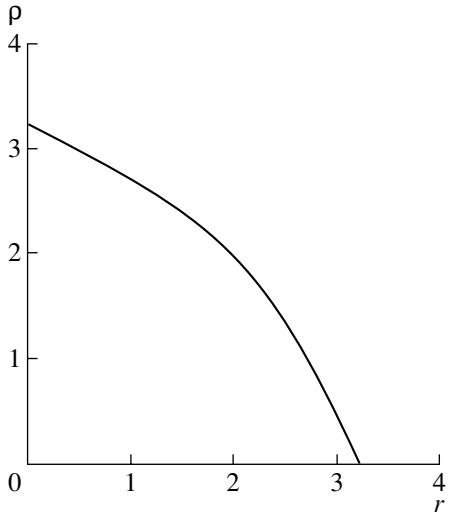

Fig. 1. Periodic Schubart orbit for $k = 0.206$, $\varphi = 135°$.

escape criteria in our notation with $h = -1$ take the form

$$R > \frac{1}{2}, \quad \dot{R} > 0, \quad \dot{R}^2 > \frac{96R}{16R^2 - 1}. \tag{13}$$

We fixed the length of the ejection to be R when the turning criterion was satisfied, and we fixed the energy of the hyperbolic motion for the case of escape to be

$$E = \frac{1}{3}\dot{R}^2 - \frac{2}{R}. \tag{14}$$

We applied a smoothing transform to eliminate singular points arising during the double close encounters in the equations of motion (1) and (2). In addition, we applied elastic recoil in a small vicinity of each double close encounter. The error introduced by this recoil did not exceed the errors associated with one step of integration of the equations of motion.

The numerical integration of the equations of motion was carried out using a fourth-order Runge–Kutta method. The maximum relative error of the energy integral at the end of the computations did not exceed 10^{-4}. The errors in the computed values of R and E did not exceed 10^{-3}.

3. RESULTS

3.1. Triple Close Encounters

We can see from the symmetry of (1) and (2) that, when $\varphi = 45°$ and $225°$, the motion in the (r, ρ) plane is along the line $r = \rho$, and there is a triple close encounter some time after the onset of the evolution. In this case, the equation of motion has the form

$$\ddot{r} = -\frac{5}{4r^2}. \tag{15}$$

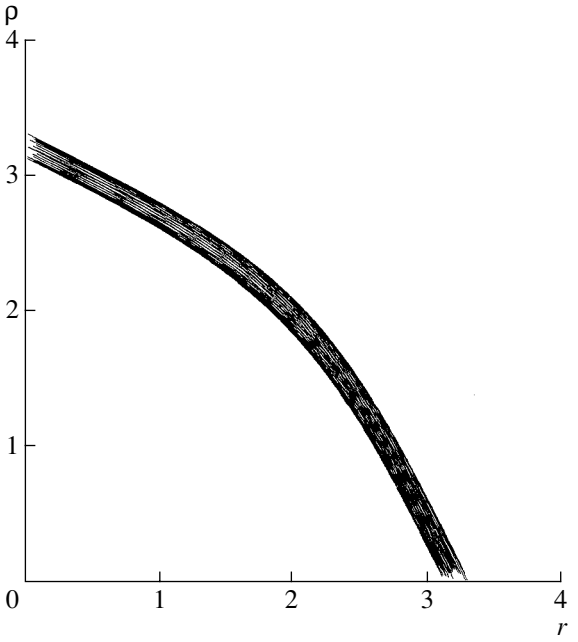

Fig. 2. Nearly periodic stable orbit for $k = 0.18$, $\varphi = 135°$.

The solution of this equation can be written

$$\pm t = -\sqrt{r\left(\frac{5}{2} - r\right)} + \frac{5}{2}\sqrt{k(1-k)} + \frac{5}{4}\left[\arcsin\frac{4r-5}{5} - \arcsin(1-2k)\right]. \tag{16}$$

The evolution ends in a triple close encounter. If $\varphi = 225°$, the triple close encounter occurs at the time

$$t = \frac{5\pi}{8} - \frac{5}{2}\sqrt{k(1-k)} + \frac{5}{4}\arcsin(1-2k). \tag{17}$$

If $k = 0$ and $r_0 = 5/2$, then $t = 5\pi/4$; if $k = 1$ and $r_0 = 0$, then $t = 0$ (the triple system is in a triple-close-encounter state at the initial time). If $\varphi = 45°$, the outer bodies initially separate, reach a maximum distance when $r = 5/2$, and then approach until encounter. The corresponding total time is equal to

$$t = \frac{15\pi}{8} + \frac{5}{2}\sqrt{k(1-k)} - \frac{5}{4}\arcsin(1-2k). \tag{18}$$

3.2. Stable Orbits

The central, stable periodic orbit of Schubart [14] corresponds to the initial conditions $\tan\varphi = -1$ ($\varphi = 135°$ and $315°$) and $k = 0.206$ (Fig. 1). In the vicinity of this orbit is a region of stable Lagrange trajectories. The motion forms a series of oscillations in the vicinity of the Schubart orbit (Fig. 2).

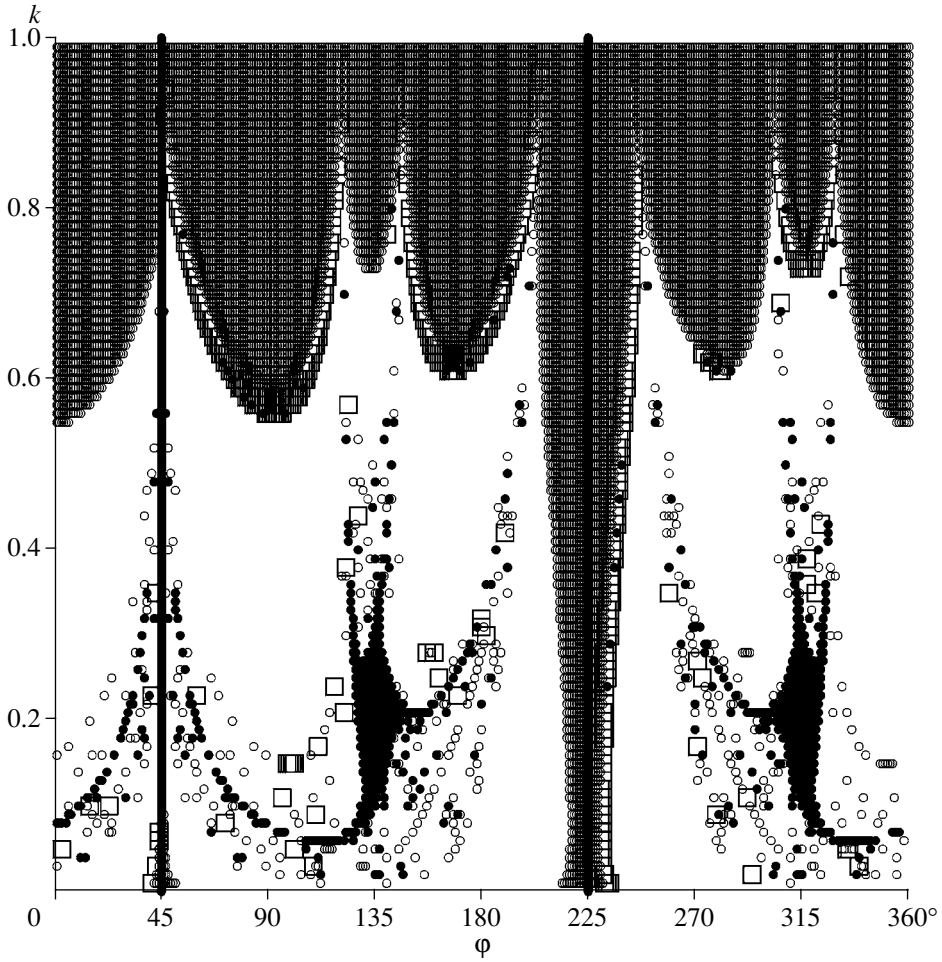

Fig. 3. Dependence of the evolutionary scenario on the initial conditions. Departures are hollow circles, distant ejections ($R > 30$) are squares, and undisrupted systems are filled circles. The vertical lines at $\varphi = 45°$ and $\varphi = 225°$ correspond to triple close encounters.

3.3. Classification of States

In the region of the initial conditions (φ, k), presented in Fig. 3, there are sets of points corresponding to different evolutionary scenarios:

(1) ejection of one of the outer bodies with its return;

(2) escape or a distant ejection ($R > 30$);

(3) stable systems;

(4) triple close encounters.

As noted above, triple close encounters in the region of the initial conditions correspond to the lines $\varphi = 45°$ and $225°$, i.e., to a set of zero measure.

The largest fraction of the region of initial conditions is occupied by points corresponding to ejections with returns of the ejected body. The fraction of escapes and conditional escapes increases with the parameter k (the closeness of the triple encounter). Departures form somewhat complex zones in the upper part of the region of initial conditions, which are adjacent to each other. The zones of conditional escapes border on the zones of escapes. Some escape regions are located along the triple-close-encounter lines. The regions of undisrupted trajectories form quadrangles with elongated lines emanating from their peaks and dividing the region of escapes.

Table 1 presents the fractions of various evolutionary scenarios. The fraction of ejections occupies about 60%, while that of escapes occupies about 35% of the region of initial conditions. The fractions of ejections of the right and left bodies are approximately the same.

3.4. Dependence of the Ejection Length on the Initial Conditions

Let us consider the dependence of the ejection length R on the initial conditions determined by the parameters (φ, k), presented in Figs. 4a, 4b, and 5.

Table 1. Fractions of various types of evolution

Type	Fraction	
Ejections:	0.599	
left body		0.308
right body		0.291
Departures:	0.370	
conditional		0.015
precise		0.355
Undisrupted systems	0.026	
Triple close encounters	0.005	

Figure 4 shows $R(\varphi)$ for all the k values considered, while Fig. 5 shows $R(k)$ for all φ for ejections of the left body; the $R(k)$ diagram for the right body has the same appearance and is not presented. The ejection length is mainly confined to the interval from one to ten. Departures of bodies occur in the vicinity of triple close encounters when $\varphi = 225°$. In some places, we observe regular elongated structures, which will be discussed below.

The $R(k)$ dependence in Fig. 5 shows a region with a low density of points to the left of the bounding curve, which grows from $k \approx 0.15$ and $R \approx 2$ to $k \approx 0.55$ and $R = 30$.

Figures 6a–6c and 7a–7c present as an example several $R(\varphi)$ diagrams for specified values of k and several $R(k)$ diagrams for specified values of φ. We can see regions of continuous variations of the ejection lengths $R(\varphi)$ and $R(k)$ and a zone in which these functions behave stochastically. In these stochastic zones, there is an alternation of ejections of the left (plus signs) and right (squares) bodies in the presence of small variations of the initial conditions (Fig. 6).

In Fig. 6, we observe symmetrical behavior relative to the points corresponding to triple close encounters at $\varphi = 45°$ and $\varphi = 225°$. There are ejections of different bodies at these symmetry points—right and left, respectively. The region of escapes in the vicinity of the triple close encounter at $\varphi = 225°$ is bounded by regular curves.

For regular trajectories, the maxima of the continuous $R(\varphi)$ curves grow with k. The regular dependences form single-peaked structures that are symmetric about the lines corresponding to triple close encounters. The characteristics of these structures (their positions $\varphi_{\max}$ and the heights $R_{\max}$ of the maxima, as well as the length of the zone of regular behavior $\Delta\varphi$) are presented in Table 2. The last column of this table presents the total relative length δ of these zones of regular behavior. We can see that, as k grows, the regular zones become wider, the maximum ejection length in these zones grows, and, in the end, the ejections are replaced by escapes in the central regions of these zones (associated with the decrease in δ for $k = 0.7$). For stochastic trajectories, the ejection length is mainly confined to the interval $R \in (2, 10)$. Note that no stochastic trajectories are visible for $k = 0.7$.

Figure 7 presents $R(k)$ for angles φ in different quarters with a step of $\Delta\varphi = 120°$. The values of φ are indicated in the panels. We can see both regular structures and regions where the points are scattered irregularly. Two families can be distinguished among the regular structures:

(1) growing curves with inflection points at $R \approx 6$;

(2) curves that originate from the horizontal axis ($k = 0$).

If there are curves of both families for some fixed value of φ, the points between them will be distributed irregularly. If only one regular structure is observed, the stochastic points are distributed on one side of it. The irregularly distributed points are primarily concentrated in the band $R \in (1, 10)$.

The data on the regular structures are presented in Table 3 for steps in φ of 10°. The table presents the values of φ, k_1 and k_2, corresponding to the beginning and end of the zone of regular behavior, and the values of (k_b, R_b) for the inflection points. The inflection points have roughly the same value $R_b \approx 5$. Systematic shifts in the regular curves $R(k)$ are observed as φ is varied.

3.5. Departures and Conditional Escapes

The regions of initial conditions corresponding to escapes form continuous sets of points and sets of isolated points. The latter are located along the region of stable orbits (Fig. 3). The continuous sets of points are joined at the values

$$\varphi = \{45°, 120°, 150°, 200°, 245°, 300°, 320°\}.$$

Minima in the continuous regions of escapes are reached at the values $k = \{0.55, 0.6, 0.72\}$. These regions are abutted from below by narrow zones of conditional escapes.

It is of interest to consider the dependence of the escape energy E (14) on the angle φ (Figs. 8a, 8b). In Fig. 8, we can see curves along which the energy varies in a regular fashion. Each of these curves corresponds to a specific value of the virial coefficient k, with their maxima shifting upward with growth in k. These curves are symmetric about the triple close encounters at $\varphi = 45°$ and 225°. The escape curves for the left body have maxima at $\varphi = 90°$, 180°, and 315°, while the curves for the right body have maxima

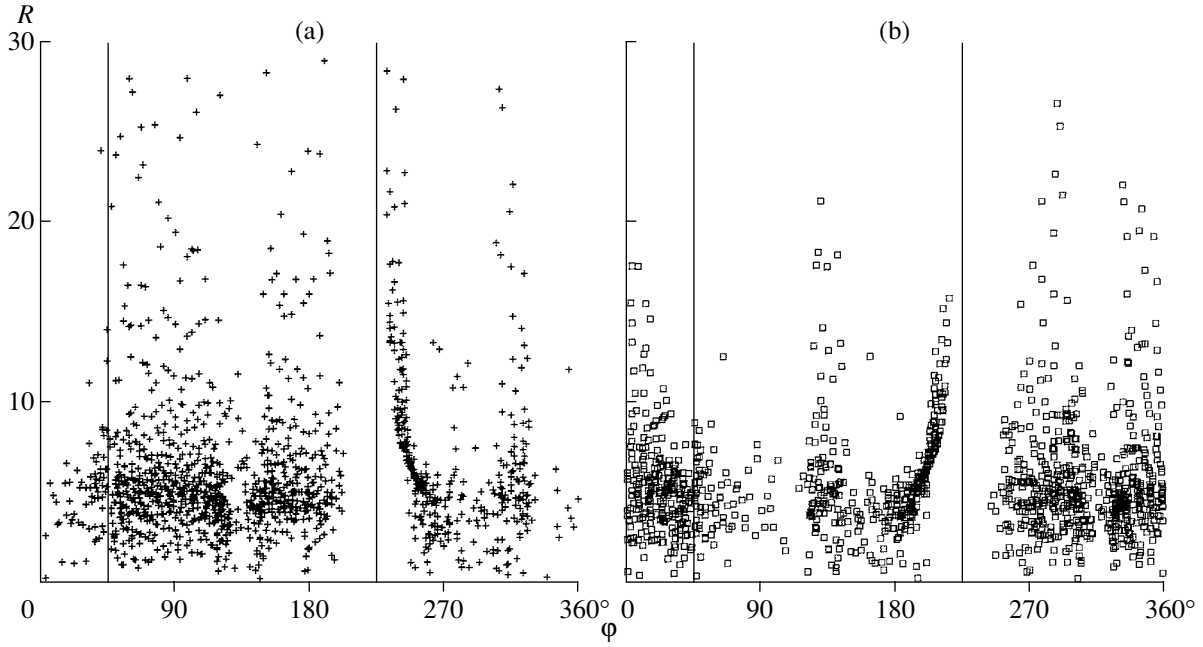

Fig. 4. Dependence of the ejection length on the angle φ for ejections of the (a) left body and (b) right body. The vertical lines correspond to triple close encounters.

at $\varphi = 0°$, 135°, and 270°. The energy grows without bound as the curve for the triple close encounter $\varphi = 225°$ is approached.

Figures 9a–9c present the dependence of the energy E on the initial value of the virial coefficient k for various intervals of the angle φ. Departures of the left and right bodies are shown by plus signs and squares, respectively. Regular, elongated structures are observed when the virial coefficient is $k > 0.5$. In the vicinity of the triple close encounter at $\varphi = 225°$ (Fig. 9b), regular structures also appear for small k, beginning with $k = 0$. At the same time, randomly scattered points are observed only when $k > 0.2$. These structures correspond to the continuous regions of escapes in Fig. 3. Overall, there is an increase in the energy with growth in the closeness of the triple encounter. The region of growth in E has a smooth envelope on its left side. Randomly scattered points are observed to the left of this envelope, while primarily regular structures are observed to its right. The zones of regular behavior for different intervals of φ join each other.

3.6. Undisrupted Trajectories

Near the stable Schubart orbit (Fig. 1), there is a region of trajectories that do not become disrupted over times $t > 100$. The initial conditions (φ, k) for these trajectories are shown in Fig. 10. They form two elongated continuous regions symmetrically placed about the line for the triple close encounters at $\varphi = 225°$. Elongated "tentacles" emerge from the four extremities of these regions. Their discontinuous nature may be associated with the discreteness of the specified initial conditions. These structures separate alternating regions containing and not containing sets of "scattered" points. Two elongated structures are located symmetrically about the $\varphi = 45°$ triple-

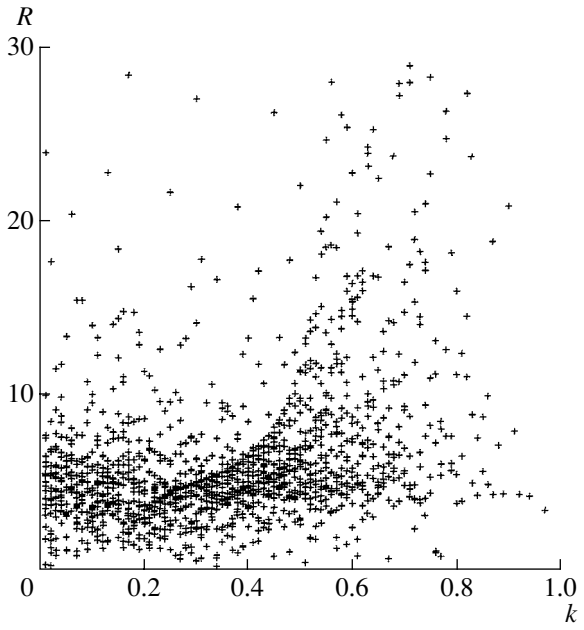

Fig. 5. Dependence of the ejection length of the left body on the virial coefficient k.

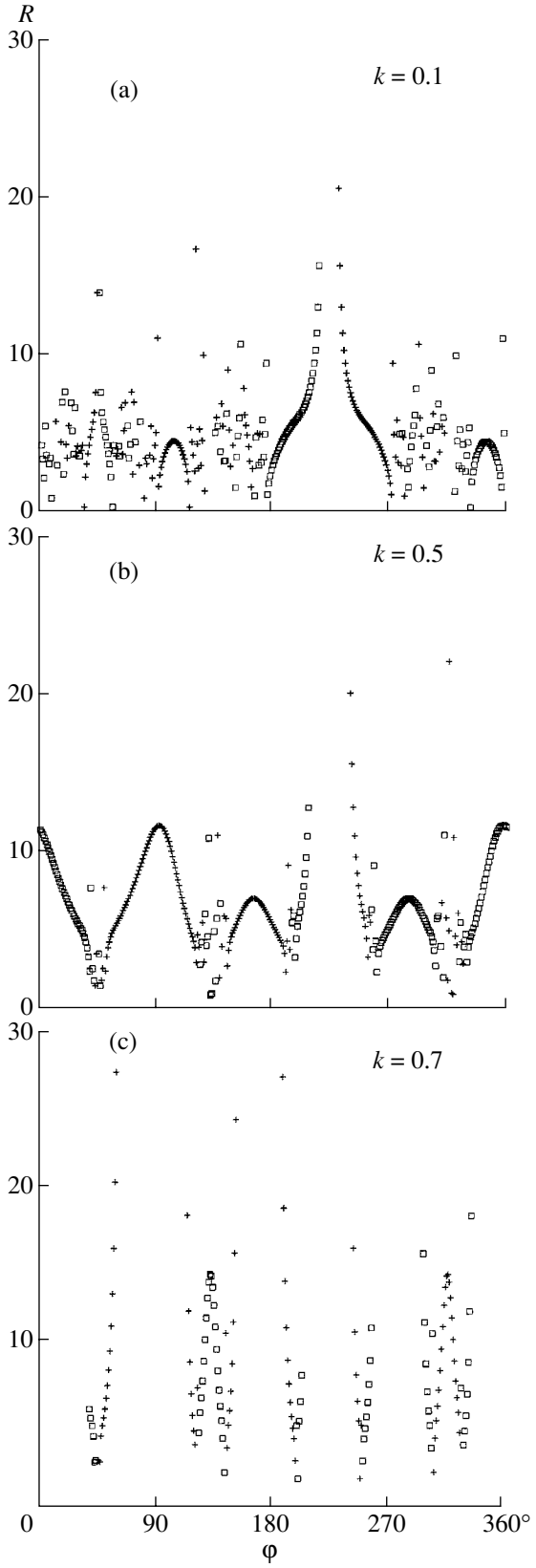

Fig. 6. $R(\varphi)$ diagrams for specified values of k. The plus signs and squares correspond to ejections of the left and right bodies, respectively.

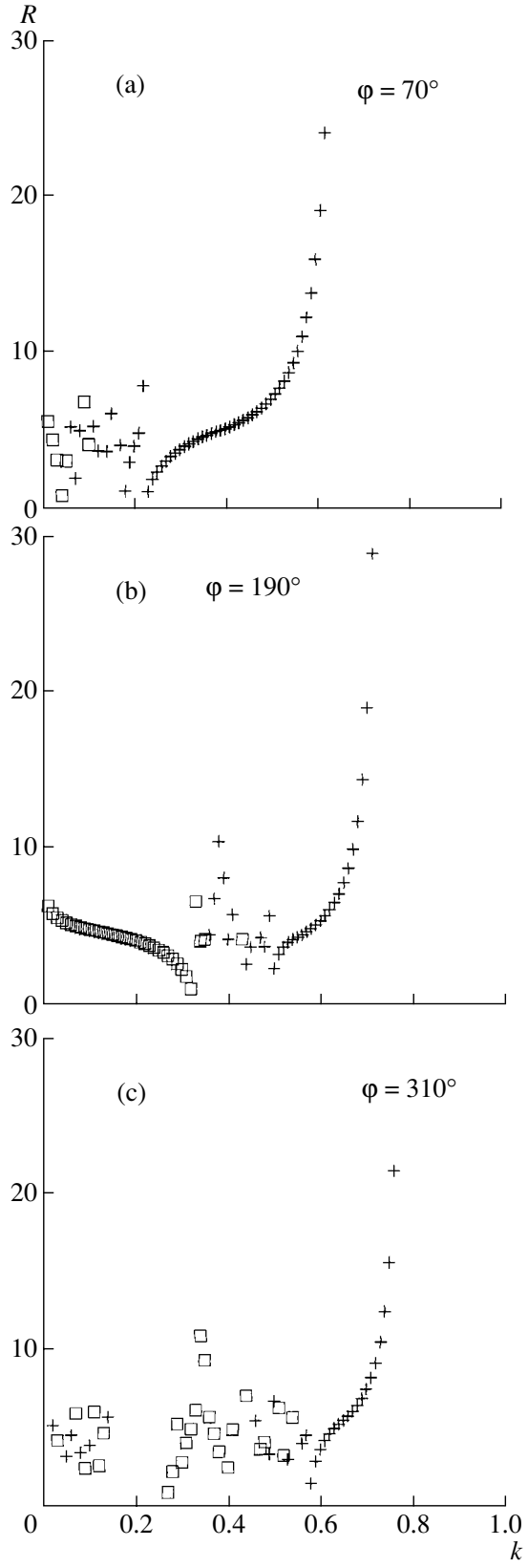

Fig. 7. $R(k)$ diagrams for specified values of the angle φ with a step of 120°. The plus signs and squares correspond to ejections of the left and right bodies, respectively.

Table 2. Characteristics of regular structures in the $R(\varphi)$ dependences

k	φ_{max}	R_{max}	$\Delta\varphi$	δ
0.1	110°; 340°	4.8	25°	0.14
0.3	90°; 360°	5.0	60°	0.44
	160°; 290°	3.0	20°	
0.5	93°; 357°	12	70°	0.56
	165°; 300°	7.0	30°	
0.7	135°; 315°	15	25°	0.14

close-encounter line. Undisrupted trajectories having initial conditions that do not correspond to the regular structures appear to move to states of ejection or escape over long times.

4. DISCUSSION

We investigated the evolution of 35 640 cases of the one-dimensional three-body problem with equal masses in our numerical simulations. Regions of initial conditions corresponding to the ejection of one of the outer bodies with its return, escapes, and undisrupted trajectories associated with the central periodic orbit of Schubart can be distinguished. We have investigated the dependences between the ejection length and the parameters (k, φ) specified by the initial conditions.

The dependence of the ejection length R on the closeness of the triple close encounter (Fig. 5) shows three populations of points:

(1) an approximately horizontal band of points near the line $R = 5$;

(2) a population to the right of the smooth envelope, beginning from $k \approx 0.15$ and asymptotically approaching the vertical line $k \approx 0.6$;

(3) a set of scattered points to the left of the envelope, above the band.

The degree of regularity in the dependence of the ejection length on the initial conditions increases with the closeness of the encounter (Fig. 6). The horizontal band corresponding to the first population is primarily determined by small values $k \leq 0.3$.

Continuous and stochastic structures are visible in the $R(k)$ diagrams for fixed values of φ (Fig. 7). Usually, stochastic structures correspond to small values of k and short ejection lengths. Regular structures are more often associated with large k values and extend upward without bound. Within each 45° interval of width, there is a shift of the regular structures toward larger k values. The function $R(k)$ shows periodic behavior with a period of 45° (see also Fig. 3) and an alternation of the component being ejected.

Table 3. Characteristics of regular structures in the $R(k)$ dependences

φ	k_1	k_2	k_b	R_b
10°; 80°	0.20	0.56	0.33	5.2
20°; 70°	0.22	0.61	0.39	5.1
30°; 60°	0.30	0.68	0.46	5.0
40°; 50°	0.0	0.20	0.08	5.7
	0.50	0.77	0.66	5.0
100°; 350°	0.16	0.55	0.30	5.0
110°; 340°	0.18	0.63	0.36	5.0
120°; 330°	0.18	0.30	0.23	4.6
	0.30	0.88	0.56	4.6
130°; 320°	0.50	0.73	0.58	5.0
140°; 310°	0.58	0.76	0.64	5.0
150°; 300°	0.30	0.77	0.50	5.0
160°; 290°	0.28	0.62	0.41	5.0
170°; 280°	0.30	0.60	0.43	5.1
190°; 260°	0.0	0.32	0.15	4.8
	0.50	0.70	0.57	4.9
200°; 250°	0.0	0.65	0.33	6.0
	0.72	0.82	–	–
210°; 240°	0.0	0.49	–	–
220°; 230°	–	–	–	–

In the vicinity of the triple close encounter with $\varphi = 225°$ (Fig. 7b), we observe continuous structures and, at small k, structures emanating from $k = 0$. The upper left boundary of these curves approximately corresponds to the upper value of the ejection length for "torn" structures.

There are also two populations of points in the $E(k)$ diagrams for the dependence of the energy of the departing body on the initial virial coefficient: discrete sets at small k and continuous sets primarily at $k > 0.5$. The envelopes of the continuous sets can be approximated by chain curves. In the region of the triple close encounter at $180° < \varphi < 270°$, there are two continuous structures (Fig. 9b): one begins at $k = 0$ and continues to $k = 1$, while the second begins at $k = 0.65$. There are about twice as many points in the first of these structures than in the second.

The stable trajectories associated with the Schubart orbit determine to a significant degree the evolu-

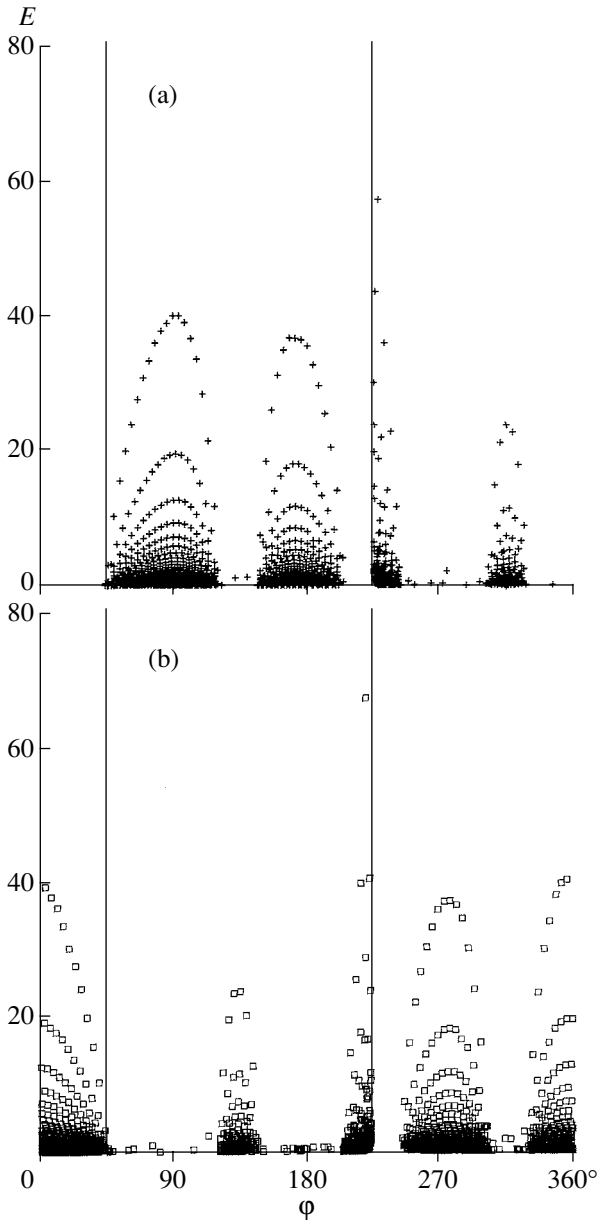

Fig. 8. Dependence of the energy E for the final hyperbolic motion on the angle φ for escapes of the (a) left body and (b) right body.

tionary scenario as a function of the initial conditions (Fig. 10). The discrete sets are concentrated along elongated structures emanating from the peaks of the solid region of stable motions. The "tentacles" extending upward in the stable region separate the set of initial conditions into eight parts and give rise to the repetition of the evolutionary scenarios with a period of 45° in φ, with alternating ejections and escapes of the right and left bodies.

We conclude that, to a large degree, stochastic discrete sets of points are characteristic of wide systems ($k < 0.5$), while continuous sets of points are

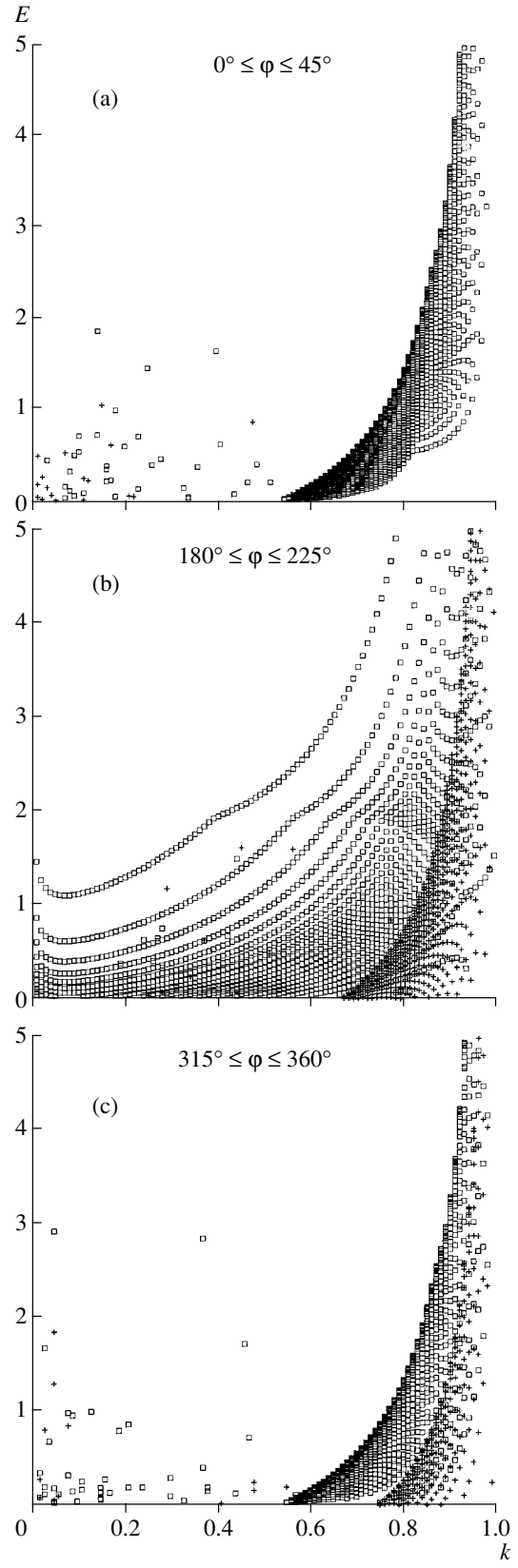

Fig. 9. $E(k)$ diagrams for various intervals of φ. The plus signs show escapes for the left body, and the squares show escapes for the right body.

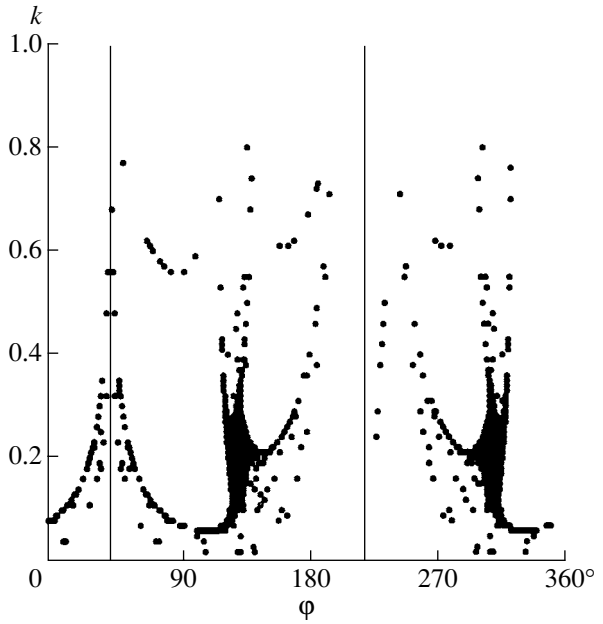

Fig. 10. Region of initial conditions for undisrupted systems.

associated with close systems ($k > 0.5$ for escapes and $k > 0.2$ for ejections). Note that $k \approx 0.2$ corresponds to the central, periodic orbit.

Thus, in the linear three-body problem with equal masses, the result of "exchange" triple encounters depends in a complex way on the initial parameters of the encounter: together with the zones of continuous behavior, there are appreciable regions of stochasticity.

The results we have obtained here, in particular the dependences of the ejection length on the parameters of the triple encounter, can be extended to "exchange" triple encounters that are close to the linear case, including systems with components with unequal masses, to which we will dedicate a separate paper. Similar situations can be realized in the dynamical evolution of hierarchical triple stars and in cases when there are no encounters between components. Therefore, the results obtained are of general interest for studies of the dynamics of triple-star systems.

REFERENCES

1. V. Szebehely, Celest. Mech. **4**, 116 (1971).
2. T. A. Agekyan and A. I. Martynova, Vestn. Leningr. Univ., No. 1, 122 (1973).
3. T. A. Agekyan and Zh. P. Anosova, Astron. Zh. **44**, 1261 (1967) [Sov. Astron. **11**, 1006 (1967)].
4. T. A. Agekyan and Zh. P. Anosova, Astrofizika **4**, 31 (1968).
5. Zh. P. Anosova and N. N. Zavalov, Tr. Astron. Obs. Leningr. Gos. Univ. **36**, 109 (1981).
6. V. Szebehely, Astron. Astrophys. **78**, 349 (1979).
7. Zh. P. Anosova and N. N. Zavalov, Astron. Zh. **66**, 152 (1989) [Sov. Astron. **33**, 79 (1989)].
8. T. A. Agekyan and Zh. P. Anosova, Astron. Zh. **68**, 1099 (1991) [Sov. Astron. **35**, 551 (1991)].
9. S. J. Aarseth, J. P. Anosova, V. V. Orlov, and V. G. Szebehely, Celest. Mech. Dyn. Astron. **60**, 131 (1994).
10. V. V. Orlov, A. V. Petrova, and A. I. Martynova, Pis'ma Astron. Zh. **27**, 795 (2001) [Astron. Lett. **27**, 678 (2001)].
11. J. P. Anosova and V. V. Orlov, Celest. Mech. Dyn. Astron. **59**, 327 (1994).
12. J. Yoshida, in *The Few-Body Problem,* Ed. by M. Valtonen (Kluwer, Dordrecht, 1988), p. 77.
13. J. Hietarinta and S. Mikkola, Chaos **3**, 183 (1993).
14. J. Schubart, Astron. Nachr. **283**, 17 (1956).
15. C. Marchal, Celest. Mech. **9**, 381 (1974).
16. J. Yoshida, Publ. Astron. Soc. Jpn. **24**, 391 (1972).

Translated by D. Gabuzda

Astronomy Reports, Vol. 46, No. 11, 2002, pp. 942–954. Translated from Astronomicheskiĭ Zhurnal, Vol. 79, No. 11, 2002, pp. 1044–1056.

Dynamical Evolution of Multiple Stars

A. V. Rubinov, A. V. Petrova, and V. V. Orlov

Astronomical Institute, St. Petersburg State University, Universitetskiĭ pr. 28, Petrodvorets, 198504 Russia

Received February 14, 2002; in final form, May 23, 2002

Abstract—We have modeled the dynamical evolution of small groups of $N = 3$–18 stars in the framework of the gravitational N-body problem, taking into account possible coalescences of stars and the ejection of single and binary stars from the system. The distribution of states is analyzed for a time equal to 300 initial crossing times of the system. The parameters of the binaries and stable triple systems formed, as well as those of ejected single stars, are studied. In most cases, the evolution of the group results in the formation of a binary or stable triple system. The orbital eccentricities of the binaries formed are distributed according to the law $f(e) = 2e$. As a rule, stable triple systems display pronounced hierarchy (the mean ratio of the semimajor axes of the outer and inner binaries is about 20 : 1). Stars are ejected with velocities from several km/s to several tens of km/s. The results of the modeling are compared with the parameters of observed wide binaries and triple systems. © *2002 MAIK "Nauka/Interperiodica"*.

1. INTRODUCTION

In the late 1960s, van Albada [1] suggested that wide binary and multiple stars result from the decay of low-multiplicity systems. According to this hypothesis, these systems have characteristic sizes of 100 to 1000 AU and can contain from several to several tens of stars. Recent modeling of the fragmentation of molecular-cloud cores [2, 3] indicates that this process can, indeed, result in the formation of non-hierarchical multiple systems with these parameters. The dynamical evolution of such systems could lead to the formation of both binary stars and stable systems of higher multiplicity.

The dynamics of low-multiplicity systems have been modeled in numerous studies (see, for example, [4, 5] and references therein). However, most have been concerned primarily with the dynamical evolution of triple systems (see, for example, [6–8]). The dynamics of stellar systems with higher multiplicities have been considered less frequently. One exception is the studies [9–11], in which systems of $N = 3$, 4, and 5 stars are modeled. A number of authors have investigated the parameters of single stars ejected from low-multiplicity systems with $N = 3$–10 stars in the course of their dynamical evolution [12, 13].

Here, we analyze the basic characteristics of the products of the dynamical evolution of low-multiplicity stellar systems with various numbers of stars N. We also study the effect of the initial mass spectrum on the results of the evolution.

2. THE MODELING

We modeled the dynamical evolution of low-multiplicity stellar systems in the framework of the gravitational N-body problem by treating the stars as point masses. The main problems encountered in the numerical integration of the equations of motion are related to possible binary and multiple interactions of the objects. To overcome this difficulty, we used the method of chain regularization suggested in [14].

In the course of their dynamical evolution, stars may acquire separations comparable to their radii, with their subsequent coalescence. To take these events into account, we used the following coalescence criterion based on the results of SPH modeling [15, 16]. Stars i and j will coalesce if

$$r_{ij} < \kappa(R_i + R_j), \tag{1}$$

where r_{ij} is the distance between the stars, R_i and R_j are their radii, and the parameter $\kappa = \frac{3}{4}$. The mass of the product of the coalescence is taken to be equal to the sum of the masses of the colliding stars. We determined the radii of the stars and the product of the coalescence using the approximate mass–radius relation for main-sequence stars

$$\begin{cases} R_i \approx \sqrt{1.5 m_i}, \text{ for } m_i > 1.5 M_\odot \\ R_i \approx m_i, \text{ for } m_i \le 1.5 M_\odot, \end{cases} \tag{2}$$

where m_i is the mass of star i and $M_\odot$ is the mass of the Sun.

In the course of the dynamical evolution of a system, single and binary stars, as well as subsystems of higher multiplicity, can be ejected from the system or recede to substantial distances from its center

1063-7729/02/4611-0942$22.00

Table 1. Distribution of states as a function of N at time 300 T_{cr}

N	Mass spectrum	Binaries	Two singles	Stable triples	Unstable triples	Higher multiplicity	n
3	EM	0.70	–	0.01	0.29	–	1000
	SM	0.78	–	0.01	0.21	–	1000
6	EM	0.57	0.05	0.15	0.09	0.14	500
	SM	0.56	0.01	0.14	0.16	0.13	500
9	EM	0.41	0.09	0.15	0.07	0.28	500
	SM	0.55	0.03	0.16	0.14	0.12	500
12	EM	0.37	0.12	0.10	0.06	0.35	500
	SM	0.47	0.04	0.17	0.16	0.16	500
15	EM	0.35	0.11	0.07	0.07	0.40	500
	SM	0.49	0.06	0.13	0.15	0.17	500
18	EM	0.34	0.10	0.08	0.04	0.44	250
	SM	0.51	0.06	0.11	0.14	0.18	250

of mass. In the latter case, such formations can be ejected from the system via several mechanisms, such as the effect of the gravitational field of the parent cloud (for young systems) or of an adjacent stellar system.

We took such events into account in the numerical integration as follows. If a single or binary star receded to a substantial distance from the center of mass of the system and was simultaneously not a member of a subsystem of higher multiplicity, the object was considered to have left the system. In addition, for binaries, we checked that the total energy was negative. Possible ejections of higher-multiplicity subsystems were not considered.

We used the following ejection criteria. The star i was considered to be ejected from the system if

$$\begin{cases} \rho_i > \lambda d \\ r_{ij} > 2\eta\lambda d, \ j \neq i, \end{cases} \tag{3}$$

where ρ_i is the distance from the given body to the center of mass of the other stars, r_{ij} is the distance between bodies i and j, d is the mean current size of the system, the parameter $\lambda = 30$, and $\eta = \frac{1}{5}$. The mean current size of the system was calculated according to the formula

$$d = \frac{G}{2|E|}\sum_{i<j} m_i m_j, \tag{4}$$

where E is the total energy of the system and G is the gravitational constant.

The binary formed by stars i and j was assumed to have left the system if

$$\begin{cases} \rho_i > \lambda d \\ \rho_j > \lambda d \\ 0 < a_{ij} < \eta\lambda d \\ r_{ik} > 2\eta\lambda d, \ k \neq i, j \\ r_{jk} > 2\eta\lambda d, \ k \neq i, j, \end{cases} \tag{5}$$

where a_{ij} is the semimajor axis of the binary consisting of bodies i and j.

The dynamical evolution of the low-multiplicity systems was followed to a time equal to 300 T_{cr}, where

$$T_{cr} = \frac{G}{(2|E|)^{\frac{3}{2}}}\sum_{i<j} m_i m_j \sqrt{\sum_{k=1}^{N} m_k} \tag{6}$$

is the initial mean crossing time of the system. The integration was also stopped if the initial system decayed into a binary system.

The regularized equations of motion were integrated using a fourth-order Runge–Kutta method with automatic step selection. The accuracy of the calculations was verified using the first integrals of motion. During the calculations, the relative errors of the area and energy integrals did not exceed 10^{-5}. The integrals of motion of the center of mass were maintained with better accuracy.

The initial conditions were specified as follows. We considered systems initially consisting of $N = 3$, 6, 9, 12, 15, and 18 stars, assuming that the stars had

Table 2. Parameters of final binaries

N	Mass spectrum	$\overline{a}/d$	$a_{\frac{1}{2}}/d$	$\overline{e}$	$e_{\frac{1}{2}}$	$\overline{q}$	$q_{\frac{1}{2}}$	n
3	EM	0.42 ±	0.299	0.715 ±	0.765	0.990 ±	1.000	697
		± 0.089		± 0.009		± 0.003		
	SM	0.413 ±	0.391	0.665 ±	0.712	0.567 ±	0.575	776
		± 0.007		± 0.008		± 0.009		
6	EM	0.843 ±	0.061	0.698 ±	0.733	0.934 ±	1.000	288
		± 0.202		± 0.014		± 0.010		
	SM	0.193 ±	0.116	0.669 ±	0.702	0.567 ±	0.550	282
		± 0.024		± 0.014		± 0.015		
9	EM	2.05 ±	0.036	0.694 ±	0.749	0.851 ±	1.000	204
		± 1.02		± 0.016		± 0.017		
	SM	0.490 ±	0.075	0.659 ±	0.714	0.549 ±	0.537	277
		± 0.241		± 0.015		± 0.016		
12	EM	1.52 ±	0.031	0.675 ±	0.701	0.761 ±	1.000	184
		± 0.62		± 0.016		± 0.020		
	SM	1.00 ±	0.060	0.660 ±	0.684	0.538 ±	0.539	237
		± 0.63		± 0.015		± 0.017		
15	EM	1.350 ±	0.021	0.673 ±	0.712	0.715 ±	0.500	176
		± 0.595		± 0.017		± 0.021		
	SM	0.152 ±	0.049	0.639 ±	0.670	0.546 ±	0.538	243
		± 0.040		± 0.015		± 0.016		
18	EM	0.912 ±	0.019	0.708 ±	0.764	0.660 ±	0.500	85
		± 0.698		± 0.024		± 0.032		
	SM	0.239 ±	0.044	0.627 ±	0.680	0.522 ±	0.483	127
		± 0.091		± 0.021		± 0.022		

a random, uniform distribution inside a sphere with radius $r = 100$ AU. The velocities of the stars were specified so that the virial theorem was fulfilled for the system as a whole. The velocity distribution was assumed to be isotropic.

We considered two initial mass spectrà for the system: equal masses (with the mass of each star taken to be that of the Sun) and a Salpeter mass spectrum [17]:

$$f(m) \sim m^{-2.35}, m/M_\odot \in [0.4; 10]. \qquad (7)$$

We studied the dynamical evolution of 1000 systems with $N = 3$ and of 250 systems for the case $N = 18$ for each initial mass spectrum. For each other set of parameters, we analyzed 500 versions of the initial conditions.

3. MODELING RESULTS

3.1. Distribution of States

The dynamical evolution of non-hierarchical multiple systems is accompanied by the dissipation of stars from the system, resulting, as a rule, in the formation of stable systems of lower multiplicity. To clarify which systems can form during the decay of multiple systems, we derived the distribution of states for the systems for a time equal to 300 T_{cr}. The specified states corresponded to binaries with negative total energy, binaries with positive total energy (two single stars), unstable triple systems, stable triple systems, and systems of higher multiplicity. The stable and unstable triple systems were distinguished using the

Table 3. Parameters of escaping binaries

N	Mass spectrum	$\overline{a}/d$	$a_{\frac{1}{2}}/d$	$\overline{e}$	$e_{\frac{1}{2}}$	$\overline{q}$	$q_{\frac{1}{2}}$	n
6	EM	0.439 ±	0.062	0.668 ±	0.710	1.000 ±	1.000	140
		± 0.088		± 0.021		± 0.000		
	SM	0.576 ±	0.322	0.682 ±	0.734	0.698 ±	0.749	59
		± 0.080		± 0.030		± 0.026		
9	EM	0.332 ±	0.029	0.682 ±	0.716	0.980 ±	1.000	251
		± 0.050		± 0.014		± 0.006		
	SM	0.623 ±	0.133	0.662 ±	0.696	0.656 ±	0.666	95
		± 0.096		± 0.024		± 0.023		
12	EM	0.342 ±	0.024	0.676 ±	0.736	0.935 ±	1.000	325
		± 0.040		± 0.013		± 0.010		
	SM	0.794 ±	0.275	0.708 ±	0.763	0.677 ±	0.710	154
		± 0.090		± 0.017		± 0.017		
15	EM	0.424 ±	0.027	0.675 ±	0.699	0.883 ±	1.000	343
		± 0.050		± 0.012		± 0.012		
	SM	0.815 ±	0.350	0.665 ±	0.704	0.652 ±	0.648	178
		± 0.091		± 0.016		± 0.016		
18	EM	0.505 ±	0.020	0.645 ±	0.691	0.880 ±	1.000	176
		± 0.086		± 0.018		± 0.017		
	SM	0.710 ±	0.183	0.653 ±	0.705	0.627 ±	0.629	82
		± 0.127		± 0.029		± 0.025		

analytical criterion of Golubev [18], which requires the calculation of the parameter S using the formula

$$S = \frac{c^2|E|}{G^2\overline{M}^5}, \qquad (8)$$

where c is the modulus of the angular momentum vector of the triple system and $\overline{M}$ is the mean mass of its components.

A triple system will be stable to the exchange of a component of an inner binary and a distant component if S exceeds the critical value $S_{\rm cr}$ (in the equal mass case, $S_{\rm cr} = \frac{25}{4}$); in this case, the system hierarchy will be maintained for an unlimited time. Otherwise, the hierarchical structure can be disrupted. However, triple systems can decay without disrupting the hierarchy. Thus, not all systems stable according to this criterion will have their motions restricted.

Table 1 presents the modeling results for the case of an equal mass spectrum (EM) and Salpeter mass spectrum (SM). Systems initially consisting of $N = 3, 6, 9, 12, 15$, and 18 stars and located in a state of virial equilibrium ($k = 0.5$) are presented. The last column contains the number n of sets of initial conditions considered.

The following conclusions can be drawn from Table 1. In most cases, the dynamical evolution of multiple stars results in the formation of a binary system. In a number of cases, an unstable triple system that is formed has not been disrupted by the time the integration is stopped; later, however, such systems should decay. The probability of a stable triple system forming is rather high. Relatively few binaries with positive total energies are formed because of the increase of the total energy of the system due to the coalescence of stars and ejection of binaries. In many cases (particularly for large N), the dynamical evolution of the system has not finished by the end of the integration time; this can be seen in the second to last column of Table 1, which indicates higher-multiplicity systems that will either decay over times longer than 300 $T_{\rm cr}$ or, possibly, prove to be stable

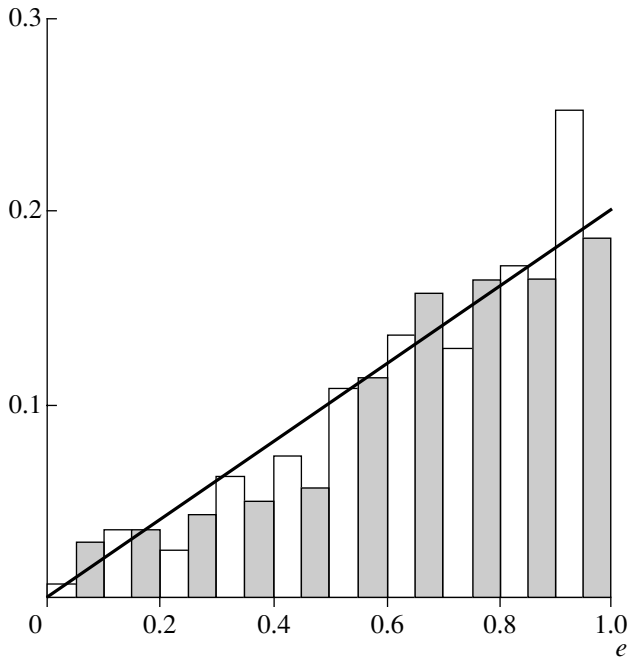

Fig. 1. The distributions of eccentricities for binaries in the equal-mass case. The solid line represents the law $f(e) = 2e$.

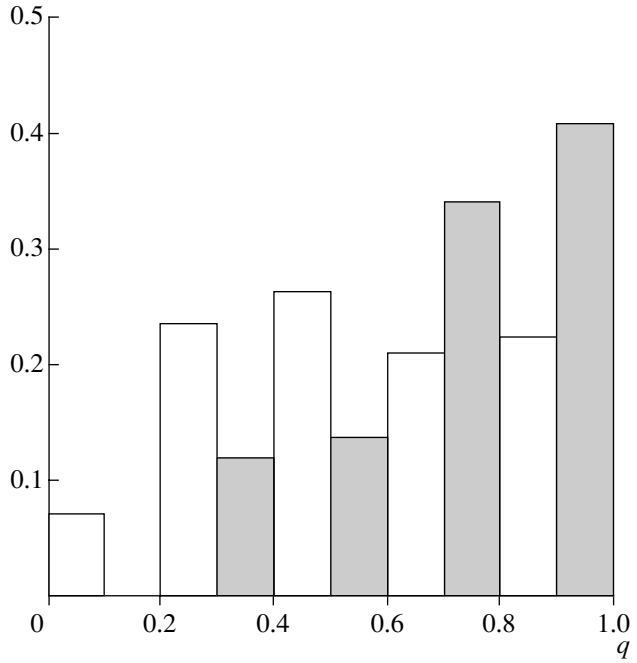

Fig. 2. Distribution of the parameter q for binaries formed for the Salpeter mass spectrum. The white and gray columns of the histogram correspond to final and escaping binaries, respectively.

systems. The fraction of binary and triple systems (both stable and unstable) decreases as N increases due to the increase in the number of systems that have not evolved. This fact is related to the deceleration of the dynamical evolution as the number of stars in the initial system increases.

3.2. Parameters of Binary Systems

In many cases, the dynamical evolution of multiple systems results in the formation of a final binary by the time 300 T_{cr}. In addition, some binaries are dissipated from the system; we will call these "escaping" binaries.

Table 2 presents the basic parameters of the final binaries: their semimajor axes a, eccentricities e, and component mass ratios $q = \frac{m_2}{m_1}$, where m_2 is the mass of the less massive component. The table presents the mean and median values of these parameters along with their mean errors. The semimajor axes are given in units of the mean initial size of a system d. The last column contains the number of final binaries formed. Table 3 presents the analogous parameters for the escaping binaries.

As a rule, the semimajor axes of the binaries (both final and escaping) are equal to within several hundredths of the initial size of the system to several times this size. If the physical size of a system is about 100 AU, the semimajor axes of the binaries will be in the interval 1–1000 AU. As the number of stars in the initial system increases, on average, the final binaries become closer to each other. This is due to the increase in the kinetic energy carried away by single stars as N increases. The escaping binaries do not display this trend. On average, the Salpeter initial mass spectrum gives rise to wider binaries than the equal mass spectrum, as is apparent from a comparison of the two medians (fourth column in Tables 2 and 3).

The mean and median eccentricities of the binaries that form are almost independent of the mass spectrum and N. Elongated systems dominate, as can also be seen in Fig. 1, which presents the distributions of eccentricities of final and escaping binaries formed for $N = 6$ and the case of equal masses. The solid line represents the eccentricity distribution $f(e) = 2e$, first derived by Ambartsumyan [19] for the equilibrium distribution of eccentricites of binaries in the stellar field and also by Monaghan [20] for binaries formed via the decay of triple systems. The distributions are consistent both with each other and with the theoretical law.

As a rule, final binaries contain the most massive stars of the system. The escaping binaries contain less massive stars, whose mean mass ratio is close to $\frac{2}{3}$ for the Salpeter initial mass spectrum. The mass ratio of the binary components q decreases as N increases, possibly due to the increased number of

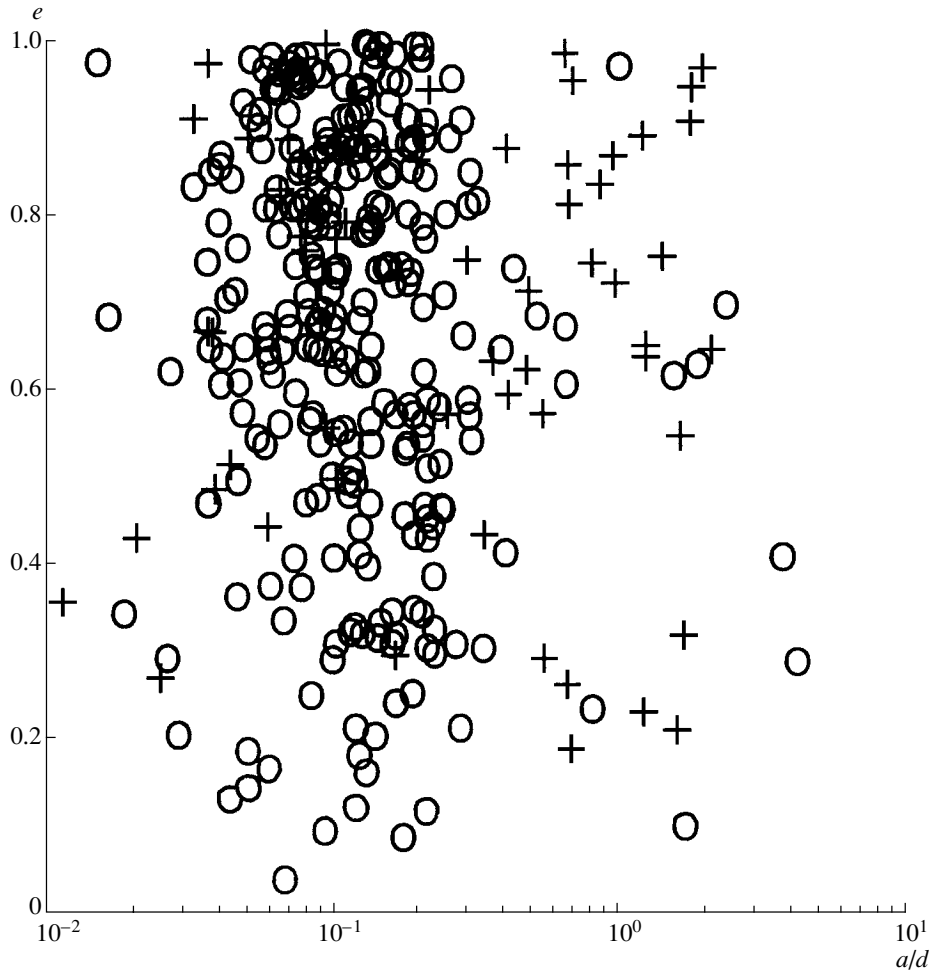

Fig. 3. Dependence of the semimajor axis on the eccentricity for the Salpeter mass spectrum. The circles and pluses correspond to final and escaping binaries, respectively.

coalescing stars. The number of coalescences may be indicated by the parameter q in the equal-mass case. If no coalescences occurred, both the mean and median values of q would be equal to 1.

Figure 2 presents the distribution of the parameter q for final and escaping binaries for the case $N = 6$ and the Salpeter initial mass spectrum. The distribution of component mass ratios for final binaries is flat for $q > 0.2$. In the case of escaping binaries, the distribution increases monotonically with increasing q. The shape of the distributions remains essentially the same for other values of N.

Figure 3 presents the dependence of the eccentricity e on the semimajor axis a for the final and escaping binaries, derived for $N = 6$ for systems with the Salpeter initial mass spectrum. A vertical strip is visible in the case of the final binaries and is less distinct for the escaping binaries. Its presence can be explained as follows. If final binaries are formed only due to ejections of single stars from the system, there should be a maximum semimajor axis for the binaries, which is reached if the single stars carry away the minimum energy needed for their ejection from the system. In this case, the final binary will be at the right border of the strip in the a–e plot. It can pass through the border to the right if ejections of binaries and coalescences occur, increasing the total energy of the system. As N increases, the strips become less distinct due to possible ejections of two or more binaries and also to the increase in the number of coalescences. The strips shift toward smaller a, reflecting the trend for the binary components to become closer to one another, due to the reasons discussed above.

3.3. Stable Triple Systems

We studied the orbital parameters of triple systems that were stable according to the criterion of Golubev. A triple system was treated as a superposition of two binaries: an inner binary consisting of the two closest bodies of the system and an outer binary. The two components of the outer binary are an object

Table 4. Orbital parameters of inner and outer binaries in stable triple systems

N	Mass spectrum	$\overline{a}_{\rm in}/d$	$a_{{\rm in}\,\frac{1}{2}}/d$	$\overline{e}_{\rm in}$	$e_{{\rm in}\,\frac{1}{2}}$	$\overline{a}_{\rm out}/d$	$a_{{\rm out}\,\frac{1}{2}}/d$	$\overline{e}_{\rm out}$	$e_{{\rm out}\,\frac{1}{2}}$	n
3	EM	0.403 ±	0.403	0.61 ±	0.63	4.65 ±	3.86	0.54 ±	0.52	8
		± 0.011		± 0.09		± 0.84		± 0.05		
	SM	0.412 ±	0.436	0.59 ±	0.60	5.59 ±	4.47	0.60 ±	0.63	12
		± 0.043		± 0.05		± 0.95		± 0.06		
6	EM	0.084 ±	0.065	0.69 ±	0.72	2.24 ±	1.97	0.47 ±	0.50	73
		± 0.011		± 0.03		± 0.19		± 0.02		
	SM	0.116 ±	0.104	0.63 ±	0.66	2.85 ±	2.29	0.50 ±	0.50	69
		± 0.007		± 0.03		± 0.23		± 0.02		
9	EM	0.044 ±	0.028	0.67 ±	0.69	1.18 ±	0.92	0.52 ±	0.55	76
		± 0.004		± 0.03		± 0.15		± 0.02		
	SM	0.080 ±	0.068	0.65 ±	0.68	1.86 ±	1.62	0.46 ±	0.45	79
		± 0.006		± 0.03		± 0.13		± 0.02		
12	EM	0.032 ±	0.021	0.62 ±	0.62	0.98 ±	0.78	0.50 ±	0.56	48
		± 0.004		± 0.03		± 0.15		± 0.03		
	SM	0.074 ±	0.059	0.60 ±	0.63	1.66 ±	1.34	0.45 ±	0.44	85
		± 0.007		± 0.03		± 0.11		± 0.02		
15	EM	0.038 ±	0.021	0.67 ±	0.70	0.92 ±	0.63	0.48 ±	0.46	37
		± 0.008		± 0.03		± 0.23		± 0.03		
	SM	0.075 ±	0.046	0.68 ±	0.64	2.26 ±	1.17	0.43 ±	0.44	67
		± 0.021		± 0.02		± 0.96		± 0.03		
18	EM	0.019 ±	0.011	0.63 ±	0.63	0.61 ±	0.31	0.43 ±	0.48	21
		± 0.005		± 0.05		± 0.21		± 0.05		
	SM	0.048 ±	0.039	0.65 ±	0.68	1.19 ±	0.95	0.46 ±	0.44	28
		± 0.005		± 0.04		± 0.15		± 0.04		

located at the barycenter of the inner binary with a mass equal to the combined mass of the inner-binary components, and the distant component of the triple system.

Table 4 presents the mean and median semimajor axes of the inner $a_{\rm in}$ and outer $a_{\rm out}$ binaries, as well as their eccentricities $e_{\rm in}$ and $e_{\rm out}$ and the errors of the mean values. The semimajor axes are given in units of the mean initial size of the system. The last column of the table contains the number of stable triple systems formed. Results are presented for the two mass spectra and various numbers of bodies N.

A distinction should be drawn between stable triple systems for the case $N = 3$ and those formed in the dynamical evolution of systems of higher multiplicity. The existence of stable triples for $N = 3$ is related to the chosen initial conditions, as is confirmed by the very small contribution of these systems to the distribution of states (1–2%; Table 1). We were primarily interested in systems formed as a result of the dynamical evolution of low-multiplicity systems and will not consider the parameters of stable triple systems for the case $N = 3$ further here.

We can draw the following conclusions from Table 4. The semimajor axes of the inner binaries are one to two orders of magnitude smaller than the initial sizes of the systems, while those of the outer binaries are comparable to the initial sizes to within an order of magnitude. The stable triple systems become closer as N increases for the same reason as the final binaries do. Both the inner and outer binaries

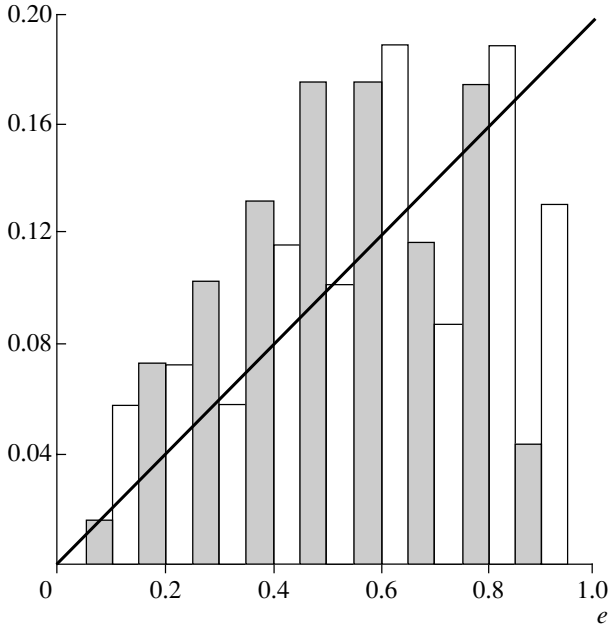

Fig. 4. Distributions of eccentricities for inner and outer binaries for the Salpeter mass spectrum. The white and gray columns correspond to the inner and outer binaries, respectively. The solid line represents the law $f(e) = 2e$.

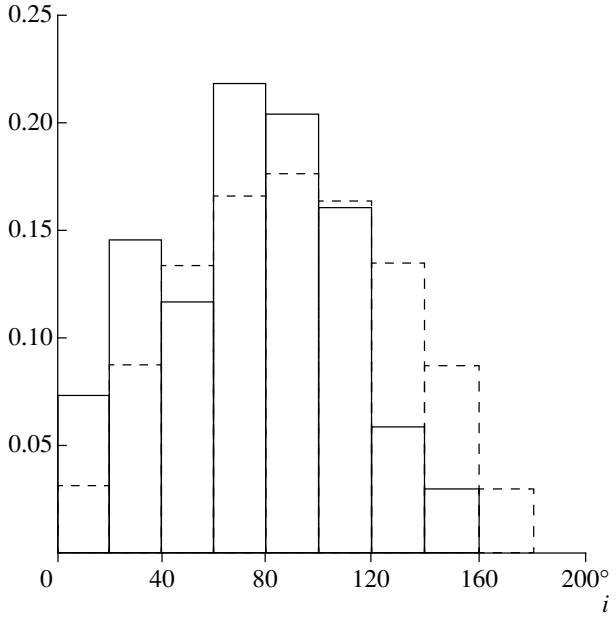

Fig. 5. Distribution of the angle i for the Salpeter mass spectrum (solid) and the random distribution $f(i) = \frac{1}{2}\sin i$ (dashed).

are somewhat wider in the case of the Salpeter initial mass spectrum than in the equal-mass case.

The orbital eccentricities for the outer binaries are, on average, smaller than those for the inner binaries. The mean eccentricities ($\bar{e}_{\rm in} \approx 0.7$, $\bar{e}_{\rm out} \approx 0.5$) are essentially independent of the number of stars N in the system and the initial mass spectrum.

Figure 4 presents the distributions of the orbital eccentricities for the inner and outer binaries for the Salpeter initial mass spectrum. We can see that they differ from the law $f(e) = 2e$: a deficiency of binaries with very elongated orbits is observed. The distribution displays a maximum for the outer binaries at $e \approx 0.5$. The appearance of the distributions remains the same as N and the initial mass spectrum are varied.

As a rule, the triple systems that form display a pronounced hierarchy. The ratio of the semimajor axes of the inner and outer binaries is virtually independent of N and the mass spectrum, and is, on average, 0.04.

Stable triple systems with prograde motions dominate. The mean angle i between the orbital angular-momentum vectors of the inner and outer binaries is approximately 75° and is essentially independent of the mass spectrum and number of stars N. Figure 5 presents distributions of the angle i for $N = 6$ for the Salpeter initial mass spectrum (solid) and the law $f(i) = \frac{1}{2}\sin i$ (dashed), which corresponds to random orientations of the momentum vectors. The distributions have the same general shape, but we can see some asymmetry favoring small values of i, which increases with N. This asymmetry may be due to the fact that the stability of a triple system exhibiting retrograde motion requires stronger isolation of the distant body from the inner binary than in the case of prograde motion.

The component mass ratio q for the inner binaries is about 0.5 for the Salpeter initial mass spectrum (Table 6). The ratio p of the masses of the distant component of a triple system and the inner binary is approximately 0.3 and depends on N only slightly. These parameters of the final triple systems are, on average, independent of the number of bodies in the initial system. We conclude based on the component mass ratio in the equal-mass case that, when $N \geq 12$, the inner binary includes the product of a coalescence in more than half of the stable triple systems.

4. COMPARISON BETWEEN MODELING AND OBSERVATIONS

Our modeling indicates that the dynamical evolution of multiple systems results in the formation of binary and stable triple systems. Below, we compare calculated parameters of the binary and triple systems with parameters of observed wide binaries and triple stars.

The semimajor axes of observed wide binaries with known orbital elements vary from 1 to 500 AU [21, 22]. Those of binaries formed via the decay of

Table 5. Comparison of calculated and observed orbital parameters of triple systems

Parameter	Observations, $P_{in} > 10^d$	Theory, SM
$\frac{\overline{P_{in}}}{P_{out}}$	0.040 ± 0.010	0.014 ± 0.002
$\left(\frac{P_{in}}{P_{out}}\right)_{\frac{1}{2}}$	0.013	0.009
$\overline{e}_{in}$	0.37 ± 0.04	0.63 ± 0.03
$(e_{in})_{\frac{1}{2}}$	0.39	0.66
$\overline{e}_{out}$	0.38 ± 0.04	0.50 ± 0.02
$(e_{out})_{\frac{1}{2}}$	0.40	0.50
n	38	69

low-multiplicity systems with $r = 100$ AU occupy approximately the same interval: $a = 1$–1000 AU (Fig. 3). The eccentricity distribution for observed wide binaries is consistent with the law $f(e) = 2e$ (see, for example, [21, 23, 24]), as is also true for binaries formed during the dynamical evolution of multiple stars (Fig. 1).

The component mass-ratio distribution for observed binaries depends strongly on the spectral type of the primary (see, for example, [23, 25]). Figure 6 presents the mass-ratio distributions for binaries in which the more massive component is a G star. Here, $q = \frac{m_2}{m_1}$, where m_2 is the mass of the less massive component. The dashed distribution was obtained from our modeling for the Salpeter initial mass spectrum for various N, while the solid distribution is that for observed wide binaries [23].

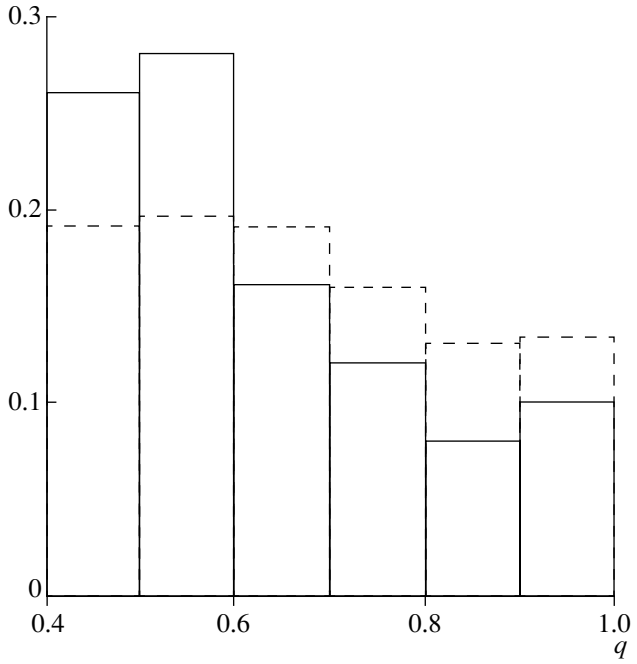

Fig. 6. Distributions of the component mass ratio for binaries with G primaries for observed (solid) and modeled (dashed) systems.

It is apparent that, on the whole, the observed and modeled distributions are similar. Differences between them may indicate that the initial mass spectrum for real multiple systems may be less steep than a Salpeter spectrum. The histogram was drawn for $q \geq 0.4$, since our modeling used a Salpeter mass spectrum with a minimum star mass of $0.4\ M_\odot$. This corresponds to $q \approx 0.4$ for $G0$ stars.

We compared the parameters of the model stable triple systems that formed with those of observed triples from the list [26], which contains 85 systems.

Table 5 presents the mean and median ratios of the periods of the outer and inner binaries, as well as their eccentricities. Table 6 contains the mean and median component mass ratios q for the inner binaries and the ratios p of the masses of the distant components to those of the inner binaries. The results of the modeling for the Salpeter initial mass spectrum (SM) for $N = 6$ are shown. The last rows contain the number of triple systems n whose parameters were used for the analysis. The orbital eccentricities and component masses were not known for all the triple stars in [26], so that the number of observed systems analyzed is less than 85.

We excluded from our analysis of the inner-binary eccentricities triple systems in which the periods of the inner binaries were less than 10 days. Tidal interactions between components can be substantial in these systems and were not taken into account in the modeling.

The median values for the period ratio in triples formed via the decay of multiple systems are in good agreement with the observations. However, the consistency for the mean values is much worse. This may be due to the difficulty of detecting triple systems with large outer-binary periods.

The eccentricities for inner and outer binaries that are members of observed triples are, on average, smaller than those derived from the modeling. In addition, the orbital eccentricities of the binaries in observed triple systems are in better agreement with the modeling results than those of the inner binaries. The deficiency of outer and inner binaries with elongated orbits may be associated with observational selection effects, which decrease the probability of detecting triple systems with large orbital eccentricities.

Partial circularization of the orbits of inner binaries with large eccentricities due to tidal interactions at

the orbit pericenters may also decrease the fraction of observed inner binaries with elongated orbits.

A comparison of the parameters q and p derived from our modeling of the dynamical evolution of multiple stars and obtained from observations yields the following conclusions. The mean and median component mass ratios for the inner binaries are consistent with the observed values. However, the observed mean and median values for p are almost twice those derived from the modeling for the indicated initial mass spectra. This may also be due to observational selection effects, manifest as a decreased probability of detecting triple systems with low-mass distant components.

Note that some fraction of the observed wide binaries and triple systems could have formed due to another mechanism, not related to the dynamical evolution of multiple stars (for example, joint formation or the decay of stellar clusters). This could also lead to differences between the parameters of observed and modeled binary and triple systems.

5. EJECTIONS OF STARS

During the dynamical evolution of stellar systems, they can eject single and binary stars. Tables 7 and 8 present the basic parameters of such escaping stars, such as their velocity, kinetic energy, and mass. The kinetic energy is given in units of the initial total energy of the system. For the escaping binaries, the kinetic energy of the center of mass of the binary and the sum of the component masses are presented. The last columns of the tables give the numbers of ejected single and binary stars.

Table 6. Comparison between modeled and observed component mass ratios for triple systems

Parameter	Observations	Theory, SM
$\overline{q}$	0.60 ± 0.04	0.49 ± 0.03
$q_{\frac{1}{2}}$	0.62	0.45
$\overline{p}$	0.64 ± 0.10	0.35 ± 0.04
$p_{\frac{1}{2}}$	0.50	0.28
n	58	69

We can see from Tables 7 and 8 that the average energies carried away from the systems by single and binary stars are comparable. The fraction of the energy lost by the system due to a single ejection decreases as N increases, independent of the initial mass spectrum. The velocities of escaping single stars are, on average, higher than those of the centers of mass of escaping binaries. The velocities of single stars are, on average, lower in the equal-mass case than for the Salpeter initial mass spectrum. The binaries do not display this trend.

As N increases, the mean and median masses of the single and binary stars ejected from the system increase. This may be due to an increase in the number of close approaches, which facilitates the accumula-

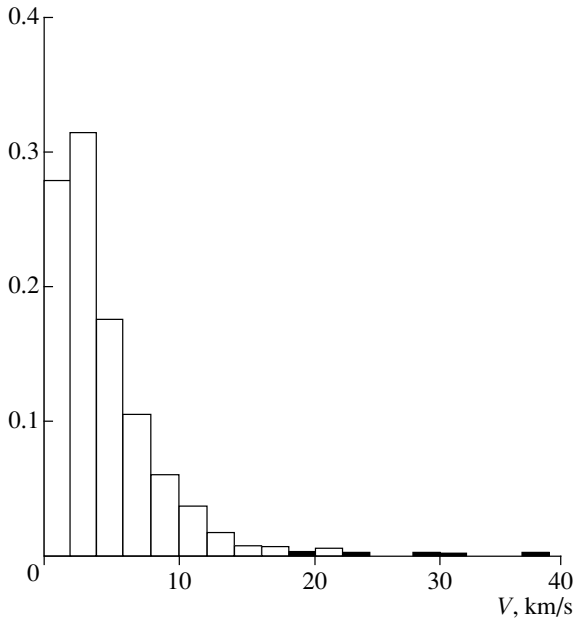

Fig. 7. Velocity distribution for single stars for the Salpeter initial mass spectrum.

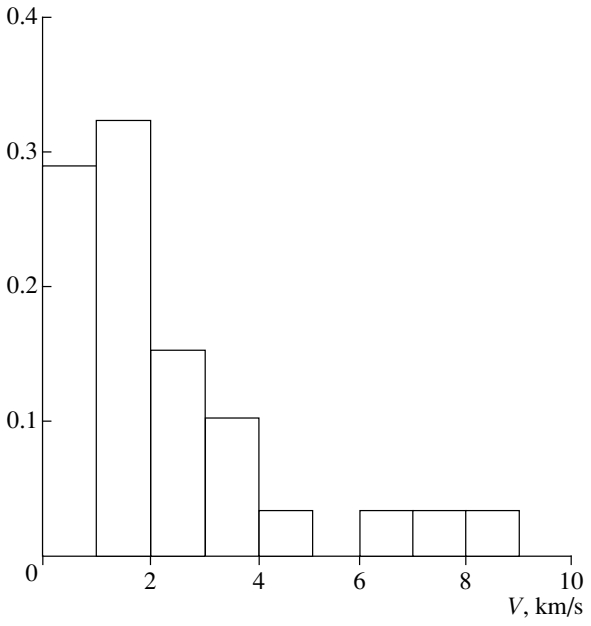

Fig. 8. Distribution of the velocities of the binary centers of mass for the Salpeter initial mass spectrum.

Table 7. Parameters of escaping single stars

N	Mass spectrum	$\overline{E}/\lvert E_0\rvert$	$E_{\frac{1}{2}}/\lvert E_0\rvert$	$\overline{V}$, km/s	$V_{\frac{1}{2}}$, km/s	$\overline{M}, M_\odot$	$M_{\frac{1}{2}}, M_\odot$	n
3	EM	0.190 ±	0.110	2.113 ±	1.818	1.001 ±	1.000	685
		± 0.010		± 0.063		± 0.001		
	SM	0.169 ±	0.091	2.450 ±	1.919	0.604 ±	0.503	768
		± 0.011		± 0.072		± 0.015		
6	EM	0.120 ±	0.049	3.449 ±	2.763	1.001 ±	1.000	1375
		± 0.006		± 0.070		± 0.001		
	SM	0.137 ±	0.052	4.394 ±	3.327	0.645 ±	0.542	1556
		± 0.009		± 0.094		± 0.008		
9	EM	0.081 ±	0.025	4.207 ±	3.148	1.003 ±	1.000	2291
		± 0.004		± 0.077		± 0.001		
	SM	0.091 ±	0.026	5.493 ±	3.997	0.687 ±	0.558	2920
		± 0.004		± 0.091		± 0.008		
12	EM	0.059 ±	0.018	4.897 ±	3.598	1.007 ±	1.000	3169
		± 0.002		± 0.075		± 0.002		
	SM	0.067 ±	0.019	6.382 ±	4.585	0.713 ±	0.577	4138
		± 0.002		± 0.090		± 0.007		
15	EM	0.047 ±	0.013	5.494 ±	3.905	1.005 ±	1.000	3911
		± 0.002		± 0.081		± 0.001		
	SM	0.055 ±	0.015	7.475 ±	5.301	0.735 ±	0.590	5469
		± 0.002		± 0.092		± 0.006		
18	EM	0.042 ±	0.011	6.179 ±	4.413	1.009 ±	1.000	2455
		± 0.002		± 0.115		± 0.002		
	SM	0.049 ±	0.011	8.034 ±	5.460	0.753 ±	0.598	3374
		± 0.002		± 0.139		± 0.007		

tion of kinetic energy sufficient for the ejection of a single star or binary from the system.

Figures 7 and 8 present the velocity distributions for escaping single stars and the centers of mass of escaping binaries for the Salpeter initial mass spectrum for $N = 6$. The distributions have maxima near 2–4 km/s and 1–2 km/s, respectively. The range of velocities for escaping single stars is broader than that for the centers of mass of the escaping binaries. The escaping single and binary stars display a smaller velocity dispersion in the equal-mass case than for the Salpeter mass spectrum. The shape of the distributions is retained as N increases, but the interval of possible velocities becomes broader. The velocity maxima shift slightly toward larger velocities. The velocities for the single stars can reach 80–100 km/s, while those for the centers of mass of the binaries reach 25 km/s. However, few stars have such high velocities. The shape of the distributions is independent of variations of the initial system parameters. Note that the escaping stars are, on average, less massive than those retained in the systems.

Observations indicate that many young T Tauri stars are located at substantial distances from star-forming regions [27–29]. This may be single stars ejected from young multiple systems with velocities of several tens of km/s [11, 12]. The results of our modeling of the dynamical evolution of low-multiplicity systems indicate that ejections of single stars with large velocities occur fairly frequently. Thus, young

Table 8. Parameters of escaping binaries

N	Mass spectrum	$\overline{E}/\lvert E_0\rvert$	$E_{\frac{1}{2}}/\lvert E_0\rvert$	$\overline{V}$, km/s	$V_{\frac{1}{2}}$, km/s	$\overline{M}, M_\odot$	$M_{\frac{1}{2}}, M_\odot$	n
6	EM	$0.093 \pm$	0.055	$2.285 \pm$	2.056	$2.000 \pm$	2.000	140
		$\pm\, 0.010$		$\pm\, 0.118$		$\pm\, 0.000$		
	SM	$0.085 \pm$	0.040	$2.273 \pm$	1.542	$1.645 \pm$	1.466	59
		$\pm\, 0.018$		$\pm\, 0.270$		$\pm\, 0.085$		
9	EM	$0.073 \pm$	0.030	$3.012 \pm$	2.423	$2.040 \pm$	2.000	251
		$\pm\, 0.007$		$\pm\, 0.136$		$\pm\, 0.012$		
	SM	$0.067 \pm$	0.030	$2.898 \pm$	2.372	$2.086 \pm$	1.789	95
		$\pm\, 0.008$		$\pm\, 0.211$		$\pm\, 0.120$		
12	EM	$0.049 \pm$	0.021	$3.360 \pm$	2.632	$2.151 \pm$	2.000	325
		$\pm\, 0.004$		$\pm\, 0.127$		$\pm\, 0.023$		
	SM	$0.039 \pm$	0.018	$2.987 \pm$	2.364	$2.226 \pm$	1.865	154
		$\pm\, 0.006$		$\pm\, 0.215$		$\pm\, 0.116$		
15	EM	$0.048 \pm$	0.017	$3.995 \pm$	3.087	$2.262 \pm$	2.000	343
		$\pm\, 0.005$		$\pm\, 0.172$		$\pm\, 0.028$		
	SM	$0.041 \pm$	0.016	$3.641 \pm$	3.210	$2.460 \pm$	1.886	178
		$\pm\, 0.006$		$\pm\, 0.209$		$\pm\, 0.118$		
18	EM	$0.038 \pm$	0.010	$4.148 \pm$	2.831	$2.318 \pm$	2.000	176
		$\pm\, 0.006$		$\pm\, 0.272$		$\pm\, 0.047$		
	SM	$0.036 \pm$	0.013	$3.753 \pm$	2.997	$2.698 \pm$	2.006	82
		$\pm\, 0.008$		$\pm\, 0.335$		$\pm\, 0.204$		

"runaway" stars may be single stars ejected during the dynamical decay of young multiple systems.

6. CONCLUSION

Theoretical studies of star formation and observations of star-forming regions indicate that a substantial fraction of stars may be formed in low-multiplicity groups (see, for example, [30]). It appears that, at some stage in the evolution of such systems, gravitational interactions between stars become dominant, and the evolution of the system can be studied via numerical integration of the equations of motion for the gravitational N-body problem, taking into account possible coalescences of closely approaching stars.

Our modeling of the dynamics of groups of $N = 3$–18 bodies indicates that, as a rule, the evolution of a system results in the formation of a final binary or stable triple system.

For stellar groups, we can identify several dynamical properties stable with respect to the initial conditions and mass spectrum chosen:

(1) formation of a high fraction (10–15%) of stable final triple systems;

(2) development of the universal eccentricity distribution $f(e) = 2e$ for the final and escaping binaries;

(3) pronounced hierarchy of the stable final triple systems: the mean ratio of the semimajor axes of the inner and outer binaries is approximately 1 : 20;

(4) the eccentricities of the outer binaries in stable triple systems are, on average, lower than those of the inner binaries, with systems with prograde motions dominating;

(5) on the whole, the orbital parameters of the binary systems formed are consistent with those of observed wide binaries.

REFERENCES

1. T. van Albada, Bull. Astron. Inst. Netherlands **19**, 479 (1968).
2. A. Burkert and P. Bodenheimer, Mon. Not. R. Astron. Soc. **280**, 1190 (1996).
3. R. S. Klessen, A. Burkert, and M. R. Bate, Astrophys. J. **501**, L205 (1998).
4. M. J. Valtonen and S. Mikkola, Ann. Rev. Astron. Astrophys. **29**, 9 (1991).
5. Zh. P. Anosova, Itogi Nauki Tekh., Ser. Astron. **26**, 57 (1985).
6. M. J. Valtonen, Vistas Astron. **32**, 23 (1988).
7. Zh. P. Anosova and V. V. Orlov, Tr. Astron. Obs. Leningr. Univ. **40**, 66 (1985).
8. S. Sigurdsson and E. S. Phinney, Astrophys. J. **415**, 631 (1993).
9. R. S. Harrington, Celest. Mech. **9**, 465 (1974).

10. R. S. Harrington, Astron. J. **80**, 1081 (1975).
11. M. F. Sterzik and R. H. Durisen, Astron. Astrophys. **339**, 95 (1998).
12. M. F. Sterzik and R. H. Durisen, Astron. Astrophys. **304**, L9 (1995).
13. L. Kiseleva, J. Colin, B. Dauphole, and P. Eggleton, Mon. Not. R. Astron. Soc. **301**, 759 (1998).
14. S. Mikkola and S. J. Aarseth, Celest. Mech. Dyn. Astron. **57**, 439 (1993).
15. W. Benz and J. G. Hills, Astrophys. J. **323**, 614 (1987).
16. W. Benz and J. G. Hills, Astrophys. J. **389**, 546 (1992).
17. E. E. Salpeter, Astrophys. J. **121**, 161 (1955).
18. V. G. Golubev, Dokl. Akad. Nauk SSSR **174**, 767 (1967).
19. V. A. Ambartsumyan, Astron. Zh. **14**, 207 (1937).
20. J. J. Monaghan, Mon. Not. R. Astron. Soc. **176**, 63 (1976).
21. A. Duquennoy and M. Mayor, Astron. Astrophys. **248**, 485 (1991).
22. W. D. Heacox, Astron. J. **115**, 325 (1998).
23. M. J. Valtonen, Astrophys. J. **485**, 785 (1997).
24. A. A. Tokovinin, Pis'ma Astron. Zh. **24**, 217 (1998) [Astron. Lett. **24**, 178 (1998)].
25. D. A. Fisher and G. W. Marcy, Astrophys. J. **396**, 178 (1992).
26. V. V. Orlov and A. V. Petrova, private communication (1999).
27. R. Neuhäuser, M. F. Sterzik, G. Torres, and E. L. Martin, Astron. Astrophys. **299**, L13 (1995).
28. M. F. Sterzik, J. M. Alcala, R. Neuhäuser, and J. H. M. M. Schmitt, Astron. Astrophys. **297**, 418 (1995).
29. M. F. Sterzik and J. H. M. M. Schmitt, Astron. J. **114**, 1673 (1997).
30. F. C. Adams and P. C. Myers, Astrophys. J. **553**, 744 (2001).

Translated by K. Maslennikov